Journal of Sensors

# Multidimensional Sensing and Big Data-Aided Intelligent Maintenance

Lead Guest Editor: Aijun Yin
Guest Editors: Chuan Li and Xiaojun Wei

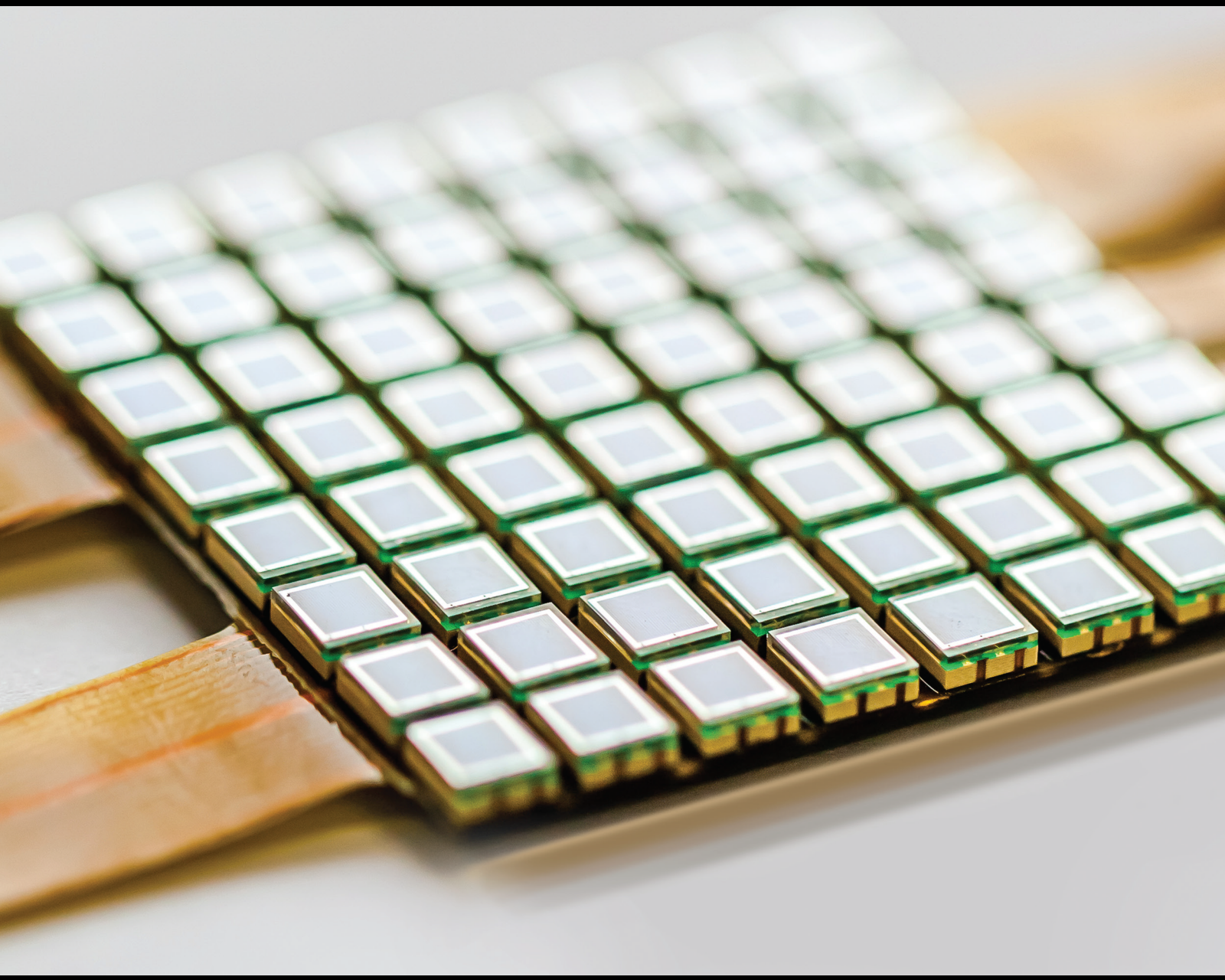

# Multidimensional Sensing and Big Data-Aided Intelligent Maintenance

Journal of Sensors

# Multidimensional Sensing and Big Data-Aided Intelligent Maintenance

Lead Guest Editor: Aijun Yin
Guest Editors: Chuan Li and Xiaojun Wei

# Contents

**Research on Safety Evaluation of Commercial Vehicle Driving Behavior Based on Data Mining Technology**
Shuilong He, Yongliang Wang, Yuye Chen, Fei Xiao, Jucai Deng, and Enyong Xu
Research Article (13 pages), Article ID 9927348, Volume 2021 (2021)

**Detail 3D Face Reconstruction Based on 3DMM and Displacement Map**
Tianping Li, Hongxin Xu, Hua Zhang, and Honglin Wan
Research Article (13 pages), Article ID 9921101, Volume 2021 (2021)

**Analyzing the Impact of Climate Factors on GNSS-Derived Displacements by Combining the Extended Helmert Transformation and XGboost Machine Learning Algorithm**
Hanlin Liu, Linqiang Yang, and Linchao Li
Research Article (13 pages), Article ID 9926442, Volume 2021 (2021)

**Energy Management of Fuel Cell Vehicles Based on Model Prediction Control Using Radial Basis Functions**
Weiwei Xin, Weiguang Zheng, Jirong Qin, Shangjun Wei, and Chunyu Ji
Research Article (8 pages), Article ID 9985063, Volume 2021 (2021)

**Quality Prediction of Strip in Finishing Rolling Process Based on GBDBN-ELM**
Shuang Li, Jian Wang, and Sen Chen
Research Article (14 pages), Article ID 9943153, Volume 2021 (2021)

**Vibration Diagnosis and Treatment for a Scrubber System Connected to a Reciprocating Compressor**
Shuangshuang Li, Guicheng Yu, Ding Tang, Ming Li, and Huaming Han
Research Article (12 pages), Article ID 6687295, Volume 2020 (2020)

Hindawi
Journal of Sensors
Volume 2021, Article ID 9927348, 13 pages
https://doi.org/10.1155/2021/9927348

*Research Article*

# Research on Safety Evaluation of Commercial Vehicle Driving Behavior Based on Data Mining Technology

**Shuilong He**,[1,2] **Yongliang Wang**,[1] **Yuye Chen**,[2] **Fei Xiao**,[2] **Jucai Deng**,[2] **and Enyong Xu**[2,3]

[1]*School of Mechanical and Electrical Engineering, Guilin University of Electronic Technology, Guilin 541004, China*
[2]*Dongfeng Liuzhou Motor Co., Ltd., Liuzhou 545005, China*
[3]*School of Mechanical Science and Engineering, Huazhong University of Science and Technology, Wuhan 430074, China*

Correspondence should be addressed to Enyong Xu; 13557729070@163.com

Received 18 March 2021; Accepted 26 October 2021; Published 25 November 2021

Academic Editor: Antonio Lazaro



The arrival of big data era of internet of vehicles promotes the rapid development of logistics industry, which also indirectly leads to the high traffic accident rate, resulting in huge casualties and property losses. Driving behavior is considered the most central factor leading to traffic accidents. Therefore, a scientific and effective method for evaluating the safety of commercial vehicle driving behavior is urgently needed. In this study, a comprehensive evaluation model of driving behavior security based on multimembership function is proposed, and entropy weight method (EWM), analytic hierarchy process (AHP), and fuzzy comprehensive evaluation algorithm are integrated. Firstly, the evaluation system of commercial vehicle safety of driving behavior is established. Secondly, the weight vector of each evaluation index is determined by combining EW-AHP to eliminate the subjectivity of the traditional AHP algorithm. Then, the fuzzy comprehensive evaluation matrix is calculated based on the multimembership function and fuzzy mathematics theory, and the quantitative evaluation of driving behavior safety is realized based on the matrix. Finally, the real road vehicle driving data and driving behavior data are verified by experiments. The experimental results show that the model can accurately and reasonably evaluate the safety of driving behavior, which is of great significance to improve road traffic safety.

## 1. Introduction

With the rapid development of internet of vehicles technology and big data technology, the logistics industry has developed rapidly [1]. But at the same time, the accident rate of commercial vehicles increases quickly, causing huge casualties and property losses. Driving behavior is generally considered one of the most important factors in crash occurrence [2, 3]. However, due to the stochastic nature of driving, the measurement and modeling of driving behavior remain a challenging topic today. By studying the relationship between driving behavior and accident tendency and exploring the key factors affecting driving risk, the safety of individual driving behavior can be quantitatively evaluated, which is helpful to distinguish safe from unsafe driving and is of great significance for improving road traffic safety [4].

In the safety research field of driving behavior, a large number of researchers have participated and achieved remarkable results. Among them, nonparametric methods and data mining techniques are widely used [5–9]. For example, Chang et al. proposed a classification and regression tree (CART) model to establish the relationship between injury severity, driver/vehicle characteristics, and accident variables, indicating that vehicle type is a very important variable related to the severity of a car accident [5, 6]. Wang et al. characterized the driving risks with the characteristics of sharp deceleration dangerous events and studied the relationship between vehicle motion state, potential collision type, driving environment, driver information,

and driving risk by combining $k$-means clustering and classification regression tree method [7]. Zhu et al. represented the driving risk by the number of historical accidents and studied the relationship between driving behavior, driver information, and accident risk with the method of the multilayer Bayesian network, so as to realize the evaluation of driving behavior safety [8]. Li et al. compared the application of support vector machine (SVM) with the traditional negative binomial model in predicting motor vehicle collision. The results show that SVM is more effective [9]. In addition, Guo et al. assessed the factors associated with individual driver risk using naturalistic driving data [10]. Hong et al. proposed an aggressive driving behavior assessment model based on OBD and smart phone data [11].

In the evaluation model of driving behavior safety, the selection of evaluation index is very important [12]. Jun et al. compared and analyzed the driving behaviors of drivers who had a car accident with those who had not and found that there were significant differences in driving range, driving speed, and acceleration between the two groups [13]. Ayuso et al. found that the longer the distance young drivers travel in speeding, the greater the probability of accidents. This study revealed the relationship between accident tendency and speeding [14, 15]. Bruce et al. believe that the violent braking and starting behaviors during driving are a kind of "high gravity acceleration" event, which can be used to predict the specific type of accidents of young drivers [16]. Research by Omar et al. show that drivers who have experienced traffic accidents have more sudden braking, suggesting that sudden braking may be an indicator of a driver's participation in dangerous traffic conditions [17]. To sum up, driving distance, driving speed, and acceleration are the key indicators that affect the safety of driving behavior.

Previous research with the evaluation of driving behavior safety have focused on passenger vehicles, while there are few studies in the field of commercial vehicles. In addition, the evaluation models proposed by many researchers all focus on distinguishing safe and unsafe driving behaviors and studying the causes affecting unsafe driving behaviors, while there are few researches on quantitative score of the safety of driving behaviors.

In this paper, based on the natural driving data of commercial vehicles, we combine analytic hierarchy process (AHP), entropy weight method (EWM), and fuzzy comprehensive evaluation algorithm to establish a multimembership function fuzzy comprehensive evaluation model of commercial vehicle driving behavior safety. Firstly, EW-AHP is used to determine the weight vector of each evaluation index, and then the fuzzy comprehensive evaluation algorithm model is established. The single-factor membership vector and comprehensive fuzzy evaluation matrix were calculated successively by using fuzzy operation, and the final driving behavior score was determined. Finally, the rationality and validity of the model are verified by experiments. The model can be used not only to analyze factors affecting driving risk and identify driving styles but also to distinguish safe and unsafe driving behaviors and quantify the safety scores of driving behavior.

The paper is outlined as follows. In Section 2, the steps of AHP, EWM, and fuzzy comprehensive evaluation algorithm are introduced briefly. Section 3 proposes a safety evaluation model of commercial vehicle driving behavior, combining the EW-AHP and fuzzy comprehensive evaluation algorithm. In Section 4, the validity of the model is verified based on the natural driving data of commercial vehicles. Section 5 concludes the work and discusses further analysis.

## 2. Theoretical Background

*2.1. Analytic Hierarchy Process (AHP).* AHP is widely used in multiobjective decision problems. It can decompose the elements to be decided into three levels, target, criterion, and index, and conducted qualitative and quantitative analysis on this basis [18]. The steps of AHP algorithm are briefly summarized as follows:

(1) Select evaluation index and establish evaluation system

(2) Construct the comparison scale between each index

(3) Construct a judgment matrix for each level

(4) Verify the consistency of each judgment matrix. If the consistency test fails, step (3) will be returned to modify the judgment matrix. If the consistency test passes, proceed to the next step. In this step, the calculation formula of consistency index $CI$ is as follows:

$$CI = \frac{\lambda_{\max} - n}{n - 1}. \tag{1}$$

In formula (1), $\lambda_{\max}$ is the maximum eigenvalue of the judgment matrix, and $n$ is the order of the judgment matrix. Then, the corresponding mean random consistency index $RI$ can be found according to Table 1. Finally, the consistency ratio $CR$ can be calculated by formula (2).

$$CR = \frac{CI}{RI}. \tag{2}$$

When the consistency ratio $CR = 0$, the judgment matrix has complete consistency, and then it passes the consistency test. When $CR < 0.1$, the judgment matrix has satisfactory consistency, and then it passes the consistency test. When $CR > 0.1$, the judgment matrix does not have consistency, and the consistency test does not pass, so the judgment matrix needs to be modified.

(5) Calculate weight vector of each index

(6) Complete the evaluation of the goal.

*2.2. Entropy Weight Method (EWM).* EWM is an objective method to calculate the weight. In information theory, entropy is a way to measure the uncertainty of events. The greater the uncertainty of the event, the greater the entropy and the more information it contains. The smaller the

Table 1: Mean random consistency index.

| $n$ | 1 | 2 | 3 | 4 | 5 | 6 | 7 |
|---|---|---|---|---|---|---|---|
| $RI$ | 0.00 | 0.00 | 0.52 | 0.89 | 1.12 | 1.26 | 1.36 |

uncertainty of the event, the smaller the entropy and the smaller the information contained [19].

According to the characteristics of entropy, the randomness and disorder degree of an event can be judged by calculating the entropy value, and the dispersion degree of an index can also be judged by the entropy value. The greater the dispersion degree of an index, the greater the influence (weight) of the index on the evaluation target will be; otherwise, the less it will be [20]. The steps of EWM algorithm are briefly summarized as follows:

(1) Import the data that need to calculate the entropy weight

(2) Standardize the data matrix

It is assumed that the data matrix consisting of $n$ objects to be evaluated and $m$ evaluation indexes is as follows:

$$X = \begin{bmatrix} x_{11} & x_{12} & \cdots & x_{1m} \\ x_{21} & x_{22} & \cdots & x_{2m} \\ \vdots & \vdots & \ddots & \vdots \\ x_{n1} & x_{n2} & \cdots & x_{nm} \end{bmatrix}. \tag{3}$$

Since the meanings of positive and negative indicators are different, different formulas are needed for data standardization processing of positive and negative indicators. Formula (4) for standardization of positive indicators and formula (5) for standardization of negative indicators are as follows:

$$z_{ij} = \frac{x - \min\left\{x_{1j}, \cdots, x_{nj}\right\}}{\max\left\{x_{1j}, \cdots, x_{nj}\right\} - \min\left\{x_{1j}, \cdots, x_{nj}\right\}}, \tag{4}$$

$$z_{ij} = \frac{\min\left\{x_{1j}, \cdots, x_{nj}\right\} - x_{ij}}{\max\left\{x_{1j}, \cdots, x_{nj}\right\} - \min\left\{x_{1j}, \cdots, x_{nj}\right\}} \tag{5}$$

(3) Calculate the sample specific gravity

Calculate the proportion of the $i$th sample in the $j$th index and regard it as the probability used in the calculation of relative entropy. Calculated from the previous step, the normalized matrix $Z$ is

$$Z = \begin{bmatrix} z_{11} & z_{12} & \cdots & z_{1m} \\ z_{21} & z_{22} & \cdots & z_{2m} \\ \vdots & \vdots & \ddots & \vdots \\ z_{n1} & z_{n2} & \cdots & z_{nm} \end{bmatrix}. \tag{6}$$

The probability matrix $P$ can be calculated, where the calculation formula of each element $p_{ij}$ is as follows:

$$P_{ij} = \frac{z_{ij}}{\sum_{i=1}^{n} z_{ij}}, i = 1 \cdots n, j = 1 \cdots m \tag{7}$$

(4) Calculate information entropy and information utility values of each index

For the $j$th index, its information entropy is calculated as shown in Formula (8), and its information utility value is calculated as shown in formula (9).

$$e_j = -\frac{1}{\ln n} \sum_{i=1}^{n} p_{ij} \ln\left(p_{ij}\right), j = 1, \cdots, m, \tag{8}$$

$$d_j = 1 - e_j, j = 1, \cdots, m \tag{9}$$

(5) Calculate the entropy weight of each index.

The calculation formula of entropy weight of each index is as follows:

$$V_j = \frac{d_j}{\sum_{i=1}^{n} d_j}, j = 1, \cdots, m. \tag{10}$$

*2.3. Fuzzy Comprehensive Evaluation Algorithm.* Fuzzy comprehensive evaluation is a method to quantify a number of influence factors with unclear boundaries and difficult to be quantified, and to conduct comprehensive evaluation of the grade status of the evaluated object from multiple factors [21, 22]. The steps of fuzzy comprehensive evaluation algorithm are briefly summarized as follows:

(1) Establish the factor set of each evaluation index (factors set)

(2) Determine the evaluation grade of the object to be evaluated (evaluation set)

(3) Determine the weight vector of each evaluation index

(4) Determine the membership function. The commonly used membership functions include the Gaussian function, ridge function, and rectangle function. Their formula is as follows:

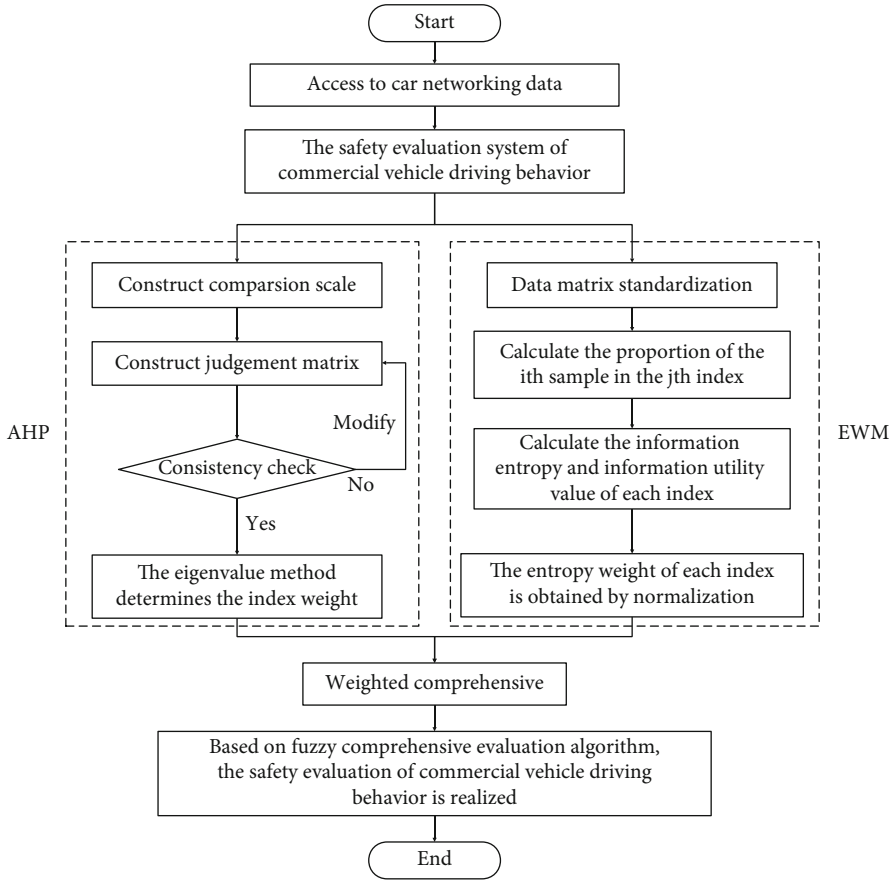


Figure 1: Overall algorithm flow chart.

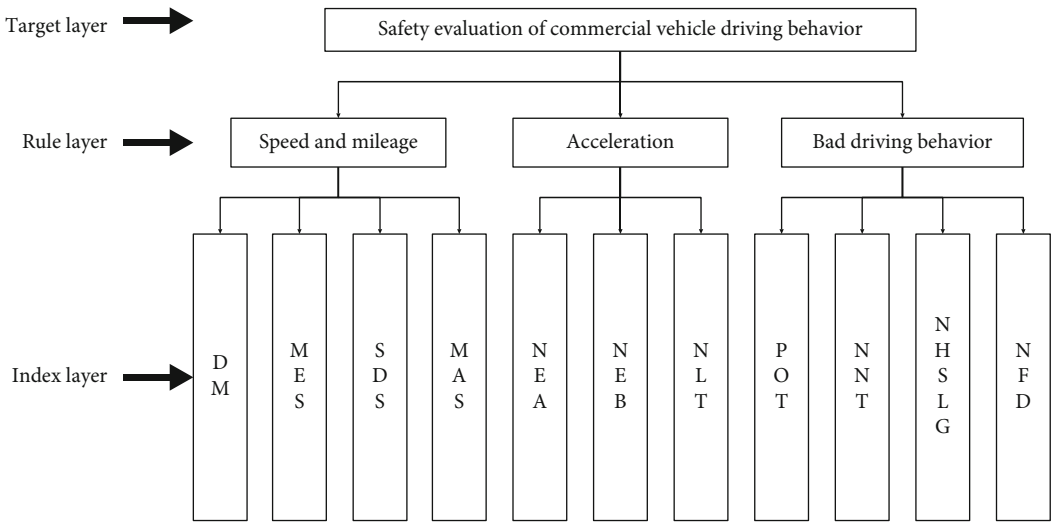


Figure 2: Safety evaluation index system of commercial vehicle driving behavior.

Gaussian function (minimum type, intermediate type, and maximum type):

$$r(x) = \begin{cases} 1, & x \le a \\ e^{-((x-a)/\sigma)^2} & x > a, \end{cases} \tag{11}$$

$$r(x) = \begin{cases} 0, & x \le a \\ 1 - e^{-((x-a)/\sigma)^2} & x > a, \end{cases} \tag{12}$$

$$r(x) = e^{-((x-a)/\sigma)^2}, -\infty < x < +\infty. \tag{13}$$

Table 2: Judgment matrix of criterion layer $U$.

| $U$ | $U_1$ | $U_2$ | $U_3$ |
|---|---|---|---|
| $U_1$ | 1 | 3 | 4 |
| $U_2$ | 1/3 | 1 | 2 |
| $U_3$ | 1/4 | 1/2 | 1 |

Ridge function (minimum type, intermediate type, and maximum type):

$$r(x) = \begin{cases} 1, & x \le a \\ \frac{1}{2} - \frac{1}{2} \sin \frac{\pi}{b-a}\left(x - \frac{a+b}{2}\right), & a < x < b \\ 0, & x \ge b, \end{cases} \quad (14)$$

$$r(x) = \begin{cases} 0, & x \le a \\ \frac{1}{2} + \frac{1}{2} \sin \frac{\pi}{b-a}\left(x - \frac{a+b}{2}\right), & a < x < b \\ 1 & b < x \le c \\ \frac{1}{2} - \frac{1}{2} \sin \frac{\pi}{d-c}\left(x - \frac{c+d}{2}\right), & c < x < d \\ 0, & x \ge d, \end{cases} \quad (15)$$

$$r(x) = \begin{cases} 0, & x \le a \\ \frac{1}{2} + \frac{1}{2} \sin \frac{\pi}{b-a}\left(x - \frac{a+b}{2}\right), & a < x < b \\ 1, & x \ge b. \end{cases} \quad (16)$$

Rectangle function (minimum type, intermediate type, and maximum type):

$$r(x) = \begin{cases} 1, & x \le a \\ 0, & x > a, \end{cases} \quad (17)$$

$$r(x) = \begin{cases} 0, & x < a \\ 1, & x \ge a, \end{cases} \quad (18)$$

$$r(x) = \begin{cases} 0, & x < a \\ 1, & a \le x < b \\ 0, & x \ge b \end{cases} \quad (19)$$

(5) The fuzzy comprehensive evaluation matrix is obtained

Firstly, formula (20) is used to calculate the single-factor membership vector, and formula (21) is used to calculate the multifactor membership matrix.

$$R_i = W_k \odot r_i, \quad (20)$$

Table 3: Judgment matrix of index layer $U_1$.

| $U_1$ | $U_{11}$ | $U_{12}$ | $U_{13}$ | $U_{14}$ |
|---|---|---|---|---|
| $U_{11}$ | 1 | 1/3 | 1/2 | 1 |
| $U_{12}$ | 3 | 1 | 2 | 2 |
| $U_{13}$ | 2 | 1/2 | 1 | 1 |
| $U_{14}$ | 1 | 1/2 | 1 | 1 |

Table 4: Judgment matrix of index layer $U_2$.

| $U_2$ | $U_{21}$ | $U_{22}$ | $U_{23}$ |
|---|---|---|---|
| $U_{21}$ | 1 | 1 | 2 |
| $U_{22}$ | 1 | 1 | 3 |
| $U_{23}$ | 1/2 | 1/3 | 1 |

Table 5: Judgment matrix of index layer $U_3$.

| $U_3$ | $U_{31}$ | $U_{32}$ | $U_{33}$ | $U_{34}$ |
|---|---|---|---|---|
| $U_{31}$ | 1 | 1/2 | 1/2 | 1/2 |
| $U_{32}$ | 2 | 1 | 2 | 1 |
| $U_{33}$ | 2 | 1/2 | 1 | 1/2 |
| $U_{34}$ | 2 | 1 | 2 | 1 |

Table 6: Weight summary results of EW-AHP combination.

| Indicators | $U_1$ (0.1311) | $U_2$ (0.5267) | $U_3$ (0.3422) | The comprehensive weights |
|---|---|---|---|---|
| $U_{11}$ | 0.5805 | | | 0.0761 |
| $U_{12}$ | 0.2677 | | | 0.0350 |
| $U_{13}$ | 0.1379 | | | 0.0181 |
| $U_{14}$ | 0.0149 | | | 0.0020 |
| $U_{21}$ | | 0.2262 | | 0.1191 |
| $U_{22}$ | | 0.6632 | | 0.3493 |
| $U_{23}$ | | 0.1106 | | 0.0583 |
| $U_{31}$ | | | 0.1977 | 0.0677 |
| $U_{32}$ | | | 0.1876 | 0.0642 |
| $U_{33}$ | | | 0.2622 | 0.0897 |
| $U_{34}$ | | | 0.3524 | 0.1206 |

$$R = \begin{bmatrix} R_1 \\ R_2 \\ \vdots \\ R_m \end{bmatrix}. \quad (21)$$

In formula (20), $R_i$ is a single-factor membership vector. The basic principle is derived from the fuzzy transformation $\odot$ of the weight vector corresponding to $r_i$ (the

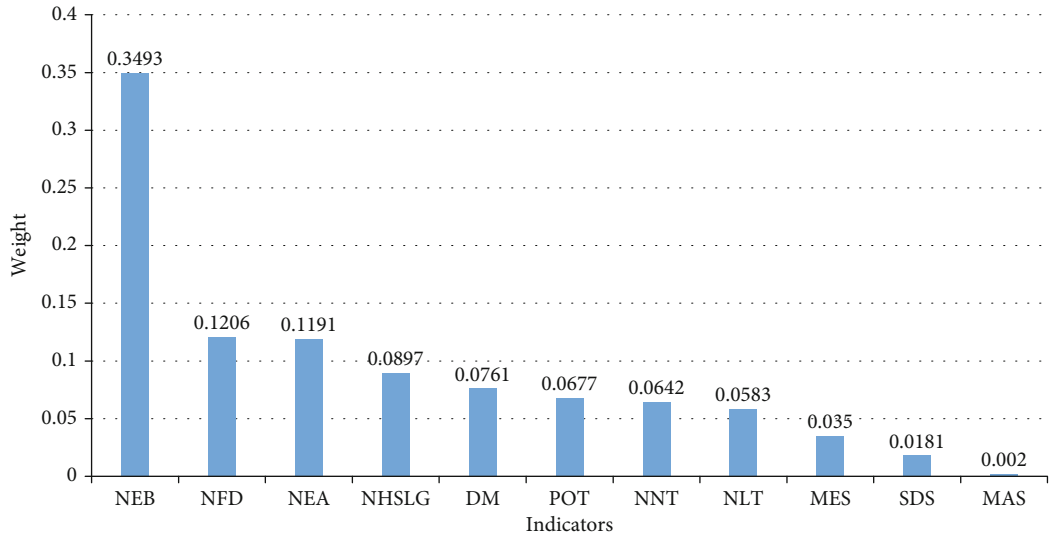


Figure 3: The weight of each index.

membership degree of the $i$th index for each evaluation level) and the second-level index, The selected fuzzy operator [23, 24] is $(\bullet+)$, $1 \le k \le 3$, $1 \le i \le m$.

$$S = W \odot R = (W_1, W_2, W_3) \odot \begin{bmatrix} r_{11} & r_{12} & \cdots & r_{1n} \\ r_{21} & r_{22} & \cdots & r_{2n} \\ \vdots & \vdots & \cdots & \vdots \\ r_{m1} & r_{m2} & \cdots & r_{mn} \end{bmatrix}. \tag{22}$$

$S$ is the fuzzy comprehensive evaluation matrix, $W$ is the weight vector of driving behavior evaluation index determined by formula (23), and $R$ is the multifactor membership matrix determined by formula (21). The operator symbol is the fuzzy operator $(\bullet+)$. Based on the above algorithm steps, the quantitative evaluation of commercial vehicle driving behavior safety can be realized.

(6) Quantify and score your goals.

## 3. Proposed Ensemble Method

The subjectivity of traditional AHP algorithm can be eliminated by combining the three methods in the second section and using the entropy weight analytic hierarchy process to comprehensively assign weights to each evaluation index. Then, the fuzzy comprehensive evaluation algorithm is used to score the driving behavior quantitatively. The flow chart of the overall algorithm is shown in Figure 1.

*3.1. Establish the Safety Evaluation System of Commercial Vehicle Driving Behavior.* Referring to Section 1, we can know that the driving mileage, driving speed, and acceleration are the key indicators affecting the safety of driving behavior. We can extend some other indicators from these three indicators, such as driving mileage, mean speed, overspeed, standard deviation of speed, maximum speed, emergency acceleration, and emergency braking. However, in the field of commercial vehicles, there are a large number of bad driving behaviors such as large throttle, low gear and high speed, neutral taxiing, and fatigue driving. Therefore, we also choose the above indicators.

Of course, the indicators affecting the driving safety are far more than this. Indicators such as weather, road conditions, driver age, and gender will have a certain impact on driving safety. However, the main research object of this paper is the driver's driving behavior, so these indicators are not within the scope of consideration.

Table 7: Corresponding scores of each rating level.

| Road conditions | Rating | | | | |
|---|---|---|---|---|---|
| | Excellent | Good | Average | Poor | Very poor |
| Urban road | 90 | 70 | 50 | 30 | 10 |
| The highway | 90 | 80 | 60 | 45 | 25 |
| Mixed road | 85 | 65 | 45 | 25 | 5 |

Table 8: Selection scheme of multimembership function.

| | |
|---|---|
| Driving mileage (DM) | Gaussian function |
| Mean speed (MES) | |
| Standard deviation of the speed (SDS) | |
| Maximum speed (MAS) | Ridge function |
| Number of emergency acceleration (NEA) | |
| Number of emergency braking (NEB) | Rectangle function |
| Number of large throttle (NLT) | |
| Proportion of overspeed time (POT) | Ridge function |
| Number of neutral taxiing (NNT) | |
| Number of high speed in low gear (NHSLG) | |
| Number of fatigue driving (NFD) | Rectangle function |

Table 9: Reference values of membership degrees of each indicator to each grade.

| Indicator | Coefficient | | | | | | | | |
|---|---|---|---|---|---|---|---|---|---|
| | $x_1$ | $x_2$ | $x_3$ | $x_4$ | $x_5$ | $x_6$ | $x_7$ | $x_8$ | $x_9$ |
| DM | 50 | 155 | 260 | 365 | 470 | 575 | 680 | 785 | 1000 |
| MES | 66 | 69 | 72 | 75 | 78 | 81 | 84 | 87 | 90 |
| SDS | 5 | 10 | 15 | 20 | 25 | 30 | 35 | 40 | — |
| MAS | 88 | 92 | 95 | 97 | 99 | 101 | 103 | 105 | — |
| NEA | 0 | 1 | 2 | 3 | 4 | 5 | 6 | 7 | — |
| NLT | 5 | 20 | 35 | 50 | 65 | 80 | 95 | 110 | — |
| POT | 0 | 0.005 | 0.020 | 0.035 | 0.050 | 0.065 | 0.080 | 0.100 | — |
| NNT | 0 | 1 | 2 | 3 | 4 | 5 | 6 | 7 | — |
| NHSLG | 0 | 2 | 4 | 6 | 8 | 10 | 12 | 14 | — |

Table 10: Vehicle driving data.

| Data generation time | Latitude and longitude | Speed (km/h) | Rotate speed (rpm) | Accumulated distance (km) | Acceleration ($m/s^2$) | Time (h) |
|---|---|---|---|---|---|---|
| 2020-8-1 0:00 | 114.9279 \| 31.9632 | 36.0 | 1166.000 | 22255.4 | 0.30 | 271.5 |
| 2020-8-1 0:00 | 114.9282 \| 31.9641 | 47.6 | 1211.125 | 22255.6 | 0.41 | 271.5 |
| 2020-8-1 0:00 | 114.9287 \| 31.9653 | 56.7 | 1114.125 | 22255.7 | 0.30 | 271.5 |
| ⋮ | ⋮ | ⋮ | ⋮ | ⋮ | ⋮ | ⋮ |
| 2020-8-31 23:59 | 125.4410 \| 43.9755 | 97.3 | 1190.125 | 54854.7 | -0.09 | 697.8 |
| 2020-8-31 23:59 | 125.4425 \| 43.9734 | 93.3 | 1147.125 | 54854.9 | -0.06 | 697.8 |

In addition, considering too many factors in the model is not conducive to the development of subsequent analysis, so we chose the key indicators identified above.

Therefore, the safety evaluation system of commercial vehicle driving behavior shown in Figure 2 can be established. Among them, the target layer is the safety evaluation of commercial vehicle driving behavior ($U$). The criteria layer includes speed and mileage ($U_1$), acceleration ($U_2$), and bad driving behavior ($U_3$). There are 11 indicators ($U_{11} - U_{34}$) in the index layer; they are the driving mileage (DM), mean speed (MES), standard deviation of the speed (SDS), maximum speed (MAS), number of emergency acceleration (NEA), number of emergency braking (NEB), number of large throttle (NLT), proportion of overspeed time (POT), number of neutral taxiing (NNT), number of high speed in low gear (NHSLG), and number of fatigue driving (NFD).

*3.2. Determination of Index Weight Based on AHP.* Based on the SATTY1-9 scale method [25] and the opinions of senior experts in the automobile industry, the judgment matrix of each index layer can be obtained as shown in Tables 2–5.

According to formulas (1) and (2) and judgment matrix of each indicator layer, it can be calculated that that the consistency ratio ($CR$) of judgment matrix of each indicator layer is less than 0.1, satisfying the consistency. Therefore, the maximum eigenvalue of the consistent matrix and its corresponding eigenvector can be obtained, which can represent the importance degree of each index layer, namely, weight allocation.

Therefore, the weight vector of each level index can be calculated by the MATLAB programming. The weight vector of criterion layer $U$ is [0.6250, 0.2385, 0.1365]. The weight vector of indicator layer $U_1$ is [0.1484, 0.4258, 0.2312, 0.1945]. The weight vector of indicator layer $U_2$ is [0.3874, 0.4434, 0.1692]. The weight vector of indicator layer $U_3$ is [0.1404, 0.3300, 0.1996, 0.3300]. The comprehensive weight vector of each indicator layer $\omega = [0.0928, 0.2661, 0.1445, 0.1216, 0.0924, 0.1058, 0.0404, 0.0192, 0.0450, 0.0272, 0.0450]$.

*3.3. Determine the Index Weight Based on Entropy Weight Method (EWM).* Combined with formulas (3)–(10), the weight of each index can be calculated by the MATLAB programming as follows: $v = [0.0371, 0.0007, 0.0286, 0.0386, 0.0263, 0.0631, 0.1438, 0.1292, 0.0662, 0.1035, 0.1635, 0.1993]$.

*3.4. EW-AHP Combination Weights.* Based on the weights obtained by the AHP and EWM algorithm in Sections 3.2 and 3.3, respectively, the combined weights of evaluation indexes can be calculated according to the following formula:

Table 11: Driving behavior data.

| Start time | End time | Vehicle type | Bad driving behavior | The last time (s) | Alarm location (latitude and longitude) |
|---|---|---|---|---|---|
| 2020-8-1 1:43 | 2020-8-1 1:43 | Tractor | Large throttle | 8 | 115.7339 \| 37.6072 |
| 2020-8-1 3:12 | 2020-8-1 3:12 | Tractor | Large throttle | 8 | 115.1235 \| 36.5906 |
| 2020-8-1 3:39 | 2020-8-1 3:39 | Tractor | Large throttle | 8 | 115.1118 \| 36.2635 |
| ⋮ | ⋮ | ⋮ | ⋮ | ⋮ | ⋮ |
| 2020-8-31 23:12 | 2020-8-31 23:12 | Tractor | Sudden braking | 1 | 113.2730 \| 23.4528 |
| 2020-8-31 23:13 | 2020-8-31 23:13 | Tractor | Neutral taxiing | 6 | 113.2775 \| 23.4523 |

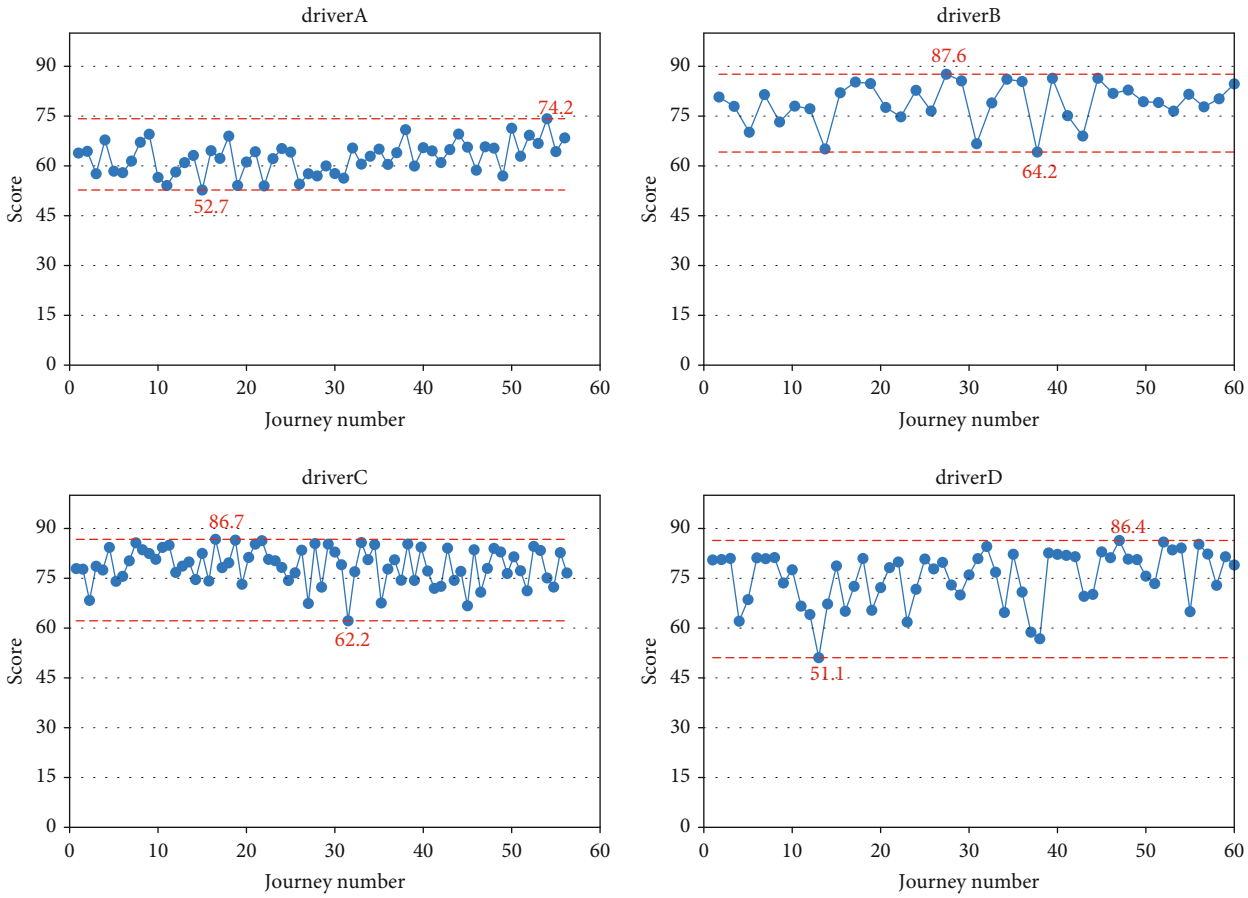


Figure 4: The scoring results of the top four drivers.

$$W_i = \frac{w_i v_i}{\sum_{i=1}^{n} w_i v_i}, i = 1, \cdots, n. \quad (23)$$

In Sections 3.2 and 3.3, $w$ is the weight of each evaluation index calculated based on AHP, and $v$ is the weight of each evaluation index calculated based on EWM. According to formula (23), the combined EW-AHP weight summary results can be obtained, as shown in Table 6.

In order to better analyze the weight proportion of each index, the weight bar chart of each evaluation index can be drawn, as shown in Figure 3. As can be seen from Figure 3, sudden braking is the most critical factor affecting the safety of commercial vehicle driving behavior, and the second factor is fatigue driving and rapid acceleration. Therefore, the improvement of the safety of commercial vehicles' driving behavior should be started from the following three aspects: emergency braking, fatigue driving, and rapid acceleration.

*3.5. Fuzzy Comprehensive Evaluation Algorithm and Implementation.* Section 2.3 has briefly introduced the steps of fuzzy comprehensive evaluation algorithm. This section will introduce in detail the specific implementation of the application of the Fuzzy comprehensive evaluation algorithm based on the EW-AHP combination weight to the safety evaluation of commercial vehicle driving behavior.

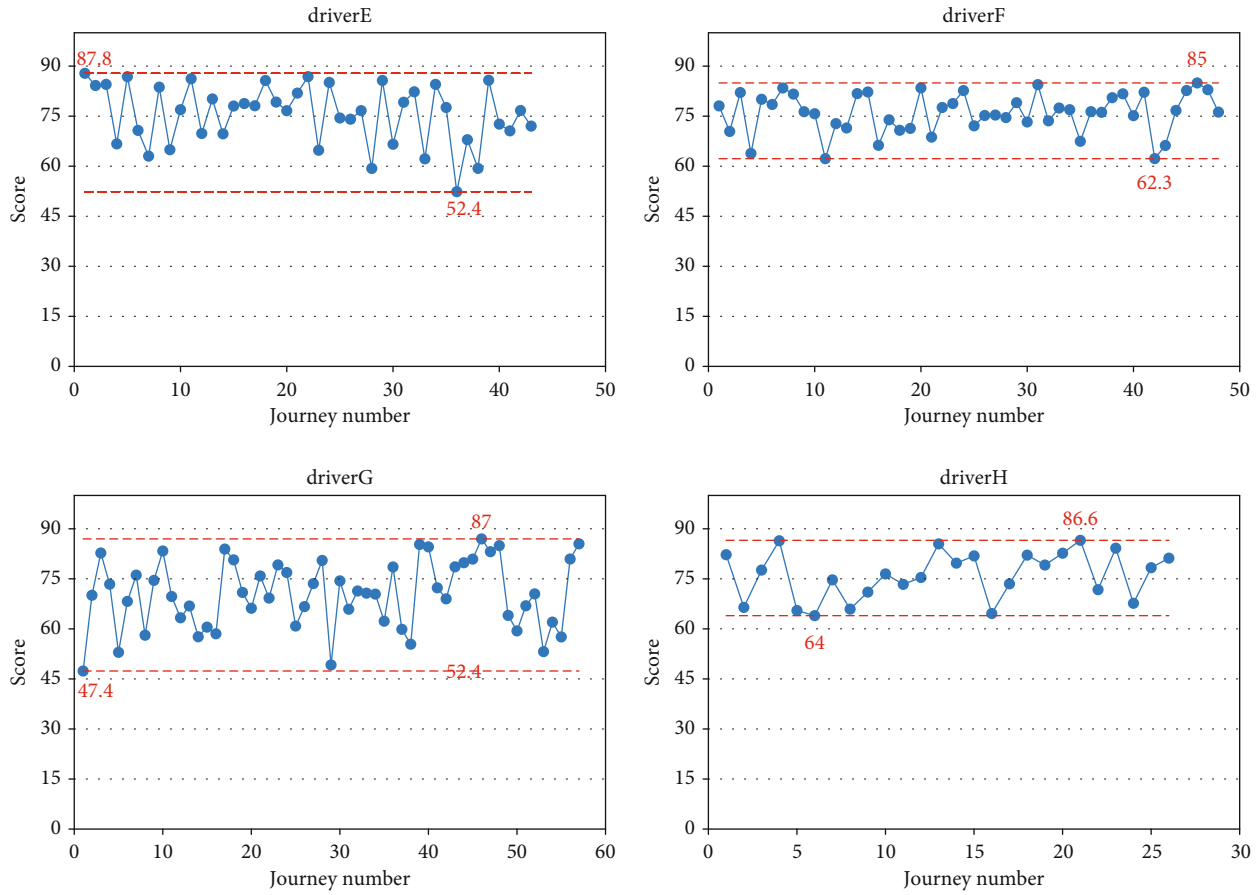


Figure 5: Scoring results of the last four drivers.

Table 12: Driver E score difference table.

| Indicators | Journey number | | | | | | | |
|---|---|---|---|---|---|---|---|---|
| | 36 | 33 | 42 | 35 | 17 | 39 | 11 | 5 |
| DM | 748.7 | 329.2 | 102.4 | 253.4 | 278.2 | 198.8 | 174 | 197.4 |
| NEA | 34 | 11 | 6 | 5 | 2 | 2 | 0 | 0 |
| NEB | 2 | 2 | 0 | 0 | 0 | 0 | 0 | 0 |
| POT | 0.03 | 0.02 | 0.00 | 0.00 | 0.03 | 0.00 | 0.00 | 0.00 |
| NHSLG | 80 | 2 | 0 | 0 | 1 | 2 | 4 | 0 |
| NFD | 1 | 1 | 0 | 0 | 0 | 0 | 0 | 0 |
| Score | 52.36 | 62.21 | 76.69 | 77.61 | 78.12 | 85.78 | 86.22 | 86.84 |

*3.5.1. Establish Driving Behavior Factors Set for Commercial Vehicles.* According to Figure 2, the factor set can be established as follows:

$$\begin{aligned} U &= \{U_1, U_2, U_3\}, \\ U_1 &= \{U_{11}, U_{12}, U_{13}, U_{14}\}, \\ U_2 &= \{U_{21}, U_{22}, U_{23}\}, \\ U_3 &= \{U_{31}, U_{32}, U_{33}, U_{34}\}. \end{aligned} \tag{24}$$

*3.5.2. Establish Evaluation Set on Commercial Vehicle Driving Behavior.* In order to quantify the final driving behavior evaluation score between 0 and 100, it is necessary to determine the corresponding score of each evaluation level while determining the evaluation set. Therefore, the evaluation set on the driving behavior of commercial vehicles can be established as follows:

$$V = \{\text{Excellent, Good, Average, Poor, Very Poor}\}. \tag{25}$$

The corresponding scores of each rating level can be established according to different driving conditions, as shown in Table 7.

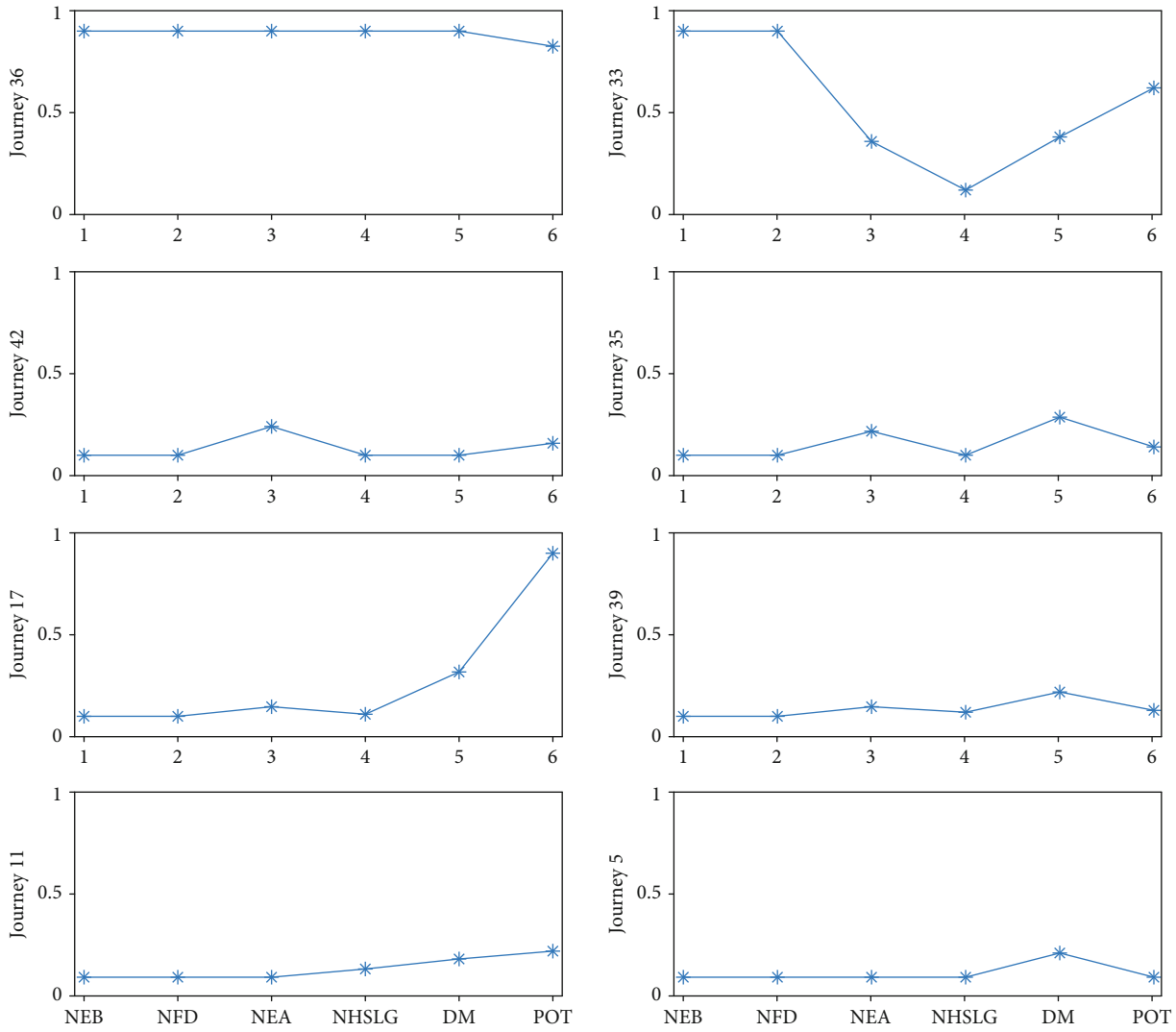


Figure 6: Data normalization results of driver E.

*3.5.3. Determine the Weight Vector of Each Evaluation Indicator.* According to Table 6, the normalized result of index weight is:

$$\begin{aligned} W &= (0.1311, 0.5267, 0.3422), \\ W_1 &= (0.5805, 0.2677, 0.1379, 0.0149), \\ W_2 &= (0.2262, 0.6632, 0.1106), \\ W_3 &= (0.1977, 0.1876, 0.2622, 0.3524). \end{aligned} \tag{26}$$

*3.5.4. Determine the Membership Function.* Due to the different characteristics of each evaluation index, the membership of each index cannot be reasonably explained by using only one membership function. Therefore, this paper proposes a method of using multiple membership functions to explain the membership of the selected evaluation index separately. After repeated experiments and comparisons of membership functions, the selection scheme of multiple membership functions as shown in Table 8 was finally determined.

In Equations (11)–(19), the parameters $a$, $b$, $c$, and $d$ are replaced by $x_i$. The reference value of membership function is different for different indicators. The calculation formula of reference value of membership degree of each indicator is as follows:

$$I_i(x_i) = \text{mean}(I_i) \pm |5 - i| \times \text{STD}(I_i). \tag{27}$$

In formula (27), if $i$ is less than 5, it takes a negative sign; otherwise, it takes a positive sign. $I_i(x_i)$ is the reference value of the membership degree of the $i$th grade of the $i$th index, $\text{mean}(I_i)$ is the mean of the data column in which the $i$th index is located, and $\text{STD}(I_i)$ is the standard deviation of the data column of the $i$th index.

For the reference value of membership degree of driving mileage, we divide its maximum value and minimum value into equal parts. The other indexes are calculated according to formula (27) and then dynamically adjusted. The reference values of each index to each grade of membership are shown in Table 9.

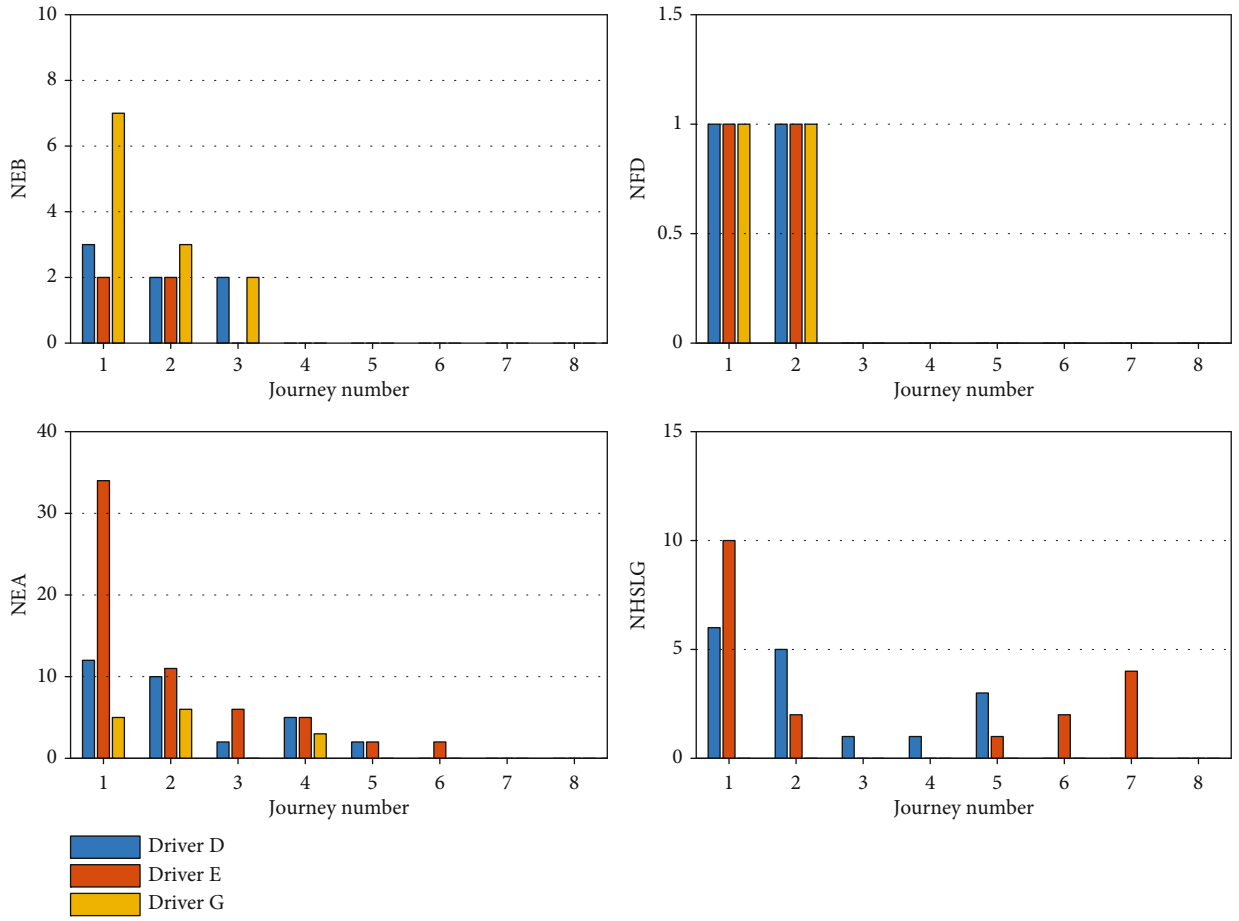


Figure 7: Comparison chart of the first 6 indicators.

Because the number of emergency braking and fatigue alarm is the rectangle function (with fewer parameters), it is different from the other two membership functions. According to the different data characteristics, the membership scheme of the two indexes is as follows: if the number of emergency braking is zero times, it belongs to the excellent level; if one time, it belongs to the good level; if two times, it belongs to the average level; if three times, it belongs to the poor level; if over three times, it belongs to the very poor level. If the number of fatigue alarm is zero times, it is classified as excellent, one time is poor, and more than one time is very poor. Finally, according to formulas (20)–(22), the fuzzy comprehensive evaluation matrix can be calculated to achieve the quantitative scoring of commercial vehicle driving behavior.

## 4. Validation and Results

The vehicle driving data of several sections of a company in August were selected, including "Hangzhou-Harbin," "Guangzhou-Changchun," and "Guangzhou-Hefei." Then, the vehicle travel data was divided into various journeys (the engine running from start to stop and the driving distance greater than 10 km was classified as a complete journey). All the travel data of 8 drivers within one month were selected from these three roads, and a total of 403 complete journeys were divided. The original driving data and driving behavior data of one of the drivers are shown in Tables 10 and 11.

The quantitative scoring model of commercial vehicle driving safety established in this study can calculate the scores of 8 drivers, and the results are shown in Figures 4 and 5.

By comparing the final scores of the eight drivers, it can be seen that the scores of driver A are generally low, and the scores are stable without great fluctuations. Therefore, we can think that the driving style of driver A belongs to the nonstandard driving type with low driving safety; however, driver B, driver C, driver F, and driver H have relatively high overall and stable scores. Therefore, we can conclude that they have normative and stable driving styles with high driving safety. The scores of driver D, driver E, and driver G are both high and low, and the scores fluctuate greatly. Therefore, it can be considered that the driving styles of them belong to the random type of driving with unstable driving safety. The final driving behavior score obtained by referring to the comprehensive evaluation model can standardize the driving style of nonstandard drivers and encourage drivers to maintain the standard driving, which is conducive to improve the safety of road traffic.

As can be seen from Figure 3, the total weight of the first six indicators exceeds 80%, so the analysis of these six

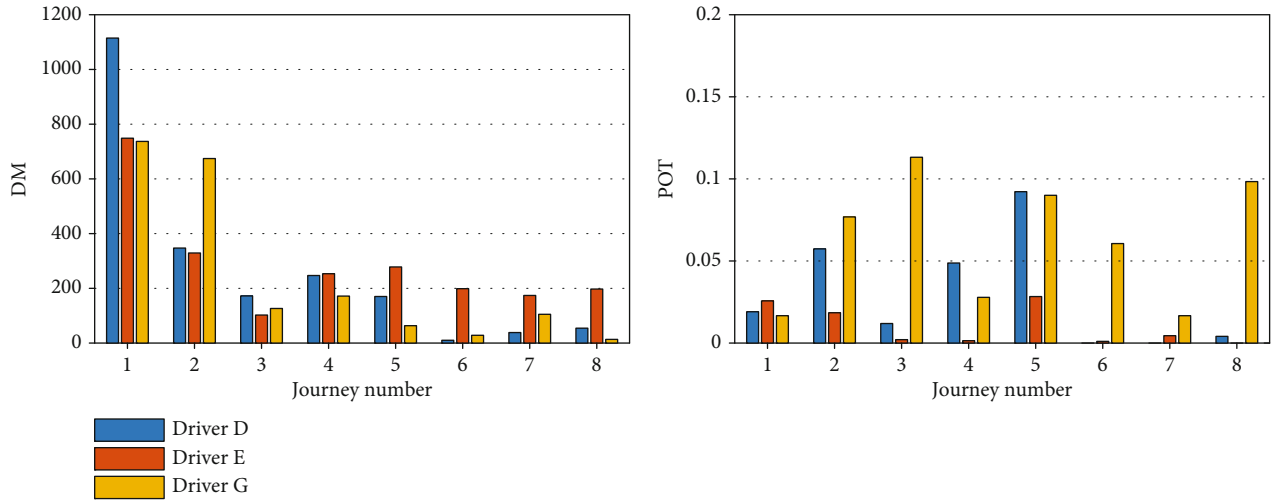


Figure 8: Comparison chart of the last 5 indicators and scores.

indicators is sufficient to prove the rationality of our evaluation model. We choose drivers D, E, and G whose scores fluctuated greatly for in-depth analysis. For the analysis of a single driver, such as driver E, we selected 8 journeys with significant differences. The scores of the 8 journeys are shown in Table 12. In order to better verify our model, each indicator in Table 12 is normalized, and the line diagram as shown in Figure 6 can be drawn.

As can be seen from Figure 6, for journeys with low scores (such as journeys 36 and 33), they have a poor performance in indicators with high weight (such as emergency braking and fatigue driving), so they have the lowest score. On the contrary, for journeys with high scores (such as journeys 39, 11, and 5), they perform well in all indicators and thus have higher scores. For journeys with medium scores (such as journeys 42, 35, and 17), they performed more modestly (neither too much nor too little) on all indicators and so scored moderately. By analyzing all the journeys of the other seven drivers, we can find that their scores were consistent with our analysis.

By comparing the 8 journeys with significantly different scores of drivers D, E, and G, a multidriver score comparison diagram can be drawn, as shown in Figures 7 and 8. Among them, low-scoring journeys include journeys 1 and 2, medium-scoring journeys include journeys 3, 4, and 5, and high-scoring journeys include journeys 6, 7, and 8.

Figures 7 and 8 compared and analyzed the scores of drivers D, E, and G. It is obvious that the three drivers perform poorly in various driving behavior indicators of journeys 1 and 2 (such as a large amount of emergency braking, emergency acceleration, and fatigue driving), so the score is low. With the decrease of bad driving behavior performance, the score increases accordingly. Therefore, our model can reasonably achieve the quantitative evaluation of the safety of commercial vehicle driving behavior.

## 5. Conclusion

In this study, a commercial vehicle driving safety evaluation model combining EW-AHP and fuzzy comprehensive evaluation algorithm is proposed as a method basis for studying the relationship between driving risks, risk causes, and quantification of driving behaviors. Based on the natural driving data of commercial vehicles, a safety evaluation system for commercial vehicle driving behavior based on AHP was established, which combines four main aspects of driving behavior characteristics including driving mileage, driving speed, acceleration, and bad driving behavior.

Based on EW-AHP, the weight coefficient of each evaluation index is effectively determined, which solves the problem that the traditional AHP algorithm is too subjective and finds out the key causes affecting the driving risk, which are emergency braking, fatigue driving, and rapid acceleration, respectively. In view of the different characteristics of each evaluation index, it is hard to explain the membership of each index by using only one membership function. Therefore, a method to explain the membership of each evaluation index by using the multimembership function is proposed. Compared with previous studies, this model can not only distinguish safe and unsafe drivers but also identify driving styles and achieve quantitative scoring of driving behavior safety. The model is tested by using the actual driving data of multiple sections and the effectiveness of the proposed method is verified.

The results of this study can be used to quantitatively evaluate the driving behavior of commercial vehicle drivers, standardize driving, and help drivers develop good driving habits to improve road traffic safety. In the future research, there are still some limitations and improvements worth noting. For example, although this study is based on multiple roads driving data, the data of roads can be more comprehensive and extensive. In addition, the research scope can not only be limited to drivers' driving behaviors but also include more factors (such as environmental factors, roads, and drivers' emotions).

## Data Availability

The data used to support the findings of this study are available from the corresponding author upon request.

## Conflicts of Interest

The authors declare that there is no conflict of interest regarding the publication of this paper.

## Acknowledgments

This work was supported in part by the project of National Natural Science Foundation of China under grant 51965013, in part by the Science and Technology Major Project of Guangxi under grant AA18242033 and grant AA19182004, in part by the Key Research and Development Program of Guangxi (AB21196029), in part by the Guangxi Natural Science Foundation Program (grants 2020GXNSFAA159081 and 2018GXNSFAA281276), in part by the Scientific Research and Technology Development in Liuzhou (2020GAAA0404, 2021AAA0104, and 2021AAA0112), in part by the Guangxi Science and Technology Base and Special Talents Program (grant 2018AD19077), and in part by the Guangxi Key Laboratory of Manufacture System and Advanced Manufacture Technology under grant 17-259-05-009Z.

## References

[1] X. M. Zhao, Q. Li, D. F. Xie et al., "Risk perception and the warning strategy based on microscopic driving state," *Accident Analysis & Prevention*, vol. 118, pp. 154–165, 2018.

[2] F. Sagberg, Selpi, G. F. Bianchi Piccinini, and J. Engström, "A review of research on driving styles and road safety," *Human Factors*, vol. 57, no. 7, pp. 1248–1275, 2015.

[3] F. Guo and Y. J. Fang, "Individual driver risk assessment using naturalistic driving data," *Accident Analysis & Prevention*, vol. 61, pp. 3–9, 2013.

[4] O. S. Siordia and I. M. Diego, "Driving risk classification based on experts evaluation," in *2010 IEEE Intelligent Vehicles Symposium*, pp. 1098–1103, La Jolla, CA, USA, 2010.

[5] L. Y. Chang and W. C. Chen, "Data mining of tree-based models to analyze freeway accident frequency," *Journal of Safety Research*, vol. 36, no. 4, pp. 365–375, 2005.

[6] L. Y. Chang and H. W. Wang, "Analysis of traffic injury severity: an application of non-parametric classification tree techniques," *Accident Analysis & Prevention*, vol. 38, no. 5, pp. 1019–1027, 2006.

[7] X. Y. Zhu, Y. F. Yuan, X. Hu, Y. C. Chiu, and Y. L. Ma, "A Bayesian network model for contextual versus non-contextual driving behavior assessment," *Transportation Research Part C: Emerging Technologies*, vol. 81, pp. 172–187, 2017.

[8] J. Q. Wang, Y. Zheng, X. Li, C. Yu, K. Kodaka, and K. Li, "Driving risk assessment using near-crash database through data mining of tree- based model," *Accident Analysis & Prevention*, vol. 84, pp. 54–64, 2015.

[9] X. G. Li, D. Lord, Y. Zhang, and Y. Xie, "Predicting motor vehicle crashes using support vector machine models," *Accident Analysis & Prevention*, vol. 40, no. 4, pp. 1611–1618, 2008.

[10] F. Guo, S. G. Klauer, J. M. Hankey, and T. A. Dingus, "Near crashes as crash surrogate for naturalistic driving studies," *Transportation Research Record*, vol. 2147, no. 1, pp. 66–74, 2010.

[11] J. H. Hong, B. Margines, and A. K. Dey, "A smartphone-based sensing platform to model aggressive driving behaviors," in *Proceedings of the 32nd annual ACM conference on Human factors in computing systems*, pp. 4047–4056, Toronto, Ontario, Canada, 2014.

[12] A. E. Af Wåhlberg, "Driver celeration behaviour and accidents – an analysis," *Theoretical Issues in Ergonomics Science*, vol. 9, no. 5, pp. 383–403, 2008.

[13] J. Jun, R. Guensler, and J. Ogle, "Differences in observed speed patterns between crash-involved and crash-not- involved drivers: application of in-vehicle monitoring technology," *Transportation Research Part C: Emerging Technologies*, vol. 19, no. 4, pp. 569–578, 2011.

[14] M. Ayuso, M. Guillén, and A. M. Pérez Marín, "Using GPS data to analyse the distance travelled to the first accident at fault in pay-as-you-drive insurance," *Transportation Research Part C Emerging Technologies*, vol. 68, pp. 160–167, 2016.

[15] M. Ayuso, M. Guillén, and A. M. Pérez-Marín, "Time and distance to first accident and driving patterns of young drivers with pay-as-you-drive insurance," *Accident Analysis & Prevention*, vol. 73, pp. 125–131, 2014.

[16] B. G. Simons-Morton, K. Cheon, F. Guo, and P. Albert, "Trajectories of kinematic risky driving among novice teenagers," *Accident Analysis & Prevention*, vol. 51, pp. 27–32, 2013.

[17] O. Bagdadi and A. Várhelyi, "Jerky driving-an indicator of accident proneness?," *Accident Analysis & Prevention*, vol. 43, no. 4, pp. 1359–1363, 2011.

[18] W. B. Lee, H. Lau, Z. Z. Liu, and S. Tam, "A fuzzy analytic hierarchy process approach in modular product design," *Expert Systems*, vol. 18, no. 1, pp. 32–42, 2001.

[19] R. T. Cheng, C. F. Wang, and G. W. Lv, "Research on safe driving scoring system and personalized ratemaking of vehicle insurance based on OBD data," in *ICCSE'18: Proceedings of the 3rd International Conference on Crowd Science and Engineering*, pp. 1–8, New York, USA, 2018.

[20] Z. S. Liu, Q. H. Shen, and H. Li, "A risky driving behavior scoring model for the personalized automobile insurance pricing," in *ICCSE'17: Proceedings of the 2nd International Conference on Crowd Science and Engineering*, pp. 61–67, Beijing, China, 2017.

[21] Y. Wang, Y. Li, W. Liu, and Y. Gao, "Assessing operational ocean observing equipment (OOOE) based on the fuzzy comprehensive evaluation method," *Ocean Engineering*, vol. 107, pp. 54–59, 2015.

[22] L. J. Guo, J. J. Gao, J. F. Yang, and J. Kang, "Criticality evaluation of petrochemical equipment based on fuzzy comprehensive evaluation and a BP neural network," *Journal of Loss Prevention in the Process Industries*, vol. 22, no. 4, pp. 469–476, 2009.

[23] M. G. Dong, S. Y. Li, and H. Y. Zhang, "Approaches to group decision making with incomplete information based on power geometric operators and triangular fuzzy AHP," *Expert Systems with Applications*, vol. 42, no. 21, pp. 7846–7857, 2015.

[24] F. A. Lootsma, "Scale sensitivity in the multiplicative AHP and SMART," *Journal of Multi-Criteria Decision Analysis*, vol. 2, no. 2, pp. 87–110, 1993.

[25] H. F. Lin, "An application of fuzzy AHP for evaluating course website quality," *Computers & Education*, vol. 54, no. 4, pp. 877–888, 2010.

Hindawi
Journal of Sensors
Volume 2021, Article ID 9921101, 13 pages
https://doi.org/10.1155/2021/9921101

*Research Article*

# Detail 3D Face Reconstruction Based on 3DMM and Displacement Map

**Tianping Li, Hongxin Xu, Hua Zhang, and Honglin Wan**

*Key Laboratory of Medical Physics and Image Processing in Shandong Province, Shandong Normal University, School of Physics and Electronics, Jinan, Shandong, China*

Correspondence should be addressed to Hua Zhang; jnzhhua@126.com

Received 12 March 2021; Revised 19 April 2021; Accepted 8 June 2021; Published 25 June 2021

Academic Editor: Aijun Yin



How to accurately reconstruct the 3D model human face is a challenge issue in the computer vision. Due to the complexity of face reconstruction and diversity of face features, most existing methods are aimed at reconstructing a smooth face model with ignoring face details. In this paper a novel deep learning-based face reconstruction method is proposed. It contains two modules: initial face reconstruction and face details synthesis. In the initial face reconstruction module, a neural network is used to detect the facial feature points and the angle of the pose face, and 3D Morphable Model (3DMM) is used to reconstruct the rough shape of the face model. In the face detail synthesis module, Conditional Generation Adversarial Network (CGAN) is used to synthesize the displacement map. The map provides texture features to render to the face surface reconstruction, so as to reflect the face details. Our proposal is evaluated by Facescape dataset in experiments and achieved better performance than other current methods.

## 1. Introduction

Face is one of the most important biological characteristics of human beings, and face modeling is often used in security, animation, biometrics, and other fields [1, 2]. In recent years, due to the limitations of 2D images, the research of human face has gradually shifted from 2D plane images to 3D space models.

The steps of 3D face reconstruction are very complex if it is reconstructed step by step. Moreover, this reconstruction model will lead to more data loss and less accuracy. To stress this issue, one-step reconstruction model is presented (see Figure 1). The reconstruction system is divided into two parts: the initial face reconstruction module and the face detail synthesis module, and both are based on deep learning [3]. The initial face reconstruction module is mainly responsible for face alignment. The supervised learning method is used to train 60K face images from 300W-LP dataset to obtain the corresponding dictionary. In this process, a CNN network is used to align the negative faces and detect their feature points. The feature points are input into the principal component analysis- (PCA-) based 3DMM [4] to obtain a rough face shape. The face detail synthesis module is based on CGAN, which inputs the original image to synthesize the displacement map, and the displacement map retains the more complete details of the face [5]. The face detail synthesis module refers to DFDN to train high-quality images and get the training data, which can synthesize the displacement map from the original image.

In this paper, we propose a reconstruction system to recover the details of the face model. Our reconstruction system can better solve the problem of face pose reconstruction and facial expression reconstruction from the input image. The facial detail synthesis module of the reconstruction system can extract facial features from the input image and synthesize the displacement map containing most of the details of the target face. Compared with the initial shape model, the detail face model with displacement map has better visual effect and more accurate data.

The rest of the paper is organized as follows. Section 2 describes the researchers' related work on 3D face. Section 3 describes the initial face reconstruction module. Section 4

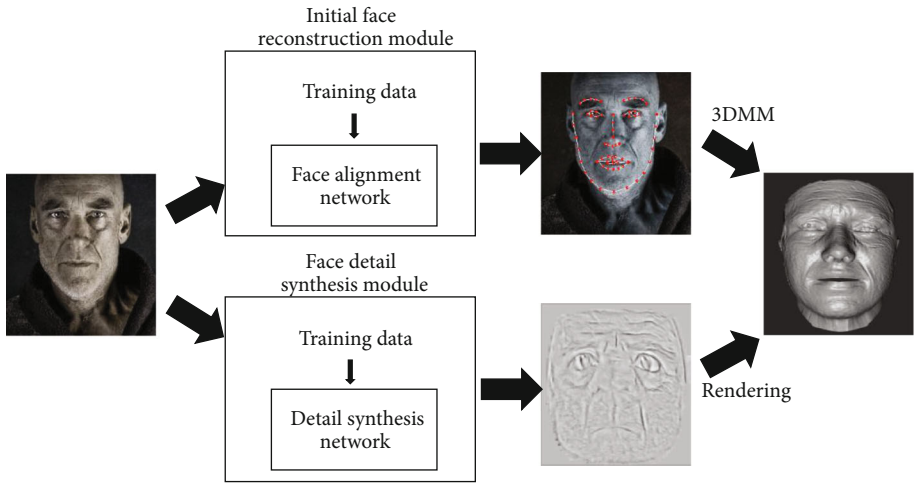


Figure 1: Reconstruction system structure.

describes the face detail synthesis module. Section 5 is the experiment and analysis. Section 6 concludes the paper.

## 2. Related Work

With the application of deep learning methods to graphics, the transition from 2D planar images to 3D spatial models has become one of the popular research directions. Blanz et al. proposed the concept of 3DMM and obtained a Basel Face Model (BFM) by training the objects and related data collected by the depth camera [6]. The parameterized BFM has the universal characteristics of a human face, and a deformed 3D model can be obtained by inputting shape, texture, and attribute parameters. A large number of 3DMM-based algorithms have been proposed. Tran et al. proposed a nonlinear 3D face deformation model method [7], which used a large number of unconstrained pictures as training objects to train a new architecture of 3DMM without using 3D scanning equipment. Galteri et al. used CGAN to refine 3DMM [8].

In addition to traditional 3DMM, an end-to-end method based on deep learning can also better reconstruct 3D face models. The end-to-end method can perform face alignment on the input face image. In the vector space, the detected feature points are mapped to the face model of the dense point cloud one by one. This method is simple and fast. Compared with the traditional 3DMM, its accuracy is higher in most cases. Yao et al. designed PRNet [9] based on the CNN network structure and deep residual network and used the UV vector space to complete the mapping of the 3D face model. Jackson et al. proposed a combination of 3DMM and CNN VRN [10] to reconstruct the model of nonfrontal face images. Tran et al. used the end-to-end neural network to reconstruct the details of extreme face [11].

The rendering of face model is also a key part. Ranjan et al. proposed COMA method to generate the head network and used an MPI-IS Mesh Processing Library for rendering [12]. MPI-IS Mesh Processing Library is an efficient 3D model rendering tool. Li et al. designed a Flame model to render the basic shape and expression of the face model [13]. Sanyal et al. proposed RingNet based on Flame [14]. RingNet can reconstruct the head model by inputting face image and can better simulate the facial expression. A deep 3D face reconstruction method was proposed by Deng et al. [15]. This method is based on 3DMM and coarse facial expression [16], and the rendered model is more accurate.

## 3. Initial Face Reconstruction Module

The initial face reconstruction module is the key module in proposed reconstruction system. This module outputs the input face image directly to the rough initial face model, which includes pose face alignment, feature point detection, and model fitting.

### 3.1. Construction of Rough Face Model

*3.1.1. Face Alignment.* In our method, the feature point coordinates are used as the input of 3DMM based on the PCA algorithm to construct a parameterized model.

Because the manual labeling is time-consuming and labor-intensive, and the traditional feature point detection is poor in robustness and accuracy, we use a CNN to deal with the face alignment of nonfrontal face images. This article uses the DLIB library to detect feature points. DLIB library uses regression tree set cascade [17] to generate feature point model through supervised learning and training image sets with feature point annotations. Input an image, the algorithm will generate the initial shape based on the target face and roughly estimate the location of the feature points. Then, a gradient boosting algorithm is used to reduce the error between the initial shape and the real landmark, and the least square method is used to minimize the error to obtain the cascade $r_t$ of each stage.

$$\widehat{S}^{t+1} = \widehat{S}^t + r_t\left(I, \widehat{S}^t\right), \tag{1}$$

where $t$ is the number of cascade regressions, $\widehat{S}^t$ is the shape vector of the $t$th secondary cascade regression, and $I$ is the

Figure 2: Feature point detection.

input image. The key point of the cascade is that the regressor $r_t$ predicts according to the image pixel intensity value and indexes it relative to the current shape vector $\widehat{S}^t$. The feature points of a nonfrontal face image are divided into two parts: visible and invisible. Since the latter is difficult to predict, deep learning methods can effectively deal with this problem.

We train 60K face images with face deflection angle data and feature point coordinate data in the 300W-LP dataset [18] to obtain a dictionary. Through the index dictionary, the output finds the index target that is closest to the deflection angle of the input face image. In addition, referring to the weight setting of the main components of the human face by referring to the PRNet, the feature points in the vicinity of the eyes, nose, and mouth are given greater weights to highlight the changes and recognition of the model

$$l_{fp} = M_{face} * W_{fp}, \tag{2}$$

where $M_{\text{face}}$ detects the coordinates of face feature points and $W_{fp}$ is the weight. Figure 2 shows an example of feature point detection.

*3.1.2. 3DMM Face Reconstruction.* A rough face model with a smooth surface is relatively average, without too much facial detail but contains most of the depth information of the face. Inputting the face image fitting model will change the vertex, and the topological network of the BFM will average face model. The method in this paper employ BFM2017 [19] to fit a 3D face with less detail.

Taking the original image as input, assuming that the grid vertex coordinates of the 3D model are $S = (x_i, y_i, z_i)$. The feature points according to Equation (2) are used to calculate the PCA parameters. According to [6], $n$ shape vectors of the initial face model is

$$S_{\text{shape}} = \sum_{i}^{n} \alpha_i S_i, \tag{3}$$

where $\alpha_i$ is the shape weight coefficient.

According to the average face shape $\bar{S}$ obtained from the training set of 200 images, the difference between the shape of each face model and the average face shape $\Delta S_i = S_i - \bar{S}$ calculates the covariance matrix $C_S$ of the shape vector. Through PCA, the orthogonal coordinate system formed by the eigenvector $s_i$ of $C_S$ is transformed into the basis:

$$S_{\text{mod el}} = \bar{S} + \sum_{i=1}^{m-1} \alpha_i s_i. \tag{4}$$

Due to the universality of main features of human face, the distribution of shape vector parameter $\alpha_i$ is normal

distribution (as shown in Equation (5)). Texture parameters are similar to shape parameter.

$$p(\alpha) \sim \sim \exp\left(-\sum_{i=1}^{m-1}\frac{\alpha_i^2}{2\sigma^2}\right). \tag{5}$$

For the shape parameter $\alpha$, texture parameter $\beta$, and attribute parameter $\gamma$, the RGB vector of the projected image of the reconstruction model is

$$I_{\text{mod el}}(x,y) = \left(I_r(x,y), I_g(x,y), I_b(x,y)\right)^T. \tag{6}$$

The error between the projected image of the reconstructed model and the input image is

$$E_{\text{image}} = \sum_{x,y}\left\|I_{\text{input}}(x,y) - I_{\text{mod el}}(x,y)\right\|^2. \tag{7}$$

Matching the input face image with the 3D modeled face is an ill-posed problem. In the vector space of the face model, the matching quality and a priori method can be used to obtain the solution with constraints [6]. Similar to Equation (5), $p(\alpha)$ and $p(\beta)$ obey normal distribution, $p(\gamma)$ is obtained by the point-to-point method. According to Bayesian decision, the input image can be obtained through the maximum posterior probability with the parameters $(\alpha, \beta, \gamma)$, and the model $I_{\text{model}}$ is reconstructed through the three parameters. But under the influence of noise, the observed image $I_{\text{input}}$ will be disturbed.

Assuming the standard deviation $\sigma_G$ of the Gaussian noise of the observed image, the parameter probability of the observed image is

$$p(\alpha,\beta,\gamma) = \exp\left(-\frac{1}{2\sigma_G^2}\cdot E_1\right). \tag{8}$$

The posterior probability of the parameter is expressed by minimizing the cost function:

$$E = \frac{1}{\sigma_G^2}E_1 + \sum_{i=1}^{m-1}\frac{\alpha_i^2}{\sigma_{S,i}^2} + \sum_{i=1}^{m-1}\frac{\beta_i^2}{\sigma_{T,i}^2} + \sum_i\frac{(\gamma_i-\bar{\gamma}_i)^2}{\sigma_{\gamma,i}^2}. \tag{9}$$

### 3.2. Camera Model

*3.2.1. Weak Perspective Projection Function.* To visualize a 3D model, the topology of the 3D model needs to be projected onto a two-dimensional plane. Compared with orthogonal projection, perspective projection can freely set the reduction and enlargement of the projected image.

During the projection process, it may appear that the dense 3D coordinates are superimposed on the 2D coordinate points of the projection surface due to dimensionality reduction. Aiming at the projection of the pose face model, this paper uses a weak perspective projection function similar to the perspective projection function to deal with the problem of projecting a 3D model onto a 2D plane [20]. Figure 3 explains the difference between orthographic projection and weak perspective projection.

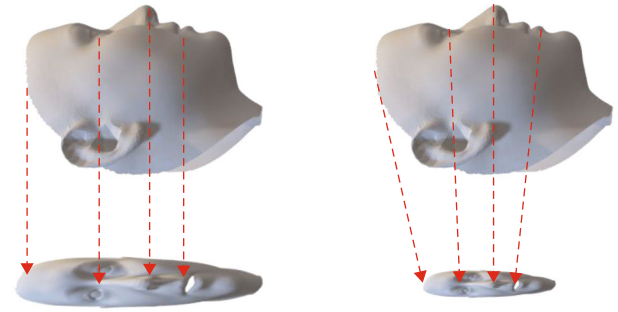

Figure 3: Orthogonal projection and weak perspective projection.

In this paper, assuming that the positive direction of the camera model is the weak perspective projection in the $z$ direction, referring to [21], we use the orthogonal projection matrix $\Lambda \in \mathbb{R}^{3\times3}$ and the target displacement calibration $x$ to design the weak perspective projection function:

$$P = f * \Lambda * R * S_{\text{mod el}} + x. \tag{10}$$

Optimizing Equation (10),

$$P = \sum_{i=1}^{n}\|f * \Lambda * R * \alpha_i S_i\| + x_i, \tag{11}$$

where $f$ is the focal length ratio, $R$ is the rotation matrix, and $x_i$ is the displacement coefficient of the $i$th vertex coordinate. The weak perspective projection function projects the normalized face mesh vertices from the 3D space to the 2D plane, which is convenient for subsequent operations and processing.

Minimize the error of projecting the initial reconstruction model based on the PCA algorithm to the plane [22]:

$$E = \sum_{\text{k}}\omega_{\text{k}}\|L_{\text{k}}\text{-}P(\text{l}_{\text{k}}(\alpha,\beta))\|_2 + \lambda_k\|\alpha\|_2, \tag{12}$$

where $L_k$ is the $k$th feature point of the planar face, $l_k(\alpha, \beta)$ is the coordinates of the $k$th vertex of the 3D model, $\omega_k$ is the weight of the $k$th feature point, and $\lambda_k$ is the regularization coefficient of the shape parameter.

*3.2.2. Hidden Surfaces Remove.* In the dense 3D mesh, under nonfrontal face conditions, some vertices will always overlap, which affects the result and accuracy of feature point acquisition. In this paper, the $z$-buffer algorithm [23] is used to solve the ambiguity of the depth value.

The $z$-buffer algorithm buffers the depth value of the visible surface into the depth buffer area, and the depth value of the hidden surface is removed. So, the single view only has the depth of the visible surface. The depth $z$ value is not the true Euclidean distance of the Cartesian space coordinate system, but a relative measure of the distance from the vertex to the viewpoint. Assuming that the model is viewed from the perspective of the $z$-axis as the positive direction, the projection surface is the $xoy$ plane. $(x, y)$ is the coordinates of each

(a) (b) (c)

Figure 4: The difference between using $z$-buffer depth map. (a) Original image. (b) Depth map using $z$-buffer. (c) Depth map without $z$-buffer.

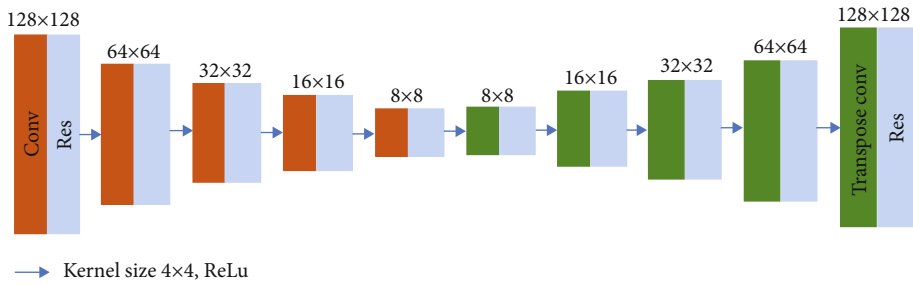


Figure 5: Face alignment network structure.

pixel in the overlapping area of the projection surface. The ray parallel to the $z$-axis are the depth values, which are $z_1$ and $z_2$, respectively, and the maximum of $(z_1,z_2)$ is stored in the $z$-buffer.

Figure 4 demonstrates the difference between whether to use the $z$-buffer depth map. The depth map of the depth map using the $z$-buffer algorithm is distinct, and there is no ambiguity in the depth value due to the posture self-occlusion caused by a single perspective.

*3.3. Face Alignment Network.* The purpose of the face alignment is to obtain a dictionary through training. The input face image is indexed after face detection, etc., and then, the angle of the target face relative to the frontal perspective can be obtained, and the target face can be aligned [24]. The face alignment obtains the angle of the target face with the feature point detection of DLIB library and the improved feature point loss function. When the input is a face image with a large pose, not only the visible feature points can be accurately detected but also the feature points that are invisible due to the posture self-occlusion can be predicted more accurately.

Test an image in the test set $n$ times, and take the average value of its location map feature points. Improved loss function $L_{fp}$:

$$L_{fp} = \sum \left\| \bar{S} - S_{GT} \right\| * W_{fp}, \tag{13}$$

where $\bar{S}$ is the average value of $n$ tests of the feature point landmarks of the location map, $S_{GT}$ is the real landmark, and $W_{fp}$ is the weight of the feature points.

The face alignment network is a CNN architecture based on the residual network [25, 26], composed of 10 residual modules. Figure 5 is a diagram of the face alignment network structure.

When using the face alignment network training and the angle of the training set image corresponding to the annotation, 3D point cloud and additional parameters are used as the training object, and the projection normalized coordinate code (PNCC) feature [18] that can represent the shape of the model is used to generate a dictionary.

PNCC is composed of normalized coordinate code (NCC) and $z$-buffer algorithm. NCC normalizes the coordinates $c = (x, y, z)$ of the vertices of the 3D average face model, and its calculation formula is

$$\mathrm{NCC} = \frac{\bar{S}_c - \min\left(\bar{S}_c\right)}{\max\left(\bar{S}_c\right) - \min\left(\bar{S}_c\right)}. \tag{14}$$

The purpose of PNCC is to use $z$-buffer algorithm to remove the hidden surface normalized by NCC to achieve the effect of projection. PNCC calculation formula:

$$\mathrm{PNCC} = z - \mathrm{buffer}(V_{3D}(\rho), \mathrm{NCC}), \tag{15}$$

Figure 6: Examples of texture map, normal map, and displacement map.

where $V_{3D}(\rho)$ is the 3D surface after projection and $\rho$ is a model parameter.

## 4. Face Detail Synthesis Module

In the initial face reconstruction module, although the 3DMM reconstruction model based on the PCA algorithm has most of the information of the reconstruction target, it loses part of the detailed information due to dimensionality reduction. We use a face detail synthesis module to make up for face detail information.

*4.1. Displacement Map Based on Texture Bump.* The details of the face include gullies and wrinkles, so it is difficult to detect and extract them with a unified standard method. Undifferentiated detection and detail extraction integration can effectively solve this problem. We uses the deep learning method to build a detailed synthesis network, which detects the face in the image and extracts the texture map of the face area, and synthesizes a displacement map based on the texture map.

The displacement map is similar to the normal map. Normal map highlights the unevenness of the model. The normal map represents the normal vector corresponding to the vertices, but cannot change the vertex coordinates of the model itself. Since all the details are only reflected in the map, the displacement map can use micropolygon tessellate [27] to change details of the model surface. For a 3DMM composing of triangular meshes, first, inlay a triangular structure with the same size as the image pixel size on the effective area of the model. The bump map is grayed out, and the depth $z$ coordinate is determined by the gray level. Then, according to the triangle mesh obtained by mosaic, the vertices are moved along the original surface normal direction. Then, determine the new normal vector for the new mesh vertex.

The lower $x$ and $y$ of the model's three-dimensional coordinates are represented by the $uv$ coordinates of the texture, i.e., the image color. $z$ coordinate is represented by the gray scale of the displacement map. The depth information of the shifted texture obtained by graying the texture is incomplete. The reason is that for face images, some face details may be treated as noise, or the depth of some details is too similar to the main area of the face, resulting in a large deviation of the model.

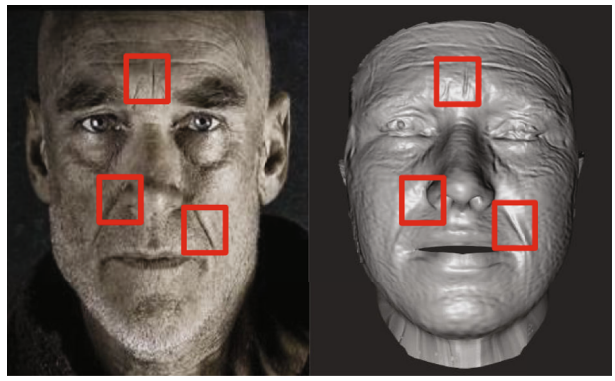

Figure 7: Rendered detailed model.

Our method proposes a detailed synthesis network based on the gray-scale displacement map, and the subtle details of the face are used as noise to extract the difficult-to-handle details of the texture map from the generator. The extracted detail noise is used as a feature map and cyclically synthesized to a displacement map. According to the gray value, the depth of the model is changed in a small amount to highlight the details. The pixels of the synthesized texture are $4096 * 4096$, and there are more pixels corresponding to details, which is more convenient for processing. The three images in Figure 6 are the RGB texture map, the normal map, and the displacement map.

In Figure 7, the red frame area of the detail model reconstructed by the method in this paper represents three details from small to large depth. Rendering the displacement map to the model can clearly see that the fit of different degrees of detail is relatively good.

*4.2. Facial Expression Process.* The recognition and fitting of facial expressions is a key problem that needs to be solved in the field of 3D face reconstruction. The dynamic changes and severity of the face will affect the analysis of the main components of the face. When projecting, because the 3D space dimensionality reduction will lose part of the information, the facial expression model will appear ambiguity when it is projected onto the 2D plane.

Our method mainly uses the expression fitting function of BFM2017 to realize the dynamic changes of the face. According to Equation (3), on the basis of the neutral expression face shape vector, an additional expression vector e is added to it, i.e.,

$$S_{\text{shape}} = \sum_{i}^{n} \alpha_i S_i + e_i. \tag{16}$$

However, the expression fitting function of BFM2017 mainly changes the mouth vector, and the fitting effect of other face parts is not ideal. Therefore this article uses a semantically defined emotion feature predictor and physical appearance features. The emotion feature predictor is based on deep learning training to obtain the corresponding expression parameters, and the appearance feature is the expression fitting of BFM2017.

Referring to the processing of facial dynamic expressions in DFDN, the emotion feature predictor is trained from a total of 450k images with 11 expressions in the AffectNet dataset [28]. The $e_{\text{predictor}} \in \mathbb{R}^{128}$ used to represent the feature vector of human emotion is obtained by the network training of CNN structure, and the emotion parameters are randomly generated in the standard normal distribution. The emotional feature vector with expression parameters is used to render the emotional image set, and the training set is input to the emotional feature predictor to obtain the feature vector of the face object in the image set [22]. The emotional feature vector is combined with the physical appearance feature to obtain a semantically defined feature vector.

According to the one-to-one correspondence between the feature vector of the image set and the expression parameter, a dictionary is set to represent the mapping of the feature vector to the expression parameter. Input a facial expression image, get its emotion feature vector through the emotion feature predictor, traverse the dictionary, and find the expression parameter closest to this vector.

*4.3. GAN-Based Detail Synthesis Network.* The Conditional Generative Adversarial Network (CGAN) [29] based on GAN is divided into two parts: generator network and discriminator network. The generator network randomly generates constrained images, and the generated images pass through the discriminator to perform feature threshold discrimination, save valid features, and cycle the generation-judgment process until the discriminator cannot determine the wrong image.

In this article, dealing with 3D face models, the loss function of CGAN is as follows:

$$V_{\text{GAN}}(D, G) = E_{x,y}[\log D(x \mid y)] + E_{x,z}[\log (1 - D(G(x \mid z)))], \tag{17}$$

where $x$ is the input image, $y$ is the feature point, and $z$ is random noise. Refer to [30], optimizing Equation (17):

$$\begin{cases} L_G = V_{\text{CGAN}}(D, G) + \lambda_1 L_1(G), \\ L_D = -V_{\text{CGAN}}(D, G), \end{cases} \tag{18}$$

where $L_G$ is the generator loss function, $L_D$ is the discriminator loss function, $L_1(G)$ is the generator's $L_1$ loss function, and $\lambda_1$ is set to 100.

The U-net model based on improved FCN [31] is a structure including down-sampling and up-sampling, with the purpose of increasing the accuracy of the image. Down-sampling is used to display environmental information, and up-sampling combines the environmental information from down-sampling with the input information of up-sampling to restore detailed information, making the texture of the human face more real.

This network uses the U-net-6 structure and takes the original target image as input, to generate displacement maps from the semantically defined texture structure map. The generator network and the 4-layer fully connected layer constrain the generated data through feature points and calculate the PCA parameters. Except for the fully connected layer, every linear part is activated by the ReLU function. The LeakyReLU function is used to activate between the fully connected layers. The structure of the U-net-6 network generator is shown in Figure 8.

The network discriminator judges the validity of the output image through the threshold. In this paper, the discriminator is based on PatchGAN [32]. The input image is divided into an $N \times N$ matrix, and after convolution, an $m \times m$ matrix is output. The output matrix is averaged, the threshold is judged, and the logical result is output. The network structure of the discriminator is shown in Figure 9.

## 5. Experiment and Discussion

*5.1. Face Alignment Evaluation.* The visible and invisible feature points of nonfrontal faces obtained by face alignment will directly affect the subsequent initial face reconstruction. In our evaluation experiment, the normalized mean error (NME) calculated by comparing with real landmarks represents the accuracy of feature points.

For the face alignment experiment, this article uses the 300W-LP dataset as the training set. The dataset contains faces deflection from 0 to 90 degrees, with a total of more than 60K images. Use the DLIB library to detect human faces and crop each image into a $256 \times 256 \times 3$ face image.

Aiming at the accuracy evaluation of the feature points of face poses at different angles, this paper randomly selects 1000 images from 300W-LP dataset. Calculate the average of the normalized mean error (NME) between the 68 detected feature points of the face and the real landmarks to evaluate the accuracy in this paper. In addition, we compare our method with other two advanced face alignment methods PRNet and 3DDFA. The results obtained are shown in Figure 10.

According to Figure 10, compared with the other two methods, our method can get better results in the feature point detection experiment of 300W-LP sample set.

*5.2. Reconstruction Evaluation in Constrained Scenarios.* For the evaluation of face image reconstruction in constrained scenes, this experiment uses Facescape dataset [33]. Aiming at the evaluation of the 3D model [34], the evaluation

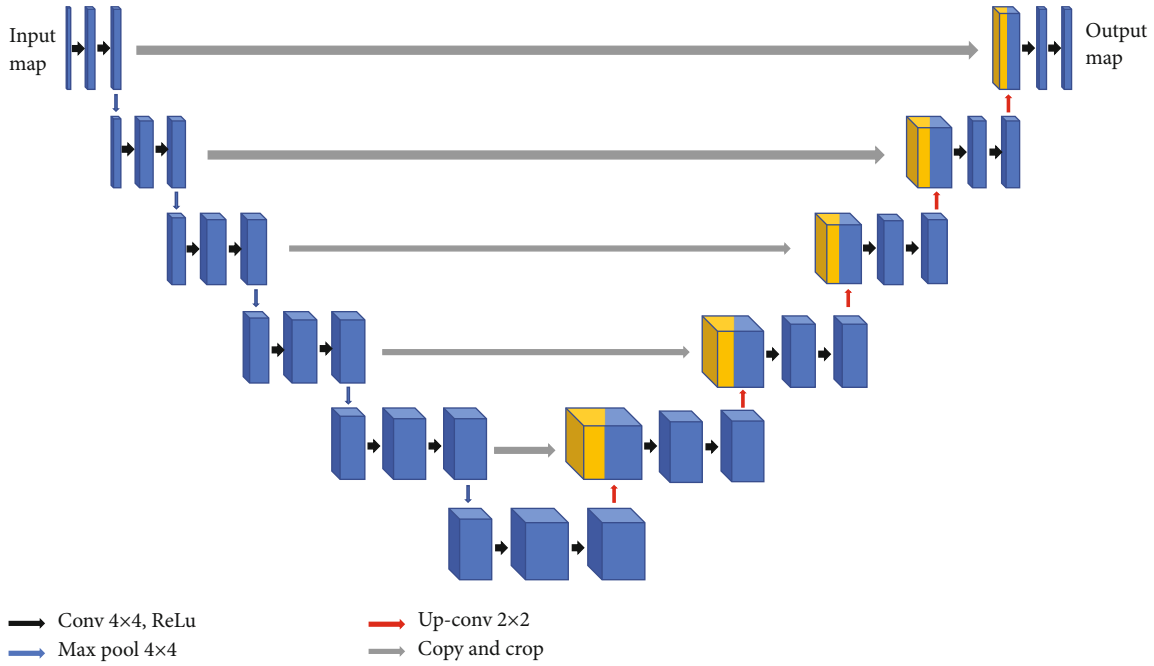


Figure 8: The structure diagram of the detailed synthesis network generator.

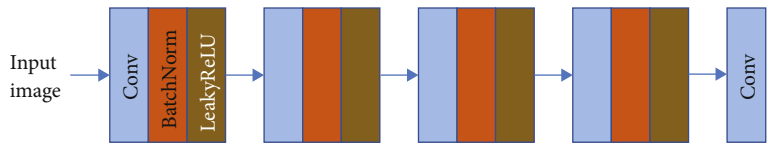


Figure 9: Network structure diagram of the discriminator.

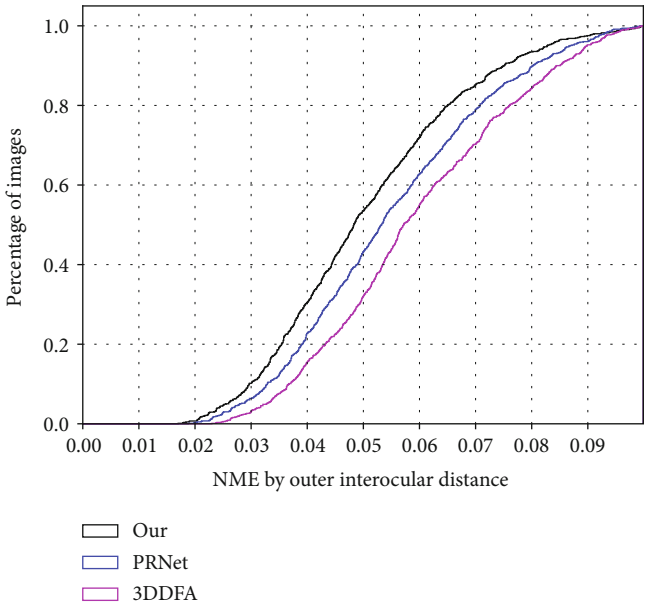


Figure 10: Comparison of cumulative error distribution (CED) curves of NME between sample landmarks and real landmarks.

Table 1: Mean RMSE 1 and mean SD of test set 1.

| Method | RMSE 1 | SD |
|---|---|---|
| Our | 3.13 | 1.87 |
| PRNet | 3.64 | 2.08 |
| 3DDFA | 4.70 | 2.96 |
| RingNet | 5.12 | 3.13 |

experiment in this paper is based on the root mean square error (RMSE) and standard deviation (SD) between the point cloud of the reconstructed model and ground truth. Among them, RMSE is used to evaluate the accuracy of the reconstructed model, and SD is used to assess the degree of dispersion of the point cloud of the reconstructed model itself. In the reconstruction evaluation, the accuracy values of neutral face evaluation, facial expression evaluation, and robustness evaluation are represented by RMSE 1, RMSE 2, and RMSE 3, respectively. The lower the RMSE and SD, the better the accuracy and dispersion of the reconstruction model.

*5.2.1. Frontal Face Model Evaluation.* In this experiment, the accuracy (RMSE 1) and the discrete value (SD) of the frontal face reconstruction model are used as the evaluation standard. In this evaluation process, 10 frontal face images of

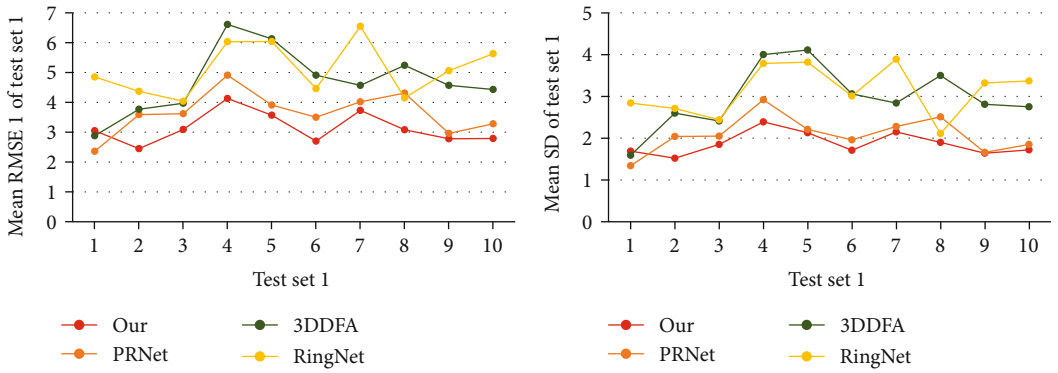


Figure 11: RMSE and SD of smooth model.

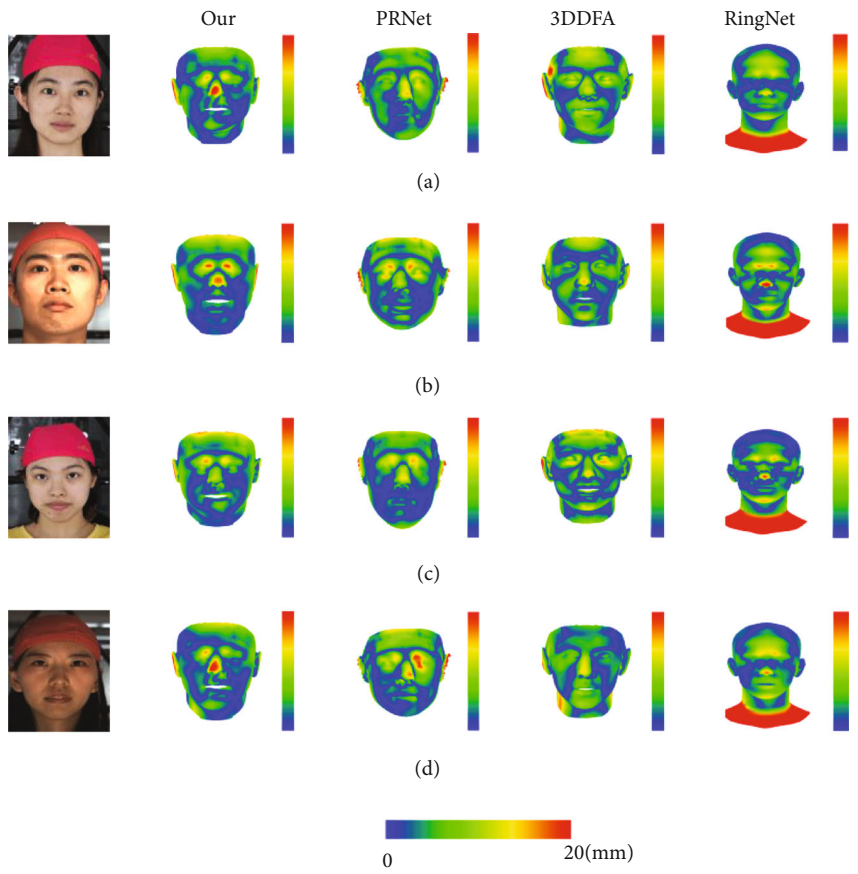


Figure 12: Error heat distribution of reconstructed model and ground truth.

the subject were randomly selected from Facescape dataset as test set 1, and the test set 1 images were reconstructed through the integrated network proposed in this paper, and 10 sets of models were obtained. In addition, this experiment compares our method with three other advanced algorithms, PRNet [9], 3DDFA [18], and RingNet [14].

According to the evaluation standard, the mean RMSE 1 and SD of the 10 groups of reconstruction models are calculated. The data of the test set 1 are shown in Table 1. The detailed data of our method and the model reconstructed by PRNet, 3DDFA, and RingNet are shown in Figure 11.

Based on the above data comparison, our method has higher accuracy and dispersion in reconstructing the frontal neutral face image compared to the other three methods. Figure 12 shows examples of the heat distribution of the sample reconstruction model error.

*5.2.2. Frontal Face Model with Expression Evaluation.* The difficulty of facial expression reconstruction is often greater than that of neutral expression face reconstruction. We show more reconstruction models of images in unconstrained environment in Figure 13.

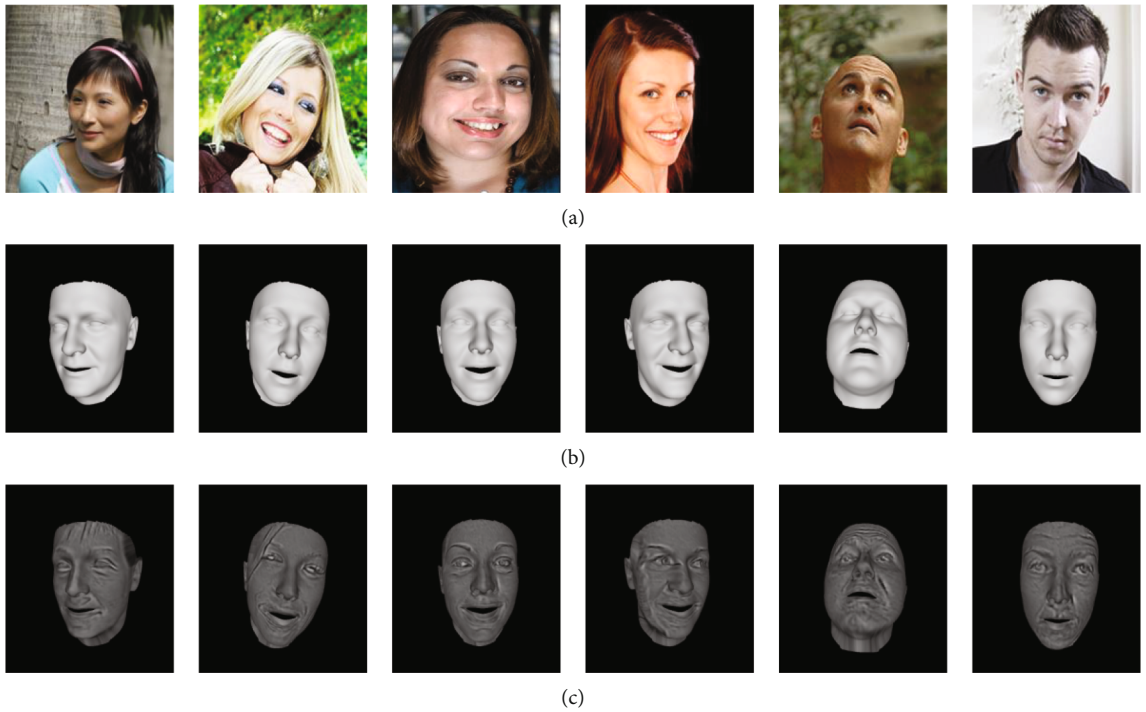


Figure 13: Reconstructed models using our method. (a) Target face images. (b) Smooth model without high frequency details. (c) Fine models with high frequency details.

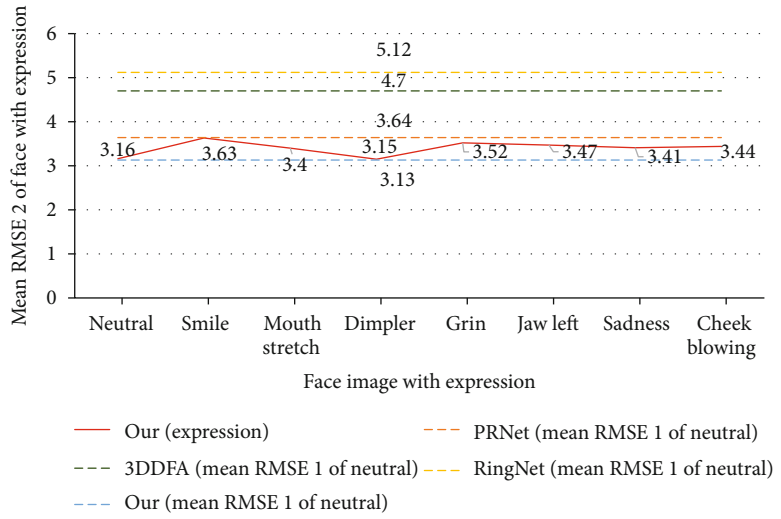


Figure 14: RMSE 2 of expression face model.

In this experiment, Facescape dataset was used to evaluate the reconstruction of facial expressions. Facescape dataset contains the depth information data of 20 facial dynamic expressions of each collected object. Eight dynamic facial expression images of the object are randomly selected from Facescape dataset for reconstruction, and the root mean square error (RMSE2) is calculated (as shown in Figure 14).

In the same method, the accuracy of facial expression reconstruction model is often slightly lower than that of neutral face reconstruction model. In Figure 14, although the RMSE 2 of face models with expression reconstructed by our method is higher than the mean RMSE 1, it is lower than the mean RMSE 1 of the face model with neutral reconstructed by other methods. The accuracy of our method for facial expression reconstruction is significantly higher than that of neutral face reconstruction model of other comparison methods, so our method also has higher advantages in facial expression fitting.

*5.2.3. Robustness Evaluation under Noise Environment.* In the field of 3D reconstruction, robustness is an important evaluation criterion for reconstruction model algorithms. It can

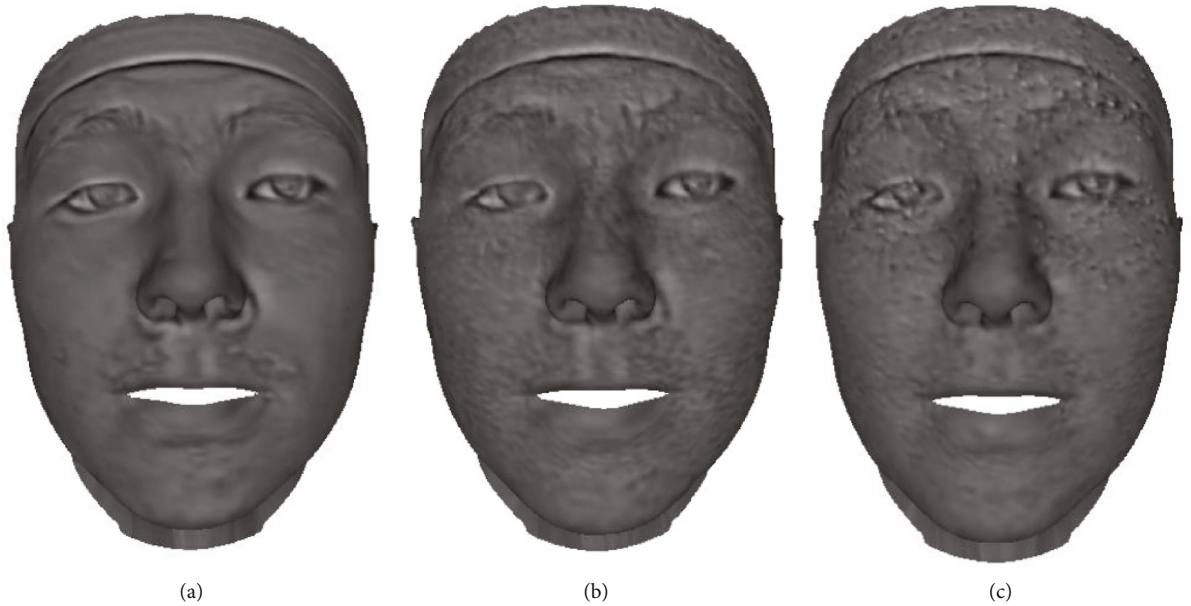


Figure 15: Robustness evaluation example model. (a) Original image reconstruction model. (b) Gaussian noise image reconstruction model. (c) Salt and pepper noise image reconstruction model.

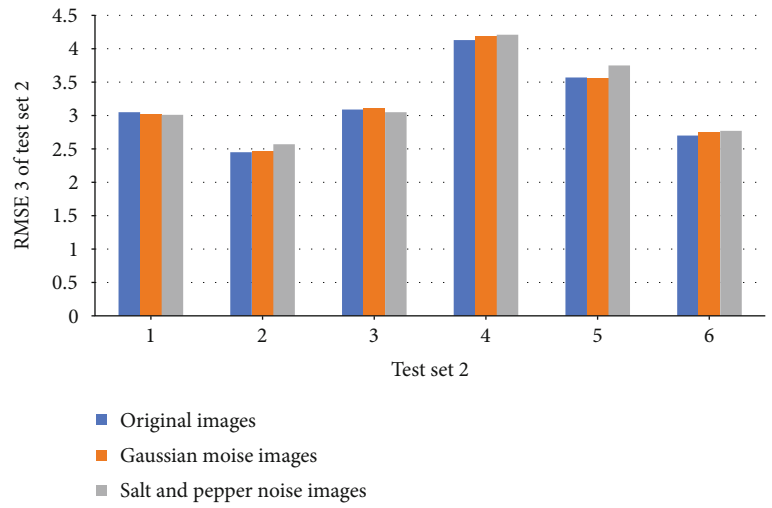


Figure 16: Robustness evaluation.

clearly indicate the degree of adaptation of the algorithm in a complex environment and whether it can reduce the influence of interference factors on model reconstruction. The robustness evaluation in this paper is mainly about face reconstruction under noisy environment. First, randomly select 6 images from the Facescape dataset, and apply Gaussian noise and salt and pepper noise to these 6 images, respectively. As can be seen in Figure 15, an example compares the difference between detail reconstruction model of the original image and detail reconstruction model of the noise image.

The image after applying noise is the test set 2. Then, the original image and the noise image of the test set 2 were reconstructed through the integrated network, compared with the ground truth, and the root mean square error (RMSE 3) was calculated (as shown in Figure 16).

According to the test set 2 of the noise evaluation experiment and the corresponding noise image, the fluctuation interval of the RMSE3 of the noise image reconstruction and the original image reconstruction is (-0.04, 0.18). In addition, there may be a large number of noise points covering the high-frequency details, which will affect the discriminating process of the discriminator of the face detail synthesis module, resulting in the increase of iterations and the slight improvement of the accuracy of the whole model.

## 6. Conclusion

We propose a reconstruction system for face model. The initial face reconstruction module uses a face alignment network and 3DMM to initially reconstruct a face with a smooth surface. The face detail synthesis network generates

a displacement map, which contains most of the details of the reconstructed object. For facial expressions, we use an emotional feature predictor to fit facial expressions. The three-dimensional sense and accuracy of the detailed face model are better than the 3DMM reconstruction model based on PCA. Through the evaluation of face alignment, accuracy, and robustness in unconstrained scenes, our method obtains ideal results. Compared with other advanced methods, our method also has more advantages.

## Data Availability

The data used to support the findings of this study are available from the corresponding author upon request.

## Conflicts of Interest

The author declares that there is no conflict of interest regarding the publication of this paper.

## Acknowledgments

This work is supported by the Shandong Provincial Natural Science Foundation (ZR2020MF119).

## References

[1] A. F. Abate, M. Nappi, D. Riccio, and G. Sabatino, "2D and 3D face recognition: a survey," *Pattern Recognition Letters*, vol. 28, no. 14, pp. 1885–1906, 2007.

[2] Y. Zhang, T. Sim, C. Lim Tan, and E. Sung, "Anatomy-based face reconstruction for animation using multi-layer deformation," *Journal of Visual Languages & Computing*, vol. 17, no. 2, pp. 126–160, 2006.

[3] E. Richardson, M. Sela, and R. Kimmel, "3D face reconstruction by learning from synthetic data," in *2016 fourth international conference on 3D vision (3DV)*, pp. 460–469, Stanford, CA, USA, 2016.

[4] V. Blanz and T. Vetter, "Face recognition based on fitting a 3d morphable model," *IEEE Transactions on Pattern Analysis and Machine Intelligence*, vol. 25, no. 9, pp. 1063–1074, 2003.

[5] Y. Chen, F. Wu, Z. Wang, Y. Song, Y. Ling, and L. Bao, "Self-Supervised Learning of Detailed 3D Face Reconstruction," *IEEE Transactions on Image Processing*, vol. 29, pp. 8696–8705, 2020.

[6] P. Paysan, R. Knothe, B. Amberg, S. Romdhani, and T. Vetter, "A 3D face model for pose and illumination invariant face recognition," in *2009 sixth IEEE international conference on advanced video and signal based surveillance*, pp. 296–301, Genova, Italy, 2009.

[7] L. Tran and X. Liu, "Nonlinear 3d face morphable model," in *Proceedings of the IEEE conference on computer vision and pattern recognition*, pp. 7346–7355, Salt Lake City, UT, USA, 2018.

[8] L. Galteri, C. Ferrari, G. Lisanti, S. Berretti, and A. del Bimbo, "Deep 3D morphable model refinement via progressive growing of conditional Generative Adversarial Networks," *Computer Vision and Image Understanding*, vol. 185, pp. 31–42, 2019.

[9] Y. Feng, F. Wu, X. Shao, Y. Wang, and X. Zhou, "Joint 3D face reconstruction and dense alignment with position map regression network," in *Computer Vision – ECCV 2018*, pp. 557–574, Springer, 2018.

[10] A. S. Jackson, A. Bulat, V. Argyriou, and G. Tzimiropoulos, "Large pose 3D face reconstruction from a single image via direct volumetric CNN regression," in *2017 IEEE International Conference on Computer Vision (ICCV)*, pp. 1031–1039, Venice, Italy, 2017.

[11] A. T. Tran, T. Hassner, I. Masi, E. Paz, Y. Nirkin, and G. Medioni, "Extreme 3D face reconstruction: seeing through occlusions," in *2018 IEEE/CVF Conference on Computer Vision and Pattern Recognition*, pp. 3935–3944, Salt Lake City, UT, USA, 2018.

[12] A. Ranjan, T. Bolkart, S. Sanyal, and M. J. Black, "Generating 3D faces using convolutional mesh autoencoders," in *Computer Vision – ECCV 2018*, pp. 704–720, Springer, 2018.

[13] T. Li, T. Bolkart, M. J. Black, H. Li, and J. Romero, "Learning a model of facial shape and expression from 4D scans," *ACM Transactions on Graphics*, vol. 36, no. 6, pp. 1–17, 2017.

[14] S. Sanyal, T. Bolkart, H. Feng, and M. J. Black, "Learning to regress 3D face shape and expression from an image without 3D supervision," in *2019 IEEE/CVF Conference on Computer Vision and Pattern Recognition (CVPR)*, pp. 7763–7772, Long Beach, CA, USA, 2019.

[15] Y. Deng, J. Yang, S. Xu, D. Chen, Y. Jia, and X. Tong, "Accurate 3D face reconstruction with weakly-supervised learning: from single image to image set," in *2019 IEEE/CVF Conference on Computer Vision and Pattern Recognition Workshops (CVPRW)*, pp. 285–295, Long Beach, CA, USA, 2019.

[16] Y. Guo, J. Zhang, J. Cai, B. Jiang, and J. Zheng, "CNN-based real-time dense face reconstruction with inverse-rendered photo-realistic face images," *IEEE Transactions on Pattern Analysis and Machine Intelligence*, vol. 41, no. 6, pp. 1294–1307, 2019.

[17] V. Kazemi and J. Sullivan, "One millisecond face alignment with an ensemble of regression trees," in *2014 IEEE Conference on Computer Vision and Pattern Recognition*, pp. 1867–1874, Columbus, OH, USA, 2014.

[18] X. Zhu, Z. Lei, X. Liu, H. Shi, and S. Z. Li, "Face alignment across large poses: a 3D solution," in *2016 IEEE Conference on Computer Vision and Pattern Recognition (CVPR)*, pp. 146–155, Las Vegas, NV, USA, 2016.

[19] T. Gerig, A. Morel-Forster, C. Blumer et al., "Morphable face models-an open framework," in *2018 13th IEEE International Conference on Automatic Face & Gesture Recognition (FG 2018)*, pp. 75–82, Xi'an, China, 2018.

[20] A. M. Bruckstein, R. J. Holt, T. S. Huang, and A. N. Netravali, "Optimum fiducials under weak perspective projection," *International Journal of Computer Vision*, vol. 35, no. 3, pp. 223–244, 1999.

[21] F. Mokhayeri, E. Granger, and G. A. Bilodeau, "Domain-specific face synthesis for video face recognition from a single sample per person," *IEEE Transactions on Information Forensics and Security*, vol. 14, no. 3, pp. 757–772, 2019.

[22] A. Chen, Z. Chen, G. Zhang, K. Mitchell, and J. Yu, "Photo-realistic facial details synthesis from single image," in *2019 IEEE/CVF International Conference on Computer Vision (ICCV)*, pp. 9429–9439, Seoul, Korea, 2019.

[23] Z. S. Hakura and E. M. Kilgariff, "Calculation of plane equations after determination of Z-buffer visibility," 2014, US Patent 8,692,829.

[24] X. Cao, Y. Wei, F. Wen, and J. Sun, "Face alignment by explicit shape regression," *International Journal of Computer Vision*, vol. 107, no. 2, pp. 177–190, 2014.

[25] K. He, X. Zhang, S. Ren, and J. Sun, "Deep residual learning for image recognition," in *2016 IEEE Conference on Computer Vision and Pattern Recognition (CVPR)*, pp. 770–778, Las Vegas, NV, USA, 2016.

[26] K. He, X. Zhang, S. Ren, and J. Sun, "Identity mappings in deep residual networks," in *Computer Vision – ECCV 2016*, pp. 630–645, Springer, 2016.

[27] D. S. Rice and M. F. Deering, "Displacement mapping by using two passes through the same rasterizer," 2006, US Patent 7,148,890.

[28] A. Mollahosseini, B. Hasani, and M. H. Mahoor, "Affectnet: a database for facial expression, valence, and arousal computing in the wild," *IEEE Transactions on Affective Computing*, vol. 10, no. 1, pp. 18–31, 2017.

[29] I. J. Goodfellow, J. Pouget-Abadie, M. Mirza et al., "Generative adversarial networks," 2014, https://arxiv.org/abs/1406.2661.

[30] H. Kuang, Y. Ding, X. Ma, and X. Liu, "3D face reconstruction with texture details from a single image based on GAN," in *2019 11th International Conference on Measuring Technology and Mechatronics Automation (ICMTMA)*, pp. 385–388, Qiqihar, China, 2019.

[31] O. Ronneberger, P. Fischer, and T. Brox, "U-net: convolutional networks for biomedical image segmentation," in *International Conference on Medical image computing and computer-assisted intervention*, pp. 234–241, Cham, 2015.

[32] U. Demir and G. Unal, "Patch-based image inpainting with generative adversarial networks," 2018, https://arxiv.org/abs/1803.07422.

[33] H. Yang, H. Zhu, Y. Wang et al., "FaceScape: a large-scale high quality 3D face dataset and detailed riggable 3D face prediction," in *2020 IEEE/CVF Conference on Computer Vision and Pattern Recognition (CVPR)*, pp. 601–610, Seattle, WA, USA, 2020.

[34] L. Jiang, J. Zhang, B. Deng, H. Li, and L. Liu, "3D face reconstruction with geometry details from a single image," *IEEE Transactions on Image Processing*, vol. 27, no. 10, pp. 4756–4770, 2018.

Hindawi
Journal of Sensors
Volume 2021, Article ID 9926442, 13 pages
https://doi.org/10.1155/2021/9926442

*Research Article*

# Analyzing the Impact of Climate Factors on GNSS-Derived Displacements by Combining the Extended Helmert Transformation and XGboost Machine Learning Algorithm

**Hanlin Liu**,[1,2] **Linqiang Yang**,[3] **and Linchao Li**[1,2]

[1]*College of Civil and Transportation Engineering, Shenzhen University, Shenzhen 518061, China*
[2]*Institute of Urban Smart Transportation & Safety Maintenance, Shenzhen University, Shenzhen 518061, China*
[3]*Department of Civil and Environmental Engineering, University of Hawaii at Manoa, Honolulu, HI 96822, USA*

Correspondence should be addressed to Linchao Li; lilinchao@szu.edu.cn

Received 8 March 2021; Accepted 7 May 2021; Published 28 May 2021

Academic Editor: Aijun Yin



A variety of climate factors influence the precision of the long-term Global Navigation Satellite System (GNSS) monitoring data. To precisely analyze the effect of different climate factors on long-term GNSS monitoring records, this study combines the extended seven-parameter Helmert transformation and a machine learning algorithm named Extreme Gradient boosting (XGboost) to establish a hybrid model. We established a local-scale reference frame called stable Puerto Rico and Virgin Islands reference frame of 2019 (PRVI19) using ten continuously operating long-term GNSS sites located in the rigid portion of the Puerto Rico and Virgin Islands (PRVI) microplate. The stability of PRVI19 is approximately 0.4 mm/year and 0.5 mm/year in the horizontal and vertical directions, respectively. The stable reference frame PRVI19 can avoid the risk of bias due to long-term plate motions when studying localized ground deformation. Furthermore, we applied the XGBoost algorithm to the postprocessed long-term GNSS records and daily climate data to train the model. We quantitatively evaluated the importance of various daily climate factors on the GNSS time series. The results show that wind is the most influential factor with a unit-less index of 0.013. Notably, we used the model with climate and GNSS records to predict the GNSS-derived displacements. The results show that the predicted displacements have a slightly lower root mean square error compared to the fitted results using spline method (prediction: 0.22 versus fitted: 0.31). It indicates that the proposed model considering the climate records has the appropriate predict results for long-term GNSS monitoring.

## 1. Introduction

Within the various remote sensing technologies, Global Navigation Satellite Systems (GNSS) plays an important role in providing fundamental infrastructure and has been successfully implemented in deformation monitoring. The global GNSS, such as the United States' Global Positioning System (GPS), Russia's Global Navigation Satellite System (GLONASS), the European Union's Galileo, and China's Beidou Navigation Satellite System (BDS), serve as highly efficient monitoring tools for precise geodetic surveying. Different unions or countries have installed numerous Continuously Operating Reference Stations (CORS) for various monitoring purposes, including the Plate Boundary Observatory (PBO) maintained by National Science Foundation (NSF) EarthScope, the CORS GPS network maintained by the U.S. National Geodetic Survey, and the GPS Earth Observation Network (GEONET) of Japan. More than 506 worldwide permanent GNSS stations are managed by the International GNSS Service (IGS) group as of December 08, 2019. The original RINEX (Receiver Independent Exchange Format) files for the GNSS stations in different CORS networks are free to download through University NAVSTAR Consortium (UNAVCO) or National Geodetic Survey (NGS) data archiving facilities [1, 2]. The GPS, originally NAVSTAR GPS, is a widely used satellite positioning system, and it especially refers to the GNSS owned and operated by the United States. In the United States, the GPS signal has been widely used in

the monitoring service since 1989 [3]. Although this study only used GPS signals, GNSS is currently used as an umbrella term for all the aforementioned global satellite positioning systems. For this reason, this study uses the term GNSS.

Understanding the climate variations of GNSS time series are important for monitoring applications. In practice, during the period of half, one, or two years, the long-term monitoring time series have cyclical fluctuation and rebound characteristics triggered by climate influence, which makes the users who do not major in geodesy confuse about the precision of GNSS monitoring. The climate factors, mainly including the rainfall, temperature difference, wind speed, visibility, dew, and humidity, have always been a question among the long-term monitoring GNSS operators and data users. Xu et al. [4] proved that climate change led to the periodical variety of thermal expansion of bedrock (TEB). Dong et al. [5] established the hybrid model to remove the seasonal variations from long-term time series. Yan et al. [6] combined the thermal expansion model with the mass loading model to study the observed annual GNSS height changes. Munekane [7] proposed that the large temperature difference induced the maximum vertical displacements of three millimeters within 24 hours and established a model to move it. The climate variations are recognized as impact factors of the target deformation. Moreover, since the climate includes a variety of parts, the effects due to local climate variations on GNSS observations need to be carefully further studied. Thus, it is necessary to quantitatively analyze the weights of impacts caused by different climate factors on the long-term GNSS monitoring time series.

To achieve the quantitative analysis results of the impact on the GNSS time series caused by different daily climate factors, we need high-precision GNSS records. The accuracy and precision of GNSS observations are impacted by the types of GNSS equipment used and the processing method applied. In general, there are two widely used GNSS data postprocessing approaches: relative positioning and absolute positioning. The relative positioning approach uses the carrier-phase double-difference (DD) method to fix differenced phase ambiguities to integer values between stations and between satellites [8]. The DD method uses simultaneous GNSS records from at least two GNSS stations, and at least one of the GNSS stations should be installed in a stable foundation or known position with respect to a specific reference frame. The absolute positioning approach only needs a single GNSS station to determine the position without using any synchronous data from other stations. This method used undifferenced dual-frequency pseudo-range and carrier-phase observations in addition to precise satellite orbits and clock information to determine the position of a stand-alone GNSS station [9].

Precise Point Positioning (PPP) is a typical GNSS postprocessing absolute positioning approach, which uses a single-receiver phase-ambiguity-fixed resolution to calculate daily original raw data. The precision of the PPP solutions has dramatically increased during the last decade, which primarily attributes to highly precise satellite orbits and clock data provided by the International GNSS Service (IGS) and new algorithms used to resolve phase ambiguity within a single receiver [10]. Moreover, the PPP algorithm has operational simplicity and can provide consistent accuracy [11, 12]. Considering the risk of lacking high-quality reference GNSS station when using the relative DD method, it is convenient to use the PPP method to process the GNSS data that monitor the long-term structural deformation or surface land movements. In this study, the software package GIPSY/OASIS (V6.4) employing the PPP processing strategy was applied [13]. The estimation of wide lane and phase bias was maintained by the Jet Propulsion Laboratory (JPL). When applying the GIPSY/OASIS software to solve daily positions, they are processed within the $X$, $Y$, and $Z$ geocentric Cartesian coordinate systems. The widely accepted global reference named the International Terrestrial Reference Frame (ITRF) is derived from the method of minimizing the overall horizontal movements of selected global permanent stations [14]. Using the GNSS to study the global tectonic movement, the most common global reference frame based on GNSS sites is required. Currently, the latest earth-centered, earth-fixed global reference frame International GNSS service of 2014 (IGS14) is established and aligned to ITRF2014 datum, which was updated from ITRF2008 in January 2017 [15]. However, the reference frame selection is motivated by the purpose of the study. In a continental-scale study area, such as North American, the NA12 was defined by 299 GPS stations and designed to corotate with the stable interior of the North American tectonic plate [16]. Also, another North American Plate fixed reference frame (NAD83 reference frame) was established resulting from requirements of the coordinates for sites located in the Conterminous United States (CONUS), Alaska, and US territories in the Caribbean. However, the high-precision GNSS monitoring time series inevitably include background tectonic motion within the subcentimeter level in the continental scale reference frame [17]. The millimeter-level internal tectonic movements could be easily obscured and biased within an inappropriate reference frame [18]. For this reason, there is a need to establish a stable regional or local reference frame for studies focusing on regional or local scales.

The scale, the orientation, the origin, and the change of these parameters over time are the main physical and mathematical properties of a reference frame. In geodetic applications, a stable local reference frame is primarily transformed from the latest and well-established global reference frame using the Helmert transformation. A group of GNSS reference stations (common points) are used to tie the target regional or local reference frames to a global reference frame (e.g., IGS14). Pearson and Snay [19] used a 14-parameter transformation method to transform coordinates from the global reference frame IGS08 to the regional reference frame NAD83, which is maintained by NGS. Theoretically, the coordinates of a point referred to the IGS14 global reference frame vary when they are transformed to a regional or local reference frame. Nevertheless, deformation monitoring mainly focuses on the deformation rates/displacements of the target study area rather than the coordinates themselves in both reference frames. In general, relative high precision displacements or deformation velocities are needed in different area monitoring applications.

In practice, after the highly precise GNSS records are processed, it is still a challenge to quantitatively analyze the weights of impact from different climate factors on the GNSS time series. However, with computing science development, the machine learning approach achieves a dramatic developing rate and provides a new tool to explore new analysis methods in geodesy and geosciences. The approach can quantitatively analyze the hypothesis and assist to capture high-dimensional data sets [20, 21]. Furthermore, machine learning methods have been widely applied in geosciences. Rouet et al. [22] evaluate the fault movements in the Cascadia subduction zone. Phrampus et al. [23] predict the probability of encountering global SEAFLEA. Anderson and Lucas [24] proposed the climate ensemble method to predict weather and establish various climate models. Ren et al. [25] used the machine learning algorithm to estimate the fault friction with high precision. The machine learning algorithm has the potential to help researchers make further explanations and explore the theories behind the questions in geosciences. Therefore, we applied the ensemble learning method to analyze the weights of impact from various daily climate factors on the GNSS monitoring time series. In this study, we used an appropriate supervised machine learning (SML) algorithm, Extreme Gradient Boosting (XGBoost), to determine the relationship between various daily climate factors and highly precise GNSS data.

In this paper, we proposed a hybrid method to evaluate the impact of daily climate factors on the GNSS time series, using the extended Helmert transformation method and XGBoost algorithm. The model is trained by high-precision GNSS records and various long-term climate records. The contributions of this paper are shown as follows:

(1) To remove the background tectonic movements when monitoring local ground deformation, we proposed the extended Helmert transformation to establish the highly stable PRVI19 local reference frame based on ten well-distributed continuously operating GNSS stations with at least five years of data

(2) By combining the GNSS records with millimeter accuracy and the local climate data with a span of at least five years, we applied the XGboost machine learning algorithm to derive the quantitative results of the weights of impact from different daily climate factors on the GNSS time series

(3) Based on the model, we predicted the GNSS records and validate them with the real raw GNSS data. The results show that the high accuracy of the prediction and it is expected that this study can provide a new prospect to explore the potential deformation monitoring problem

## 2. Data and Methods

*2.1. Coordinate Transformation Using the Extended Helmert Transformation Method.* The Helmert transformation, also called a 7-parameter transformation, is used to conduct distortion-free reference frame transformations within a three-dimensional (3D) space in the geodesy area. The 7-parameter approach employs three parameters from translations, three parameters from rotations, and one parameter from the scale at a selected epoch and the rates of these seven parameters over time. For daily GNSS positional coordinate transformation from the PPP solutions, the geocentric coordinates of a site with respect to the local reference frame can be approximated by the following formula:

$$X(t)_{\text{local}} = T_X(t) + [1 + s(t)]\bullet X(t)_{\text{IGS14}} + R_Z(t)\bullet Y(t)_{\text{IGS14}} - R_Y(t)\bullet Z(t)_{\text{IGS14}}, \tag{1}$$

$$Y(t)_{\text{local}} = T_Y(t) + R_Z(t)\bullet X(t)_{\text{IGS14}} + [1 + s(t)]\bullet Y(t)_{\text{IGS14}} + R_X(t)\bullet Z(t)_{\text{IGS14}}, \tag{2}$$

$$Z(t)_{\text{local}} = T_Z(t) + R_Y(t)\bullet X(t)_{\text{IGS14}} - R_X(t)\bullet Y(t)_{\text{IGS14}} + [1 + s(t)]\bullet Z(t)_{\text{IGS14}}, \tag{3}$$

where $R_X(t)$, $R_Y(t)$, and $R_Z(t)$ are counterclockwise rotations along $X$ axis, $Y$ axis, and $Z$ axis of the geocentric coordinate system; $T_X(t)$, $T_Y(t)$, and $T_Z(t)$ are translations about these three axes; and $s(t)$ is a differential scale change between IGS14 and local reference frame.

Theoretically, the seven parameters for each epoch/day are different. Therefore, to obtain the positional time series in the local reference frame, the seven parameters at each epoch have to be provided. Currently, there are two strategies that can be employed to perform the transformation, daily seven-parameter transformation, and 14-parameter transformation [19]. Continuous observations have made it possible to calculate the seven transformation parameters on a daily basis and transform the daily positional time series from one reference frame to another. However, calculating daily transformation parameters is too complex for most end-users, since users have to include a large number of reference stations for calculating transformation parameters at each epoch. Besides, it is difficult to ensure the data quality and availability for all the reference stations at each day. Thus, the GNSS time series of these seven transformation parameters can be simulated by the linear method with equations:

$$\alpha_t = \begin{bmatrix} T_X(t) \\ T_Y(t) \\ T_Z(t) \end{bmatrix}, \beta_t = \begin{bmatrix} R_X(t) \\ R_Y(t) \\ R_Z(t) \end{bmatrix}, \alpha' = \begin{bmatrix} T'_X \\ T'_Y \\ T'_Z \end{bmatrix}, \beta' = \begin{bmatrix} R'_X \\ R'_Y \\ R'_Z \end{bmatrix}, \tag{4}$$

$$\alpha_t = \alpha_{t_0} + \alpha'\bullet(t - t_0), \tag{5}$$

$$\beta_t = \beta_{t_0} + \beta'\bullet(t - t_0), \tag{6}$$

$$s(t) = s(t_0) + s'\bullet(t - t_0). \tag{7}$$

Here, $t_0$ denotes a specific epoch, which is set as specific epoch. $T_X(t_0)$, $T_Y(t_0)$, $T_Z(t_0)$, $R_X(t_0)$, $R_Y(t_0)$, $R_Z(t_0)$, and $s$

$(t_0)$ are the seven Helmert transformation parameters at specific epoch $t_0$. $T'_X$, $T'_Y$, $T'_Z$, $R'_X$, $R'_Y$, $R'_Z$, and $s'$ are the first derivatives (rates) of these seven parameters, which are assumed to be constant; the units of the translational components ($T_X(t)$, $T_Y(t)$, $T_Z(t)$) are meters; the units of the three rotational components ($R_X(t)$, $R_Y(t)$, $R_Z(t)$) are radians; the units of the rates of translational components ($T'_X$, $T'_Y$, $T'_Z$) are meter/year; the units of the rates of the rotational components ($R'_X$, $R'_Y$, $R'_Z$) are radian/year, and $s(t)$ is a unitless scale. The local reference frame is tied to the same origin and scale of the original global reference frame, which is the IGS14 global reference frame in this study. The above formulas also require the use of a scale factor $s(t)$ to minimize the distortion of point-to-point distances between the two reference frames. In general, the scale factor $s(t)$ can be set as zero in frame transformations between a global reference frame and a local reference frame [26]. The common points are used to solve the inverse problem by the least square method.

Then, the coordinates of the target GNSS stations referred to the local reference frame can be obtained through:

$$X(t)_{\text{local}} = X(t)_{\text{IGS14}} + T'_X \bullet (\Delta t) + R'_Z \bullet (\Delta t) \bullet Y(t)_{\text{IGS14}} - R'_Y \bullet (\Delta t) \bullet Z(t)_{\text{IGS14}}, \tag{8}$$

$$Y(t)_{\text{local}} = Y(t)_{\text{IGS14}} + T'_Y \bullet (\Delta t) - R'_Z \bullet (\Delta t) \bullet X(t)_{\text{IGS14}} + R'_X \bullet (\Delta t) \bullet Z(t)_{\text{IGS14}}, \tag{9}$$

$$Z(t)_{\text{local}} = Z(t)_{\text{IGS14}} + T'_Z \bullet (\Delta t) + R'_Y \bullet (\Delta t) \bullet X(t)_{\text{IGS14}} - R'_X \bullet (\Delta t) \bullet Y(t)_{\text{IGS14}}, \tag{10}$$

$$\Delta t = (t - t_0). \tag{11}$$

Also, since a linear model is assumed, the changing rates can be easily calculated with two sets of transformation parameters at two different epochs. In this study, the epochs are set as $t_0$ (i.e., 2015) and $t_1$ (i.e., 2018). So, the coordinates in both frames at epoch $t_0$ are the same, and the seven parameters are all zeros. The method aligns the two frames at the epoch $t_0$. The coordinates at epoch $t_0$ are calculated with the following equation:

$$\begin{pmatrix} X(t_0)_{\text{IGS14}} \\ Y(t_0)_{\text{IGS14}} \\ Z(t_0)_{\text{IGS14}} \end{pmatrix} = \begin{pmatrix} X(t_0)_{\text{local}} \\ Y(t_0)_{\text{local}} \\ Z(t_0)_{\text{local}} \end{pmatrix}. \tag{12}$$

In order to calculate the transformation parameters at another epoch $t_1$, the coordinates at epoch $t_1$ in IGS14 and local reference frame can be derived by using the following equations:

$$\begin{pmatrix} X(t_1)_{\text{local}} \\ Y(t_1)_{\text{local}} \\ Z(t_1)_{\text{local}} \end{pmatrix} \approx \begin{pmatrix} X(t_0)_{\text{local}} \\ Y(t_0)_{\text{local}} \\ Z(t_0)_{\text{local}} \end{pmatrix}. \tag{13}$$

Here, the velocity in local reference frame is regarded as zero since local reference frame is designed to have a velocity of zero relative to the rigid part of the region. With the coordinates at epoch $t_0$ in both IGS14 and local reference frame, equations (1), (2), and (3) can be solved for the seven parameters at epoch $t_0$. By knowing the six parameters for epoch $t_0$ and $t_1$, the parameter rates can be obtained by a simple differential method:

$$T'_X = \frac{(T_X(t_1) - T_X(t_0))}{\Delta t}, \tag{14}$$

$$R'_X = \frac{(R_X(t_1) - R_X(t_0))}{\Delta t}. \tag{15}$$

Then, the coordinates of a GNSS site at any epoch can be transformed from IGS14 to the local reference frame with $T'_X$, $T'_Y$, $T'_Z$, $R'_X$, $R'_Y$, and $R'_Z$ parameters.

*2.2. Extreme Gradient Boosting (XGboost) Algorithm.* In this study, we applied the Extreme Gradient Boosting (XGboost) algorithm to predict ground displacements and to understand which climate factors have more impact on the GNSS monitoring time series. XGBoost was proposed by Chen et al. [27], which can combine many regression trees into one strong ensemble learner. Because of the ensemble, XGBoost can sufficiently capture complex interaction of variables in monitoring time series and then fit the nonlinear dynamic changes of displacements. This is one of the motivations for us to select XGBoost in this paper. Another reason is that the strong explanation power of XGBoost can help us understand the relationship between different daily climate variables and predict the high-precision GNSS displacements.

In XGBoost, $K$ additive regression trees are together to predict displacements. That is:

$$\hat{y}_i = \sum_{k=1}^{K} g_k(x_i), g_k \in \mathcal{F}, \tag{16}$$

where $\mathcal{F} = \{g(x) = w_{q(x)}\} (q : \mathcal{R}^m \to T, w \in \mathcal{R}^T)$ is the space of used regression trees, $x_i$ is a data set containing historical displacements, each $g_k$ represents an independent regression tree structure $q$ and leaf weights $w$, and $T$ represents the number of leaves of the regression tree.

The optimization function of XGBoost can be written as:

$$\mathcal{L} = \sum_i l(\hat{y}_i, y_i) + \sum_k \Omega(g_k), \tag{17}$$

$$\Omega(g) = \beta T + \frac{1}{2}\lambda \|w\|^2, \tag{18}$$

where $\beta$ and $\lambda$ are coefficients, $l$ is a differentiable convex loss function which represents the differences between measured displacements and predicted displacements, and $\Omega(g)$ is the penalty term of the objective function which helps avoid the overfitting problem.

However, because of the complex architecture, it is difficult to train the ensemble learner once. An additive strategy

has been widely applied which means trees are trained one by one. The trees that have already been trained will be fixed, and then, a new tree is added at one step. Suppose that the predicted displacement at step $t$ is $\widehat{y}_i^{(t)}$, then the optimization function at this step can be written as:

$$\mathscr{L}_t = \sum_i l\left(y_i, \widehat{y}_i^{(t-1)} + g_t(x_i)\right) + \sum_k \Omega(g_t) + C, \tag{19}$$

where $C$ is a constant. To approximate the optimization function using a second-order Taylor expansion, it can be rewritten as:

$$\mathscr{L}_t = \sum_{i=1}^{n}\left[a_i g_t(x_i) + \frac{1}{2} b_i g_t^2(x_i)\right] + \Omega(g_t), \tag{20}$$

where

$$a_i = \frac{\partial l\left(y_i, \widehat{y}_i^{(t-1)}\right)}{\partial \widehat{y}_i^{(t-1)}}, \tag{21}$$

$$b_i = \frac{\partial^2 l\left(y_{ii}, \widehat{y}_i^{(t-1)}\right)}{\partial\left(y\wedge_i^{(t-1)}\right)^2}. \tag{22}$$

With equations (19) and (20), the optimization function can be revised as:

$$\mathscr{L} = \sum_{j=1}^{T}\left[\left(\sum_{i\in I_j} a_i\right) w_j + \frac{1}{2}\left(\sum_{i\in I_j} b_i + \lambda\right) w_j^2\right] + \beta T, \tag{23}$$

where $I_j = \{i \mid q(x_i) = j\}$. Given a tree structure $q(x)$, the weight of the $j$th node and extreme value of $\mathscr{L}(q)$ can be obtained as:

$$w_j = -\frac{\sum_{i\in I_j} a_i}{\sum_{i\in I_j} b_i + \lambda}, \tag{24}$$

$$\mathscr{L}(q) = -\frac{1}{2}\sum_{j=1}^{T}\frac{\left(\sum_{i\in I_j} a_i\right)^2}{\sum_{i\in I_j} b_i + \lambda} + \beta T. \tag{25}$$

As studied by Breiman and Friedman [28], for a single regression tree (RT), the following equation can be used to measure the relative importance of independent variables in the tree:

$$I_d^2(\mathrm{RT}) = \sum_{t=1}^{T-1} \alpha_t^2 I(v(j) = d), \tag{26}$$

where $t$ is a nonterminal node and $T$ is the terminal node of tree RT, $x_d$ is the splitting variable of node $t$, and $\alpha_t^2$ is the improvement of square error of the prediction if $x_d$ is used as splitting variable. For an ensemble learner, which is a collection of $M$ regression trees $\{\mathrm{RT}_m\}_1^M$, the relative importance of variable $x$ can be obtained by its average over all additive trees:

$$I_d^2 = \frac{1}{M}\sum_{m=1}^{M} I_d^2(\mathrm{RT}_m). \tag{27}$$

The XGBoost is implemented using the "xgboost" package in the R software [29].

*2.3. Data and Selection.* In geodesy, a terrestrial reference frame is realized by selecting a set of reference stations and defining their positions and velocities. The selection of the reference stations is critical for establishing a stable reference frame. Here, it is very hard to set any mathematical or technical standard for selecting appropriate GNSS reference stations. In general, with some previously proposed guidelines, the reference stations are selected based on overall geographic distribution and long-term (e.g., >5 years) continuous records [30, 31]. Also, it requires no considerable subsidence or uplift with vertical velocity magnitude less than 0.5 mm/year referred to the global reference frame IGS14. A reference station that is not locally stable will degrade the overall stability or precision of the reference frame. The selection is mostly based on the availability of long-term CORS in the study area. In addition, if the selected GNSS sites have detailed station logs, which it may help explain the unexpected steps. The step means that the GNSS time series have sudden ascending or descending jump induced by the earthquake, volcano eruption, or/and GNSS equipment change. In this paper, we selected Puerto Rico and the Northern Virgin Islands (PRVI) to be the target area. In the tectonic setting, the motivation results from the results that researchers proposed the exist of rigid block of Puerto Rico and the Northern Virgin Islands (PRVI) between the Caribbean Plate and the North American Plate [32, 33]. The area is recognized as a tectonic stable microplate without notably tectonic movements in the Caribbean area and can minimize the influence from tectonic movements. The PRVI region is recognized as an appropriate area to apply the method.

Also, the PRVI region has established an appropriate GNSS infrastructure and has a long-term land monitoring history. Since 1986, GNSS stations were installed by researchers for studying Caribbean plate tectonic movements [34]. In the PRVI region, as of 2020, 28 GNSS stations are recording the displacement observations with 15 seconds positioning. GNSS station coverage within this region is exceptionally dense. The PRVI region owns the densest GNSS stations in the United States and has been well monitored by numerous permanent GNSS stations [30]. For example, the coverage along the coast of Puerto Rico is approximately 20.0 stations per kilometer. Eight GNSS stations within the PRVI region were installed by the Puerto Rico Seismic Network (PRSN) at the University of Puerto Rico at Mayaguez (UPRM). The installation was primarily funded by a National Science Foundation (NSF) Major Research Instrumentation (MRI) project (EAR-0722540). The daily GNSS records with a sample rate of 15 seconds are archived at UNAVCO public data archiving facility.

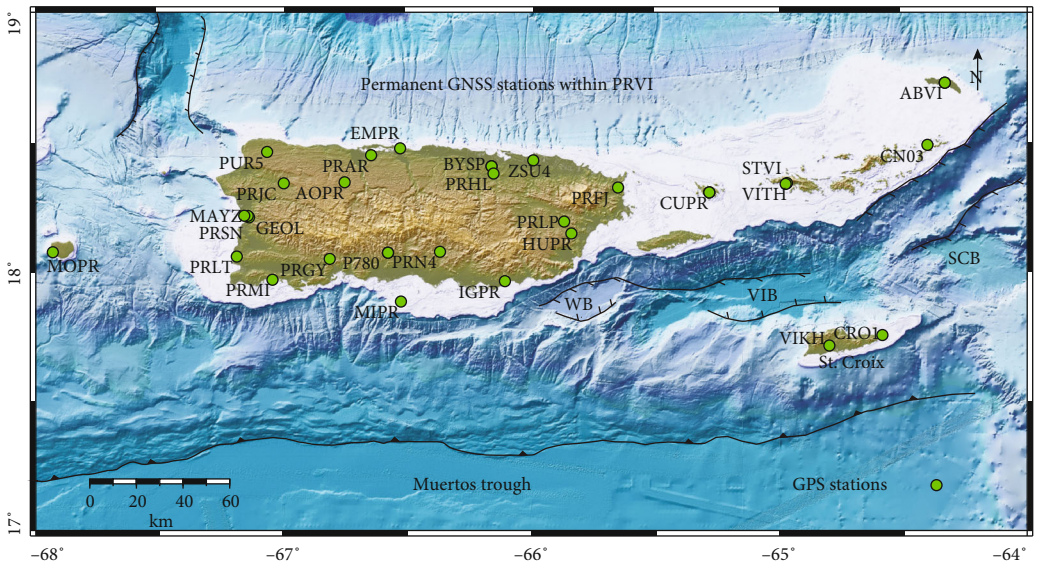


Figure 1: Map showing the locations of current GNSS stations in the Puerto Rico and Virgin Islands region. VI represents the Virgin Islands; WB represents the Whiting basin; VIB represents the Virgin Islands basin; SCB represents the St. Croix basin.

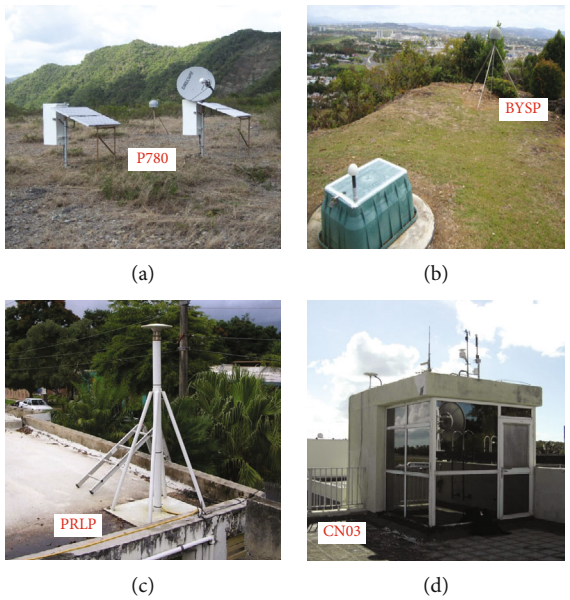


Figure 2: Figure showing the site views of four typical continuously operating permanent GNSS stations in the PRVI region. (a) A site view at Cerrillos_PR2008 GNSS station (ID: P780) installed in Ponce, PR. The antenna is mounted to a short-drilled braced monument (SDBM) designed by UNVCO. (b) A site view at BayamonSciPR2008 GNSS station (ID: BYSP) and a nearby strong motion accelerometer installed in the Bayamón Science Park, Bayamón, PR. (c) A typical building based GNSS station (ID: PRLP) installed by the HLCM Group Inc. in Las Piedras, PR. (d) A site view at DVirgGordaBVI2013 GNSS station (ID: CN03) installed at the top of a mountain in North Sound, Virgin Gorda.

The HLCM Group Inc. also installed eight GNSS stations in the PRVI region for land surveying. The HLCM Group Inc. is a private surveying company, and it archives the GNSS data at the NGS data archiving facility. Other public agencies, such as the U.S. Coast Guard, Federal Aviation Administration (FAA), and Jet Propulsion Laboratory (JPL), also operate GNSS stations in the PRVI region. Therefore, the well-established GNSS network and the complete equipment maintenance record offer a strong foundation to apply the experiment (Figure 1). Moreover, since the GNSS signals are likely to be blocked by the circumstance, the GNSS stations need to be installed in the open area. The open area, such as the building roof or top of the mountain, could keep minimum interference from GNSS multiple paths and signal block. Figure 2 shows the site views at four typical permanent GNSS stations in the PRVI region, all of which were installed

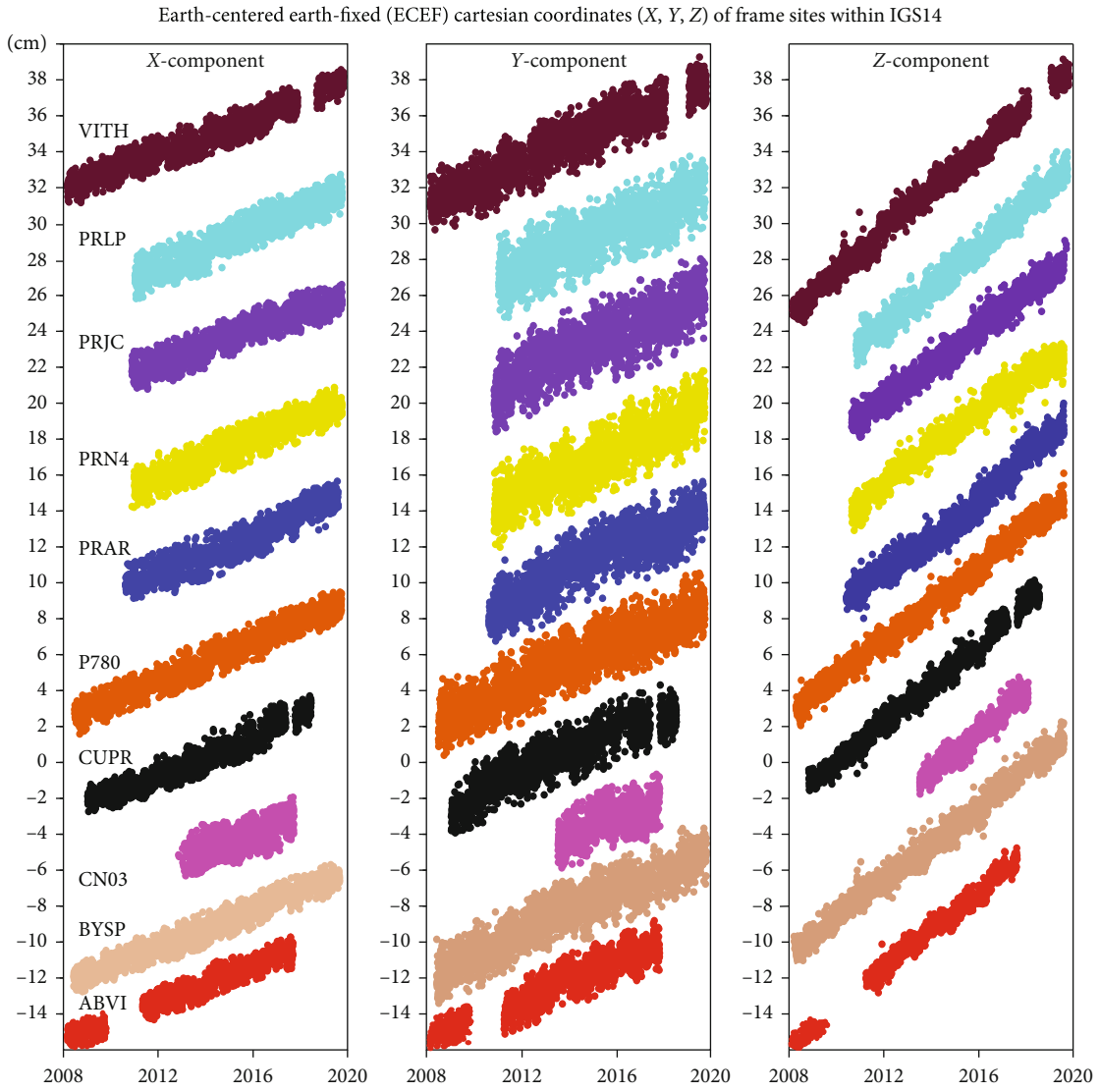


Figure 3: Plots showing the geocentric positional time series (*X*, *Y*, *Z*) of the ten frame sites with respect to the global reference frame IGS14.

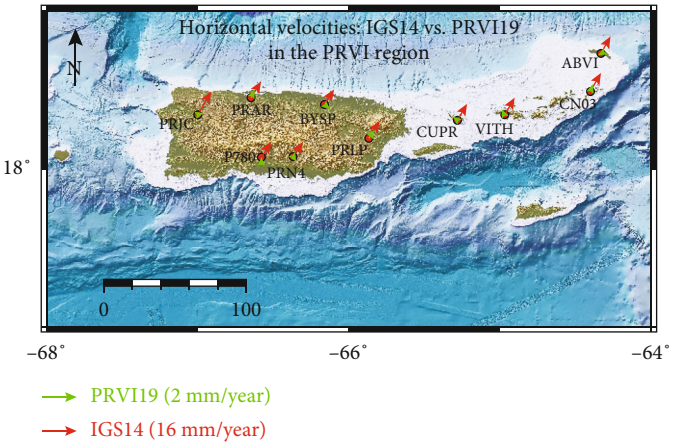


Figure 4: Map showing the locations of the ten selected GNSS reference stations within the PRVI region. The red velocity vectors are referred to the IGS14 reference frame. The green velocity vectors are referred to the PRVI19 reference frame.

Table 1: Detailed information of the ten reference stations and the site velocities referred to IGS14 and PRVI19 reference frames.

| Reference GNSS | Location (degree) | | | Site velocity | | | | | | Uncertainty of the velocity (mm/year)** | | |
|---|---|---|---|---|---|---|---|---|---|---|---|---|
| | | | | IGS14, mm/year | | | PRVI19, mm/year | | | | | |
| | Location | Longitude | Latitude | EW | NS | UD | EW | NS | UD | EW | NS | UD |
| P780 | Ponce, PR | -66.5791 | 18.075 | 8.9 | 13.8 | -0.3 | 0.1 | 0.1 | -0.3 | 0.2 | 0.2 | 0.8 |
| BYSP | Bayamón, PR | -66.1612 | 18.408 | 8.8 | 13.8 | -0.5 | 0.2 | -0.2 | -0.9 | 0.2 | 0.2 | 0.8 |
| PRJC | San Sebastian, PR | -66.9995 | 18.342 | 9.0 | 13.6 | -0.8 | 0.4 | 0.1 | -0.9 | 0.3 | 0.3 | 1.0 |
| PRLP | Las Piedras, PR | -65.8683 | 18.195 | 9.3 | 14.8 | 0.1 | 0.5 | 0.7 | -0.1 | 0.3 | 0.3 | 1.0 |
| PRAR | Cercadillo, PR | -66.647 | 18.450 | 8.9 | 14.4 | -0.5 | 0.3 | 0.7 | -0.9 | 0.3 | 0.3 | 0.9 |
| PRN4 | Coamo, PR | -66.369 | 18.079 | 9.0 | 13.6 | 0.6 | 0.2 | -0.3 | 0.6 | 0.3 | 0.3 | 1.1 |
| CUPR | Culebra Island, PR | -65.2825 | 18.307 | 8.5 | 14.6 | -0.5 | -0.3 | 0.2 | -0.9 | 0.3 | 0.3 | 1.0 |
| VITH | St. Thomas Island, USVI | -64.9692 | 18.343 | 8.6 | 14.8 | -0.1 | -0.1 | 0.2 | -0.5 | 0.2 | 0.3 | 0.9 |
| CN03 | Gorda Peak, BVI | -64.403 | 18.490 | 8.9 | 15.5 | -0.2 | 0.2 | 0.6 | -0.5 | 0.4 | 0.4 | 1.3 |
| ABVI | Anegada Island, BVI | -64.3325 | 13.730 | 8.4 | 14.9 | -0.3 | -0.2 | -0.1 | -0.9 | 0.3 | 0.3 | 1.0 |

*PR: Puerto Rico; USVI: U.S. Virgin Islands; BVI: British Virgin Islands. **The uncertainty represents the 95% confidence interval of the velocity estimate.

Table 2: Seven parameters for Helmert reference frame transformation from IGS14 to PRVI19.

| Parameters | Unit | IGS14 to PRVI19 |
|---|---|---|
| dTx | m/year | 2.652437*E*-02 |
| dTy | m/year | -2.130450*E*-02 |
| dTz | m/year | -9.310699*E*-02 |
| dRx | Radian/year | 1.386115*E*-08 |
| dRy | Radian/year | 1.273412*E*-09 |
| dRz | Radian/year | 5.511930*E*-09 |
| $t_0$ | 1/year | 2015.0 |

*Counterclockwise rotations of axes ($X$, $Y$, $Z$) are positive.

in the open area to avoid the GNSS signal block or multipath effects, with solid monuments, i.e., the short-drilled braced monument, and building mount monument.

The climate impacts the seasonal ground deformation, and different climate factors perform different impact weights in the GNSS time series. In this study, PRVI region that presently follows a tropical rainforest climate is selected to test the hybrid method. The area has recorded an annual mean temperature of 28°C, and it has a trend of increasing since the 1950s [35]. The precipitation records show a long-term trend of decreasing precipitation in the northern area and show historically drier with a positive rainfall trend in the southern area [36]. Since the PRVI is one of the islands located in the Caribbean region, it has a wind speed of 10 mph~14 mph which is recorded at 10 meters above the ground. However, hurricane activity has increased since 1995. This increase in hurricane activity may also be a result of natural variability [37]. Also, historical records from tide gauges since 1900 show a Sea Level Rise (SLR) of 1.7 mm/year. Recent satellite-based remote sensing technology shows a SLR rate of 3.2 mm/year since 1992 [38]. Moreover, since the snow/ice has different characteristics in a variety of areas (such as Alaska and Texas in the U.S), it leads to a tremendously different impact weight in GNSS time series [39]. Notably, we expect the hybrid method to be fully tested and have the characteristics of generality and efficiency. Thus, we select the location without snow/ice to test the hybrid method. Besides, to precisely evaluate the impact caused by different climate factors, the selected study area needs to have consistent climate data. We choose to use the original daily climate monitoring continuous station which is installed near the permanent continuous GNSS station in the PRVI region.

## 3. Results

*3.1. PRVI19 Local Reference Frame.* This study used the GIPSY-OASIS software package (V6.4) to obtain daily solutions using the PPP method. Firuzabadi and King [40] and Wang [41] proposed an outlier detection and removing algorithm to clean the positional or displacement time series. On average, 6 ~ 7% of the total samples have been removed as outliers in this study. According to the previous investigations, daily PPP solutions would achieve 3-5 mm horizontal accuracy and 5-8 mm vertical accuracy in the PRVI area [30]. The PPP solutions of the GNSS stations are provided with respect to a global reference frame. The positional time series referred to the IGS14 global reference frame are shown in Figure 3. Also, the raw PPP solutions inevitably include the common background of global tectonic movements. Thus, the GNSS observations referred to a stable local reference frame could minimize the influence induced from the global background movements.

In this study, we used the extended Helmert transformation and selected ten permanent stations to realize the PRVI19 reference frame. The MIDAS method was used to calculate velocity and uncertainty [42]. The velocities of the ten selected reference stations with respect to different reference frames are shown in Figure 4. The locations of these permanent stations and corresponding site velocities referred to IGS14 and PRVI19, respectively, are listed in Table 1. The seven Helmert parameters for transforming the global IGS14 reference frame to the local PRVI19 reference frame are listed in Table 2. Moreover, the plate reconstructions

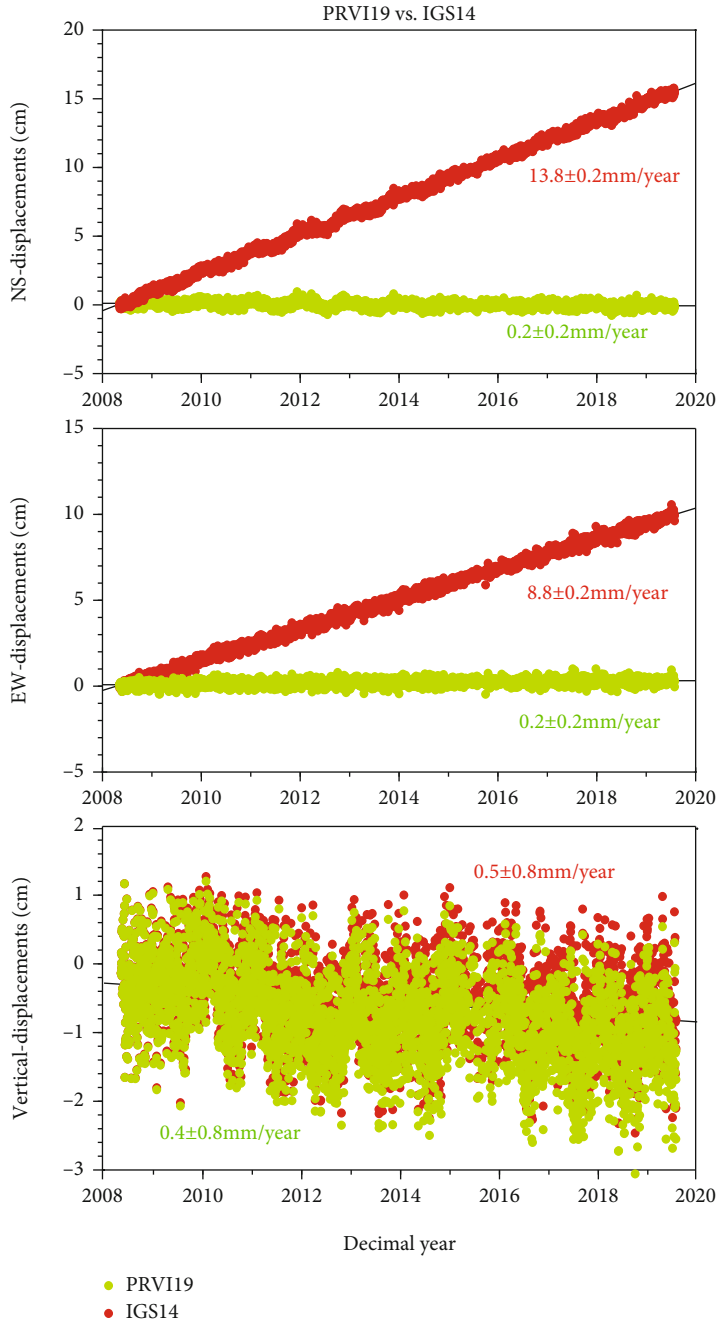


Figure 5: Plots showing the three-component displacement time series of the BYSP station with respect to two different scale reference frames: a global reference frame (IGS14) and a local reference frame (PRVI19). The green dots represent the displacements with respect to the PRVI19 reference frame during 2008-2020. The red dots represent the displacements referred to the IGS14 reference frame within the same period of time.

and geodynamic modeling are defined by the rigidity of tectonic plates. The stability of the local reference frame also relies on the assumption of the rigidity of the tectonic plate. The stability or the accuracy of the reference frame can be assessed by the average velocities of all reference stations with respect to the reference frame. Since the reference frame is defined by the reference stations, in an ideal situation, all reference stations should have no relative movement between each other with respect to the defined reference frame. Thus, if the PRVI region is recognized as a rigid microplate in tectonics, the stability of the local reference frame is to be 0 mm/year. However, in practice, a tectonic plate is not completely rigid, and it cannot be strictly stable. For PRVI19, the stability reaches approximately 0.4 mm/year in horizontal and approximately 0.5 mm/year in vertical. This level of accuracy is essential for studying millimeter-per-year ground motions in the PRVI region.

Theoretically, the longer length of GNSS data and better geographical distribution of reference stations can improve the stability of a reference frame. Wang et al. [18] updated

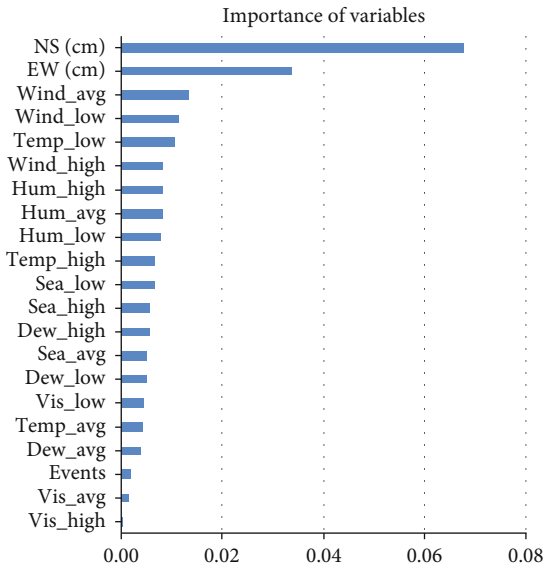


Figure 6: Plot showing the impact weights of different climate factors evaluated by the combined method. Sea: sea level; Temp: temperature; Hum: humidity; Vis: visibility. NS represents the North-South displacements. Events represent the operation log of weather station. EW represents the East-West displacements. Avg represents the average of daily values. Low represents the lowest daily value. High represents the highest daily value.

Table 3: XGBoost hyperparameters.

| | | |
|---|---|---|
| nrounds =400 | nthread =8 | eta=0.01 |
| Gamma =0.01 | max_depth =8 | min_child_weight =2 |
| Subsample =0.54 | colsample_bytree =0.54 | Lambda =0.01 |

the PRVI14 local reference frame to PRVI18 with the latest global reference frame (from IGS08 to IGS14) and reference stations. However, it indicated that there was no considerable improvement in reference frame stability. In this study, we established the local reference frame to PRVI19 with ten reference stations and a longer length of GNSS data. The PRGY, PRLT, and PRMI GNSS stations, which are located at southwestern and southern of the PRVI region, are excluded from reference stations. Those stations are located nearby the South Lajas fault which is an active Holocene structure within the past 5,000 years [43]. The Lajas Valley currently experiences a 1.5 mm/year north-south direction extension and minor right-lateral strike-slip [9]. Also, the MIPR station is excluded from the reference stations because it is close to P780 and PRN4 in geographic distribution, and the GNSS station stops recording data since October of 2017. Though the location of MIPR station can form well geographical distribution for the local reference frame, we still excluded it from the reference stations because P780 station has better quality and longer length of data and locates in the same area. However, the stability of the PRVI19 still does not considerably increase compared with the previous two local reference frames, i.e., PRVI14 and PRVI18 [18, 31]. Based on the previous versions of local reference frames and PRVI19, it proves that the stability of the PRVI19 local reference frame is approaching the rigidity of the PRVI tectonic block.

Figure 5 depicts nearly 13-year North-South, East-West, and vertical displacement time series at BYSP (2008-2020) with respect to the IGS14 and the PRVI19 reference frames. It shows a notable difference in horizontal velocities when referred to the global (IGS14) and local (PRVI19) reference frames. The 13 years of BYSP observations show that it has a velocity of $13.8 \pm 0.2$ mm/year in NS and a velocity of 8.8 $\pm 0.2$ mm/year in EW with respect to the global IGS14 reference frame; it has a velocity of $0.2 \pm 0.2$ mm/year in NS and a velocity of $0.2 \pm 0.2$ mm/year in EW with respect to the local PRVI19 reference frame, respectively. In general, most engineer monitoring applications only focus on the local target deformation displacements and do not consider the movements with respect to a global reference frame. The comparison of the BYSP GNSS time series within IGS14 and PRVI19 reference frames demonstrates that the background global or regional tectonic movements can bias or obscure the local ground deformation when using a global or regional reference frame.

*3.2. Daily Climate Impact Factors.* Climate change is considered as an important external impact factor influencing the GNSS data precision. However, it is a challenge to clarify the relationship between daily climate change and daily GNSS records. The main reasons are because the daily climate change influence could be partially removed by the 24-hour GNSS processing method. Thus, we selected the continuous operating GNSS station BYSP, which is installed nearby a real-time climate-monitoring device. The 5-year continuous climate data are used in the model, which is collected by the weather station (TJSJ) nearby the BYSP (NOAA National Weather Service). Here, we established two models between which the only difference is that one considers the daily climate features and the other not. We used the model to evaluate whether climate change can influence the precision of the 24-hour GNSS time series, which has been transformed to the PRVI19 reference frame using the extended Helmert transformation method. The dimensionless index shows that the model without considering the daily climate change is 0.32 and the other one considering the daily climate change is 0.25. The lower dimensionless index means that the model has better performance. The results prove that daily climate change is one of the impact factors in the GNSS time series.

Furthermore, we determined the quantitative weights of impact from different daily climate factors on the GNSS time series. Figure 6 shows the importance of the 20 selected climate factors on the GNSS time series using the XGBoost model. The XGBoost parameters used to evaluate the displacements are shown in Table 3. Each row displays the impact of the feature, in which the contribution weight is shown on the $x$-axis. Here, we used two complementary features, North-South (NS) feature and East-West (EW) feature, which are the physical movements due to the vertical displacements. Theoretically, the NS and EW observations should change when the GNSS station has vertical movements. For this reason, we involve the two features to help

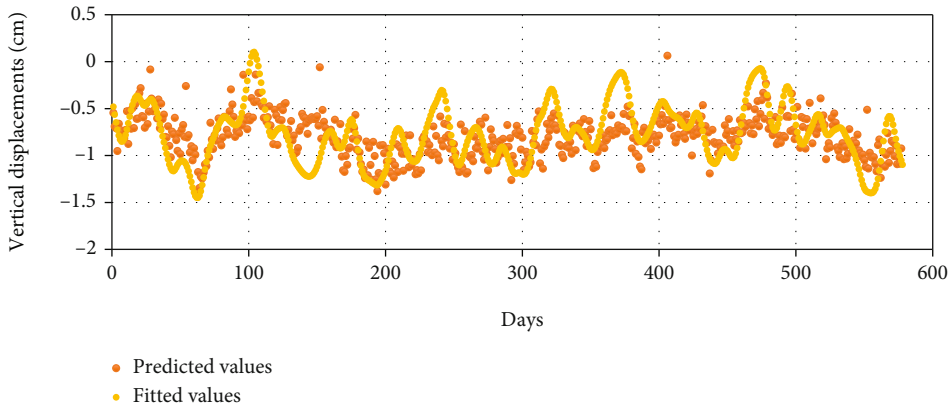


Figure 7: Plot showing the detailed comparisons between the fitted values from measured values and predicted values in 600 days. The orange dots represent the results predicted by the combined machine learning method. The yellow dots represent the fitted results based on GNSS records using the cubic spline method.

the hybrid model precisely evaluate different climate features and corresponding impact weights. The relationship between these two physical features is in good agreement with the results reported in Li et al. [44], which indicated that the key feature for the NS movements was the variance of the subsidence or uplift area. Based on the five years of monitoring climate records, we analyze the weight of different climate factors influencing the GNSS displacements. We found that the wind speed (average) and temperature (minimum) were the two climate factors that have the biggest impact on the daily GNSS time series. Interestingly, the humidity, temperature (average), and dew are not sensitive in the model. In the daily GNSS postprocessing records, except for the mega weather conditions, it is hard to determine the relationship between these features that can impact the vertical displacements.

*3.3. GNSS Time Series Prediction.* The hybrid model forecasted the GNSS monitoring displacements by learning the previous data and expected to explore the potential deformation problem in various monitoring applications. The prediction of GNSS observations is derived from the previous displacements that are referred to the stable local PRVI19 reference frame. Here, we used the BYSP GNSS postprocessing records referred to PRVI19 to train the model. The hybrid model was trained by the 1823 days of GNSS displacements. Also, we used the root mean square error (RMSE) as an indicator to evaluate the forecasting precision [45, 46]:

$$\mathrm{RMSE} = \sqrt{\frac{\sum(x-\bar{x})^2}{n}}, \tag{28}$$

where $x$ is the prediction value, $\bar{x}$ is the measured value, and $n$ is the sample size of test dataset. In the experiment, we need to use the prediction results to compare with real deformation results monitored by the GNSS station. However, the GNSS time series still inevitably include the nonlinear change, such as the noise, which is complex and hard to remove. Gazeaux et al. [47] tested different models and methods to minimize the white noise and colored noise such as the first-order Gauss Markov model and auto-regressive moving average model. However, the best noise model is location dependent, which is impacted by the location of the GNSS site, GNSS raw data processing method, and monument designs [48]. Thus, in the comparison, we used cubic spline function interpolation to fit the GNSS measured solutions, which have been transformed to PRVI19 [49]. Figure 7 shows the predicted model results compared with the post-fitted GNSS displacements using the cubic spline function in the experiment. We used optimized parameters for the cubic spline method and found the predicted values performed well. It shows that the RMSE of the forecasting method is 0.22, which is slightly lower than 0.31 from the fitted results using the cubic spline function. Moreover, we tested all parameters enrolled in the cubic spline method. It also shows that the precision of the forecasted results meets well with the spline fitted results, which are processed using the real raw GNSS records.

## 4. Conclusions

To precisely analyze the impact of various daily climate factors on the GNSS time series, we proposed a hybrid method and applied it in the PRVI area. We used the extended Helmert transformation method to establish the PRVI19 local reference frame, which could help avoid the bias of background global or regional tectonic movements in the GNSS time series when studying local ground deformation. The stability of the PRVI19 reference frame is approximately 0.4 mm/year and 0.5 mm/year in the horizontal and vertical directions, respectively. Also, we adopted the XGBoost algorithm and the highly stable PRVI19 local reference frame to quantitatively assess the effects of daily climate factors on the GNSS daily (24 hours) observations. Based on the 13 years of GNSS records referred to PRVI19 and climate data recorded by a nearby climate-monitoring device, we observed that the wind had the biggest impact on the GNSS time series. The results show that the average, lowest, and highest wind speeds are the first, second, and fourth-largest weights among all the climate factors. Besides, the result also

shows that the lowest temperature also greatly affects the GNSS displacements, which is the third-largest weight among all climate factors. This paper introduces a new method that can quantitatively determine the impact weights of different climate factors on the GNSS time series. Moreover, we used the model to predict the GNSS records and indicate users to explore potential deformation risk. It is hoped that this study can promote the applications of the GNSS techniques and improve the understanding of the impact of different climate factors on the GNSS monitoring time series.

## Data Availability

Data available in a publicly accessible repository. Data is available through http://geodesy.unr.edu/ and also appreciates the climate data from NOAA National Weather Service https://www.weather.gov/.

## Conflicts of Interest

The authors declared that they have no conflicts of interest to this work. We declare that we do not have any commercial or associative interest that represents a conflict of interest in connection with the work submitted.

## Authors' Contributions

Linchao Li and Hanlin Liu contributed to the conceptualization, methodology, data curation, and writing—original draft preparation. Hanlin Liu contributed to the visualization and investigation. Linchao Li contributed to the supervision. Linchao Li and Linqiang Yang contributed to the writing—reviewing and editing.

## Acknowledgments

The authors acknowledge Guoquan Wang (University of Houston) for providing the PPP solutions data quality check for this study. The first author also appreciates the UNAVCO and the Nevada Geodetic Laboratory (NGL) at the University of Nevada for sharing their GPS products with the public. Data is available through http://geodesy.unr.edu/ and also appreciates the climate data from NOAA National Weather Service https://www.weather.gov/. This research was funded by the National Key R&D Program of China (grant number 2019YFB2102700). This study was supported by the research funds from China Postdoctoral Science Foundation funded project (grant number 2020M682883), the Shenzhen Science and Technology program (grant number KQTD20180412181337494), and the Foundation for Distinguished Young Talents in Higher Education of Guangdong, China (Grant No. 2019KQNCX126).

## References

[1] R. A. Snay and T. Soler, "Continuously operating reference station (CORS): history, applications, and future enhancements," *Journal of Surveying Engineering*, vol. 134, no. 4, pp. 95–104, 2008.

[2] UNAVCO (University NAVSTAR Consortium), "Monumentation types," 2014, http://www.unavco.org/instrumentation/monumentation/types/types.html.

[3] G. Blewitt, "Carrier phase ambiguity resolution for the global positioning system applied to geodetic baselines up to 2000 km," *Journal of Geophysical Research: Solid Earth*, vol. 94, no. B8, pp. 10187–10203, 1989.

[4] X. Xu, D. Dong, M. Fang, Y. Zhou, N. Wei, and F. Zhou, "Contributions of thermoelastic deformation to seasonal variations in GPS station position," *GPS Solutions*, vol. 21, no. 3, pp. 1265–1274, 2017.

[5] D. Dong, P. Fang, Y. Bock, M. K. Cheng, and S. I. Miyazaki, "Anatomy of apparent seasonal variations from GPS-derived site position time series," *Journal of Geophysical Research: Solid Earth*, vol. 107, no. B4, pp. ETG 9-1–ETG 9-16, 2002.

[6] H. Yan, W. Chen, Y. Zhu, W. Zhang, and M. Zhong, "Contributions of thermal expansion of monuments and nearby bedrock to observed GPS height changes," *Geophysical Research Letters*, vol. 36, no. 13, 2009.

[7] H. Munekane, "Sub-daily noise in horizontal GPS kinematic time series due to thermal tilt of GPS monuments," *Journal of Geodesy*, vol. 87, no. 4, pp. 393–401, 2013.

[8] T. A. Herring, T. I. Melbourne, M. H. Murray et al., "Plate boundary observatory and related networks: GPS data analysis methods and geodetic products," *Reviews of Geophysics*, vol. 54, no. 4, pp. 759–808, 2016.

[9] W. Bertiger, Y. Bar-Sever, A. Dorsey et al., "GipsyX/RTGx, a new tool set for space geodetic operations and research," *Advances in Space Research*, vol. 66, no. 3, pp. 469–489, 2020.

[10] L. Yang, G. Wang, V. Huérfano, C. G. von Hillebrandt-Andrade, J. A. Martínez-Cruzado, and H. Liu, "GPS geodetic infrastructure for natural hazards study in the Puerto Rico and Virgin Islands region," *Natural Hazards*, vol. 83, no. 1, pp. 641–665, 2016.

[11] J. Geng and C. Shi, "Rapid initialization of real-time PPP by resolving undifferenced GPS and GLONASS ambiguities simultaneously," *Journal of Geodesy*, vol. 91, no. 4, pp. 361–374, 2017.

[12] J. Geng, X. Li, Q. Zhao, and G. Li, "Inter-system PPP ambiguity resolution between GPS and BeiDou for rapid initialization," *Journal of Geodesy*, vol. 93, no. 3, pp. 383–398, 2019.

[13] W. Bertiger, S. D. Desai, B. Haines et al., "Single receiver phase ambiguity resolution with GPS data," *Journal of Geodesy*, vol. 84, no. 5, pp. 327–337, 2010.

[14] Z. Altamimi, X. Collilieux, and L. Métivier, "ITRF 2008: an improved solution of the international terrestrial reference frame," *Journal of Geodesy*, vol. 85, no. 8, pp. 457–473, 2011.

[15] Z. Altamimi, P. Rebischung, L. Métivier, and X. Collilieux, "ITRF 2014: a new release of the International Terrestrial Reference Frame modeling nonlinear station motions," *Journal of Geophysical Research: Solid Earth*, vol. 121, no. 8, pp. 6109–6131, 2016.

[16] G. Blewitt, C. Kreemer, W. C. Hammond, and J. M. Goldfarb, "Terrestrial reference frame NA12 for crustal deformation studies in North America," *Journal of Geodynamics*, vol. 72, pp. 11–24, 2013.

[17] G. Blewitt and D. Lavallée, "Effect of annual signals on geodetic velocity," *Journal of Geophysical Research: Solid Earth*, vol. 107, no. B7, p. ETG 9-1, 2002.

[18] G. Wang, H. Liu, G. S. Mattioli, M. M. Miller, K. Feaux, and J. Braun, "CARIB18: a stable geodetic reference frame for

geological hazard monitoring in the Caribbean region," *Remote Sensing*, vol. 11, no. 6, p. 680, 2019.

[19] C. Pearson and R. Snay, "Introducing HTDP 3.1 to transform coordinates across time and spatial reference frames," *GPS Solutions*, vol. 17, no. 1, pp. 1–15, 2013.

[20] E. S. Abdolkarimi, G. Abaei, and M. R. Mosavi, "A wavelet-extreme learning machine for low-cost INS/GPS navigation system in high-speed applications," *GPS Solutions*, vol. 22, no. 1, p. 15, 2018.

[21] K. J. Bergen, P. A. Johnson, V. Maarten, and G. C. Beroza, "Machine learning for data-driven discovery in solid Earth geoscience," *Science*, vol. 363, no. 6433, article eaau0323, 2019.

[22] B. Rouet-Leduc, C. Hulbert, and P. A. Johnson, "Continuous chatter of the Cascadia subduction zone revealed by machine learning," *Nature Geoscience*, vol. 12, no. 1, pp. 75–79, 2019.

[23] B. J. Phrampus, T. R. Lee, and W. T. Wood, "A global probabilistic prediction of cold seeps and associated seafloor fluid expulsion anomalies (SEAFLEAs)," *Geochemistry, Geophysics, Geosystems*, vol. 21, no. 1, 2020.

[24] G. J. Anderson and D. D. Lucas, "Machine learning predictions of a multiresolution climate model ensemble," *Geophysical Research Letters*, vol. 45, no. 9, pp. 4273–4280, 2018.

[25] C. X. Ren, O. Dorostkar, B. Rouet-Leduc et al., "Machine learning reveals the state of intermittent frictional dynamics in a sheared granular fault," *Geophysical Research Letters*, vol. 46, no. 13, pp. 7395–7403, 2019.

[26] T. Soler and R. A. Snay, "Transforming positions and velocities between the International Terrestrial Reference Frame of 2000 and North American Datum of 1983," *Journal of Surveying Engineering*, vol. 130, no. 2, pp. 49–55, 2004.

[27] T. Chen and C. Guestrin, "Xgboost: a scalable tree boosting system," in *Proceedings of the 22nd acm sigkdd international conference on knowledge discovery and data mining*, pp. 785–794, New York, NY, USA, 2016.

[28] L. Breiman and J. H. Friedman, "Predicting multivariate responses in multiple linear regression," *Journal of the Royal Statistical Society: Series B (Statistical Methodology)*, vol. 59, no. 1, pp. 3–54, 1997.

[29] R. Ihaka and R. Gentleman, "R: a language for data analysis and graphics," *Journal of Computational and Graphical Statistics*, vol. 5, no. 3, pp. 299–314, 1996.

[30] G. Wang and T. Soler, "OPUS for horizontal subcentimeter-accuracy landslide monitoring: case study in the Puerto Rico and Virgin Islands region," *Journal of Surveying Engineering*, vol. 138, no. 3, pp. 143–153, 2012.

[31] H. Liu and G. Wang, "Relative motion between St. Croix and the Puerto Rico-Northern Virgin Islands block derived from continuous GPS observations (1995–2014)," *International Journal of Geophysics*, vol. 2015, Article ID 915753, 9 pages, 2015.

[32] U. S. ten Brink and A. M. López-Venegas, "Plate interaction in the NE Caribbean subduction zone from continuous GPS observations," *Geophysical Research Letters*, vol. 39, no. 10, 2012.

[33] B. Benford, C. DeMets, B. Tikoff, P. Williams, L. Brown, and M. Wiggins-Grandison, "Seismic hazard along the southern boundary of the Gônave microplate: block modelling of GPS velocities from Jamaica and nearby islands, northern Caribbean," *Geophysical Journal International*, vol. 190, no. 1, pp. 59–74, 2012.

[34] P. Mann, E. Calais, J. C. Ruegg, C. DeMets, P. E. Jansma, and G. S. Mattioli, "Oblique collision in the northeastern Caribbean from GPS measurements and geological observations," *Tectonics*, vol. 21, no. 6, pp. 7-1–7-26, 2002.

[35] D. J. Murphy, M. H. Hall, C. A. Hall, G. M. Heisler, S. V. Stehman, and C. Anselmi-Molina, "The relationship between land cover and the urban heat island in northeastern Puerto Rico," *International Journal of Climatology*, vol. 31, no. 8, pp. 1222–1239, 2011.

[36] A. E. Lugo, O. Ramos, and C. Rodriguez, *The Río Piedras Watershed and Its Surrounding Environment. FS-980*, vol. 46, US Department of Agriculture, Forest Service, International Institute of Tropical Forestry, 2011.

[37] J. Nyberg, B. A. Malmgren, A. Winter, M. R. Jury, K. H. Kilbourne, and T. M. Quinn, "Low Atlantic hurricane activity in the 1970s and 1980s compared to the past 270 years," *Nature*, vol. 447, no. 7145, pp. 698–701, 2007.

[38] W. W. V. Sweet, R. Kopp, C. P. Weaver et al., "Global and regional sea level rise scenarios for the United States," *NOAA technical report NOS CO-OPS*, vol. 83, 2017.

[39] Y. Li, X. Chang, K. Yu, S. Wang, and J. Li, "Estimation of snow depth using pseudorange and carrier phase observations of GNSS single-frequency signal," *GPS Solutions*, vol. 23, no. 4, p. 118, 2019.

[40] D. Firuzabadi and R. W. King, "GPS precision as a function of session duration and reference frame using multi-point software," *GPS Solutions*, vol. 16, no. 2, pp. 191–196, 2012.

[41] G. Wang, "GPS landslide monitoring: single base vs. network solutions: a case study based on the Puerto Rico and Virgin Islands permanent GPS network," *Journal of Geodetic Science*, vol. 1, pp. 191–203, 2011.

[42] G. Blewitt, C. Kreemer, W. C. Hammond, and J. Gazeaux, "MIDAS robust trend estimator for accurate GPS station velocities without step detection," *Journal of Geophysical Research*, vol. 121, no. 3, pp. 2054–2068, 2016.

[43] C. S. Prentice and P. Mann, "Paleoseismic study of the South Lajas fault: first documentation of an onshore Holocene fault in Puerto Rico. Active tectonics and seismic hazards of Puerto Rico, the Virgin Islands, and offshore areas," *Geological Society of America Special Paper*, vol. 385, pp. 215–222, 2005.

[44] Y. Li, C. Xu, L. Yi, and R. Fang, "A data-driven approach for denoising GNSS position time series," *Journal of Geodesy*, vol. 92, no. 8, pp. 905–922, 2018.

[45] L. Li, H. Zhou, H. Liu, C. Zhang, and J. Liu, "A hybrid method coupling empirical mode decomposition and a long short-term memory network to predict missing measured signal data of SHM systems," *Structural Health Monitoring*, p. 1475921720932813, 2020.

[46] Y. Lin, L. Li, H. Jing, B. Ran, and D. Sun, "Automated traffic incident detection with a smaller dataset based on generative adversarial networks," *Accident Analysis & Prevention*, vol. 144, article 105628, 2020.

[47] J. Gazeaux, S. Williams, M. King et al., "Detecting offsets in GPS time series: first results from the detection of offsets in GPS experiment," *Journal of Geophysical Research: Solid Earth*, vol. 118, no. 5, pp. 2397–2407, 2013.

[48] J. Langbein, "Noise in GPS displacement measurements from Southern California and Southern Nevada," *Journal of Geophysical Research: Solid Earth*, vol. 113, no. B5, 2008.

[49] C. Li, S. Huang, Q. Chen et al., "Quantitative evaluation of environmental loading induced displacement products for correcting GNSS time series in CMONOC," *Remote Sensing*, vol. 12, no. 4, p. 594, 2020.

Hindawi
Journal of Sensors
Volume 2021, Article ID 9985063, 8 pages
https://doi.org/10.1155/2021/9985063

*Research Article*

# Energy Management of Fuel Cell Vehicles Based on Model Prediction Control Using Radial Basis Functions

**Weiwei Xin**,[1] **Weiguang Zheng**,[1,2] **Jirong Qin**,[2] **Shangjun Wei**,[2] **and Chunyu Ji**[2]

[1]*School of Mechanical and Electrical Engineering, Guilin University of Electronic Technology, Guilin 541004, China*
[2]*Commercial Vehicle Technology Center, Dong Feng Liuzhou Automobile Co., Ltd., Liuzhou 545005, China*

Correspondence should be addressed to Weiguang Zheng; weiguang.zheng@foxmail.com

Received 18 March 2021; Revised 28 April 2021; Accepted 5 May 2021; Published 24 May 2021

Academic Editor: Aijun Yin



Energy management strategies can improve fuel cell hybrid electric vehicles' dynamic and fuel economy, and the strategies based on model prediction control show great advantages in optimizing the power split effect and in real time. In this paper, the influence of prediction horizon on prediction error, fuel consumption, and real time was studied in detail. The framework of energy management strategy was proposed in terms of the model prediction control theory. The radial basis function neural network was presented as the predictor to obtain the short-term velocity in the future. A dynamic programming algorithm was applied to obtain optimized control laws in the prediction horizon. Considering the onboard controller's real-time performance, we established a simple fuel cell vehicle mathematical model for simulation. Different prediction horizons were adopted on UDDS and HWFET to test the influence on prediction and energy management strategy. Simulation results showed the strategy performed well in fuel economy and real-time performance, and the prediction horizon of around 20 s was appropriate for this strategy.

## 1. Introduction

The transportation industry is one of the primary sources of energy consumption and exhaust emissions. Many technologies on NEVs (new energy vehicles) have high fuel efficiency and fewer emissions. As one of the most popular NEVs, FCVs (fuel cell vehicles) have huge development space in transportation, depending on their zero emission and high efficiency.

The vehicle with fuel cell stack as the single energy source has a poor dynamic response, and the practical solution is to add a short-term storage system to assemble a hybrid vehicle, thus improving the vehicle's drivability and dynamic. The most common short-term storage systems include battery and supercapacitor—the former can store more electricity due to its higher specific energy, and the latter has high power density. The hybrid vehicle's dynamic performance and fuel economy are related to the architecture, the components, and the energy management strategy of the vehicle [1]. The work focused on the optimization of fuel economy for FCV with an energy management strategy.

The vehicle propulsion system's power split is optimized by the energy management strategy when the dynamic vehicle performance is satisfied. Depending on the control method, energy management strategies include optimization-based and rule-based ones.

Current energy management strategies are mostly based on certain/fuzzy logic rules. Certain rule-based strategies are first presented to solve the power split for hybrid electric vehicles, and these strategies have been extensively applied to real vehicles such as Toyota's Mirai and Hyundai's Nexo. Fuzzy logic-based strategies, relying on the fuzzy processing of control variables and the threshold value, are more robust and adaptive than those based on specific rules.

Buntin et al. first proposed a switching logic control system for hybrid vehicles [2]. For the fuel cell/battery FCV configuration, Liu et al. designed a control strategy to realize the vehicle's cold start in terms of meeting the dynamic performance requirements [3]. Hemi et al. analysed the

performance of FCV's three configurations in the unknown driving cycle and real-time driving conditions [4]. However, the formulation of rule-based strategies relies on engineering experience, different from practical solutions.

Optimization-based strategies can be decided into instantaneous optimization, global optimization, and MPC-based (model-predictive-control-based) ones. The most popular instantaneous optimization strategy is ECMS (equivalent consumption minimization strategy), wherein the equivalent consumption of hydrogen in the fuel cell is changed into that of fuel in the battery, and the strategy is used to minimize the equivalent fuel consumption at each sampling time [5, 6]. Global optimization strategy, adopting the optimization algorithms such as DP (dynamic programming) [7, 8], Pontryagin's minimum principle [9], and pseudospectral method [10], can obtain the global optimal control laws following the certain drive cycle. And in addition to that, Lü et al. present a review of energy management system of fuel cell hybrid vehicle from the perspective of heuristic algorithm [11]. In a sense, the MPC-based strategy can be regarded as a compromise between instantaneous optimization and global optimization ones. In this strategy, the vehicle's short-term future demanded velocity is predicted by the constructed model, and the controller optimizes the control laws in the prediction horizons [12–14].

In this paper, a MPC-based energy management strategy for fuel cell vehicles was proposed, and the influence of prediction horizon was studied in detail. In the built MPC framework, a radial basis function (RBF) neural network was adopt as predictor to obtain the prediction speed, dynamic programming algorithm was employed as the solver to get the optimal trajectory of SOC, and different prediction horizons were tested in terms of prediction error, fuel consumption, and real-time performance. This work is based on fuel cell vehicles, but the method is applicable to other vehicles with two energy sources.

The remainder of this paper is organized as follows. The fuel cell vehicle power system's mathematical model is established in Section 2. The MPC-based energy management strategy is presented in Section 3, and Section 4 shows the simulation results. Section 5 shows the conclusion.

## 2. FCV Mathematical Model

*2.1. Vehicle and Drivetrain.* Figure 1 shows the studied vehicle structure. A vehicle propulsion system contains the fuel cell system and battery, which provide power to the motor during the vehicle operation. The bus voltage is provided by connecting the battery to the bus, and a unidirectional DC-DC converter is used to connect the fuel cell system to the bus. The vehicle operates with the kinetic energy provided by the DC motor.

When the impacts of lateral dynamics and rotating mass are ignored, the traction force $F_t$ can be calculated by

$$F_t = m\frac{dv}{dt} + \frac{1}{2}\rho C_d A_f v^2 + mgf\cos(\alpha) + mg\sin(\alpha), \quad (1)$$

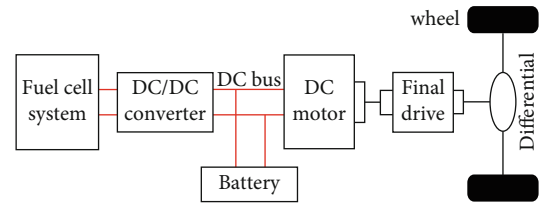


Figure 1: Structure of FCV. The red and black lines represent the electrical and mechanical connections of FCV, respectively.

where $m$ is the vehicle's total mass, $v$ is the vehicle's current velocity, $\rho$ is the air density, $A_f$ is the frontal area, $C_d$ is the aerodynamic drag's coefficient, $f$ is the rolling resistance coefficient, and $\alpha$ is the road's inclination angle. Table 1 shows the parameters of the fuel cell vehicle.

With the calculated traction force and velocity, the torque $T_w$ and the speed $\omega_w$ of wheels are given by

$$T_w = rF_t, \quad (2)$$

$$\omega_w = \frac{v}{r}, \quad (3)$$

where $r$ is the rolling radius of the wheel. When the wheel torque is positive, the motor exports kinetic energy to drive the vehicle; when it is negative, the vehicle is in the braking energy recycling, and the motor converts the braking energy into electricity to charge the battery. With the wheel torque and wheel speed, the torque $T_m$, the speed $\omega_m$, and the power demand $P_m$ of the motor are as follows.

$$T_m = \begin{cases} \dfrac{T_w}{\eta_{\text{fd}} r_{\text{fd}}}, & T_w \geq 0, \\ \dfrac{T_w \eta_{\text{fd}}}{r_{\text{fd}}}, & T_w < 0, \end{cases} \quad (4)$$

$$\omega_m = \omega_w r_{\text{fd}}, \quad (5)$$

$$P_m = \begin{cases} \dfrac{T_m \omega_m}{\eta_m}, & T_m \geq 0, \\ T_m \omega_m \eta_m, & T_m < 0, \end{cases} \quad (6)$$

wherein $\eta_{\text{fd}}$ and $r_{\text{fd}}$ are the efficiency and gear ratio of the final drive, respectively. The efficiency of the motor can be looked up in the motor's efficiency map.

It is defined that the motor power demand $P_m$ is positive during the traction phase and negative during the breaking phase. The fuel cell net power $P_{\text{fc}}$ is positive all the time, and the battery power $P_{\text{bat}}$ is positive when discharging and negative when charging. The relationship of three variables is written as

$$P_m = P_{\text{fc}} + P_{\text{bat}}. \quad (7)$$

*2.2. Fuel Cell System.* A 50 kW fuel cell system is chosen as the primary energy source of the vehicle. A complete onboard fuel cell system [15] contains a fuel cell stack and other auxiliary equipment such as a hydrogen storage system,

Table 1: Parameters of the fuel cell vehicle.

| Parameters | Value |
|---|---|
| Vehicle total mass (kg) | 1380 |
| Air density (kg/m$^3$) | 1.2 |
| Aerodynamic drag coefficient | 0.335 |
| Vehicle frontal area (m$^2$) | 2 |
| Wheel radius (m) | 0.282 |
| Gear ratio | 6.67 |
| Transmission efficiency (%) | 0.95 |
| Rolling resistance coefficient | $0.9e-2$ |

hydrogen circuit, air circuit, water circuit, and coolant circuit. The complete model can obtain the fuel cell system's detailed internal dynamic responses, but cost more time. In this work, a simplified model is adopted to obtain a rapid response. The net power $P_{fc}$ can be divided into the stack power $P_{stack}$ and the auxiliary power $P_{aux}$ as

$$P_{fc} = P_{stack} + P_{aux}. \tag{8}$$

The hydrogen consumption rate $\dot{m}_{H_2}$ can be written as the function of the stack current $I_{stack}$:

$$\dot{m}_{H_2} = \frac{NM_{H_2}}{nF} I_{stack}, \tag{9}$$

where $N$ is the number of cells, $M_{H_2}$ is the molar mass of hydrogen, $F$ is the Faraday constant, and $n$ is the number of electrons lost in electrochemical reactions.

The net power is a function of the stack current, and the hydrogen consumption rate can be described as a function of the net power. Figure 2 shows the relationship between them.

The efficiency $\eta_{fc}$ of a fuel cell system is defined as a function of the net power and the power provided by hydrogen:

$$\eta_{fc} = \frac{P_{fc}}{\dot{m}_{H_2} LHV}, \tag{10}$$

where LHV is the low heating value of hydrogen.

*2.3. Battery.* Figure 3 shows a typical physical model of battery. In this model, the battery can be denoted by an ideal voltage source in series with internal resistance. The output power of the battery can be written as

$$P_b = V_{oc} I_b + I_b^2 R_{int}, \tag{11}$$

where $V_{oc}$, $I_b$, and $R_{int}$ are the open-circuit voltage, the terminal current, and the internal resistance of the battery, respectively.

The open-circuit voltage and the internal resistance are the functions of the SOC and the temperature. The test can be used to obtain internal resistance and the relationship between the open-circuit voltage and SOC (see Figure 4).

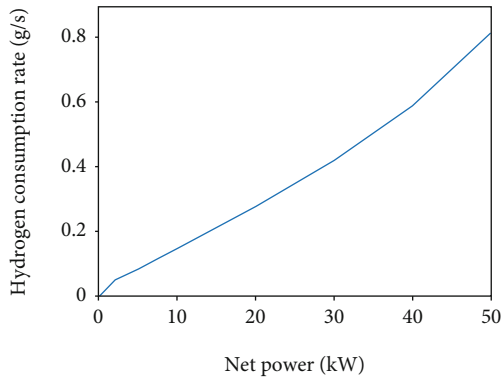


Figure 2: Curve of hydrogen consumption rate.

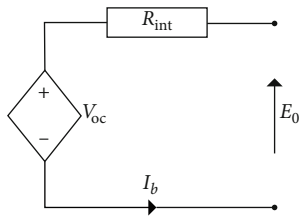


Figure 3: Equivalent circuit of the battery.

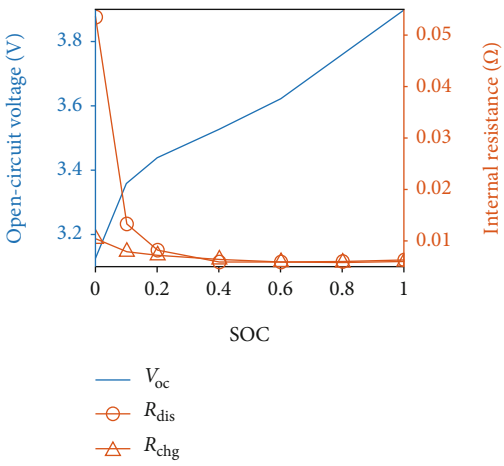


Figure 4: Curves of open-circuit voltage and internal resistance of the battery.

The battery temperature is assumed to be constant in this work.

The change rate of SOC is defined as the ratio of the terminal current and the battery capacity:

$$\dot{SOC} = -\frac{I_b}{Q_b}, \tag{12}$$

where $\dot{SOC}$ is the change rate of SOC and $Q_b$ is the battery capacity. With formulas (11) and (12), the change rate of SOC is calculated by

$$\dot{SOC} = -\frac{V_{oc} - \sqrt{V_{oc}^2 - 4P_b R_{int}}}{2R_{int} Q_b}. \tag{13}$$

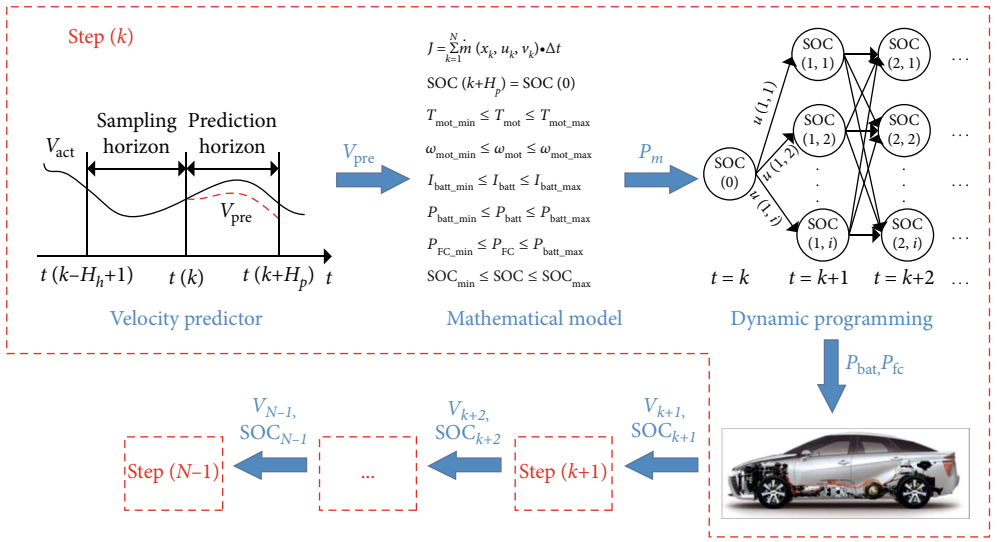


Figure 5: Structure of MPC-based energy management strategy.

Every single battery has a capacity of 6 Ah and a peak voltage of 3.8 V. A battery pack is constituted with 87 cells in series and three battery packs formed by the parallel connection for simulation.

## 3. MPC-Based Energy Management Strategy

*3.1. Structure of MPC-Based Energy Management Strategy.* With the transformation of global optimization into a series of suboptimizations, MPC can obtain the optimal local control laws based on model prediction, rolling optimization, and feedback correction. In Figure 5, the typical MPC-based energy management strategy consists of three steps [16].

*Step 1.* Predict the vehicle's future short-term velocity through the constructed prediction model.

*Step 2.* Obtain the optimal control rules in the short-term drive cycle by minimizing the cost function.

*Step 3.* Apply the optimal control rules in the first time step of the prediction horizon to vehicles' control system. Repeat the above steps until the drive cycle ends.

The whole system is discretized into constrained optimization problems in the finite time domain, and DP algorithm [17, 18] is employed as the solution algorithm. The power split factor and SOC are selected as the control variable and state variable, respectively. Therefore, the system function at each prediction step is described as

$$x_{k+1} = x_k + f_k(x_k, u_k, v_k), \quad k = 1, 2, \cdots, N, \tag{14}$$

where $x_k$ is the battery's SOC, $u_k$ is the power split factor, $v_k$ is the prediction velocity, and $N$ is the length of drive cycle.

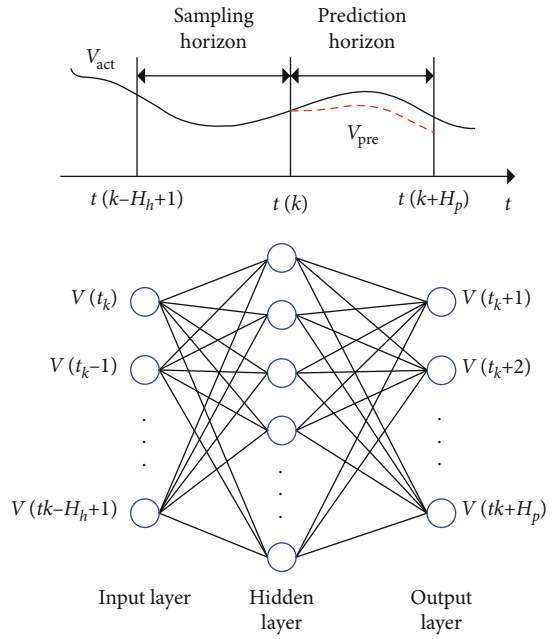


Figure 6: Structure of neural network predictor.

The fuel consumption is employed as the cost function:

$$J = \sum_{k=1}^{N} \dot{m}(x_k, u_k, v_k)\Delta t, \tag{15}$$

where $\dot{m}(x_k, u_k v_k)$ is the fuel consumption per step and $\Delta t$ is the rolling step length (1 s).

For the structure of fuel cell vehicle, a terminal constraint is implemented to the SOC at every control horizon

$$\mathrm{SOC}(k + H_p) = \mathrm{SOC}(0), \tag{16}$$

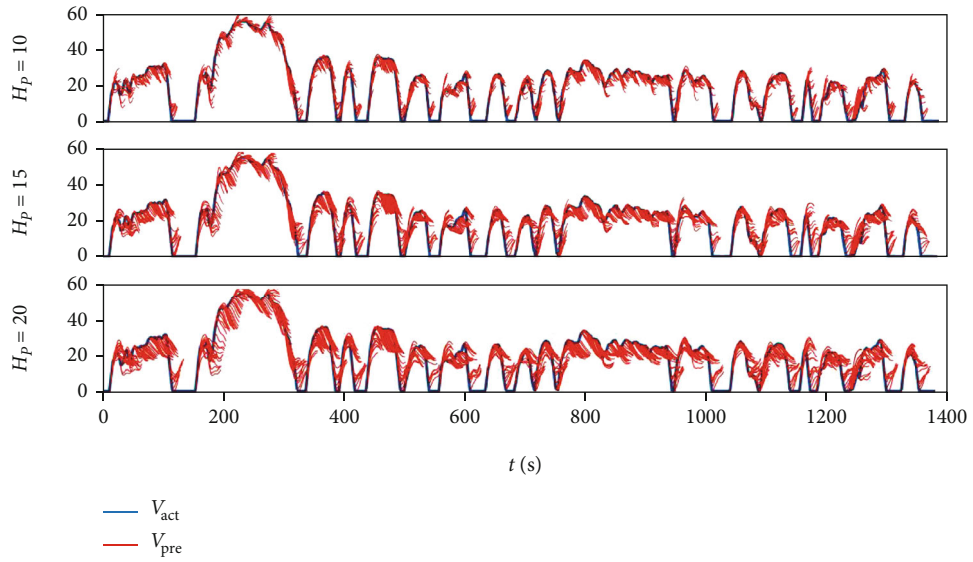


Figure 7: Prediction results for UDDS in three horizons.

where $\mathrm{SOC}(k + H_p)$ is the terminal target SOC of every control horizon and $H_p$ is the length of the prediction horizon.

$$\begin{cases} T_{\text{mot-min}} \le T_{\text{mot}} \le T_{\text{mot-max}}, \\ \omega_{\text{mot-min}} \le \omega_{\text{mot}} \le \omega_{\text{mot-max}}, \\ I_{\text{batt-min}} \le I_{\text{batt}} \le I_{\text{batt-max}}, \\ P_{\text{batt-min}} \le P_{\text{batt}} \le P_{\text{batt-max}}, \\ P_{\text{FC-min}} \le P_{\text{FC}} \le P_{\text{FC-max}}, \\ \text{SOC}_{\min} \le \text{SOC} \le \text{SOC}_{\max}. \end{cases} \tag{17}$$

Other parameters under constraints are shown in equation (17).

*3.2. Velocity Prediction with Neural Network.* The neural networks can respond to the nonlinear relationship between inputs and outputs through training the black-box model. In this work, a neural network of the radial basis function is trained to predict the velocity.

In Figure 6, the neural network inputs are the historical velocity sequence $[V(t_{k-H_h+1}), V(t_k)]$; the outputs are the prediction velocity sequence $[V(t_{k+1}), V(t_{k+H_p})]$ in the future; $H_h$ is the sampling horizon length; $H_p$ is the length of prediction horizon. The Gaussian function is selected as the activation function of the hidden layer, which is formulated as

$$a_j^1 = \exp\left(-\frac{\|\text{IW} - P\|^2}{2b^2}\right), \tag{18}$$

where IW is the neural network center, $P$ is the input vector, and $b$ is the maximum width between selected centers.

Here, a RBF-neural network with the structure of 10-50-$H_p$ is constructed to predict the velocity. Seven standard drive cycles (ARB-02, LA92, NYCC, REP05, SC03, UNIF01, and US06), including urban, suburban, and highway conditions, are used for the network training; 70% of the data are employed as the training dataset and 30% as the test dataset. In addition, untrained drive cycle (UDDS) and highway fuel economy test (HWFET) are used as the validate dataset.

## 4. Simulation Results and Discussion

The simulation was performed at MATLAB 2018b on a laptop with the configurations of Inter Core i3-3227U CPU @ 1.90 GHz. Seven drive cycles were used to train the network, the other two was used to test the performance of the network and the MPC-based energy management strategy. It was defined that the sampling time $H_h$ was 10 s, and the prediction time $H_p$ was 5 s to 25 s. The initial SOC of the battery was 0.6, and the terminal target SOC per prediction horizon was set as the same value of initial SOC. The upper and lower boundaries of SOC were 0.5 and 0.7, respectively. Also, the average root mean squared error (RMSE) was employed to assess the network performance, formulated as

$$\text{RMSE}(i) = \sqrt{\frac{\sum_{j=1}^{H_p}\left(v_{\text{pre}}^{ij} - v_{\text{act}}^{ij}\right)^2}{H_p}}, \tag{19}$$

$$\text{RMSE}_{\text{ave}} = \frac{\sum_{i=1}^{N}\text{EMSE}(i)}{N}, \tag{20}$$

where $\text{RMSE}(i)$ is the RMSE of prediction for the prediction horizon (from $i+1$ seconds to $i+H_p$ seconds) at step $i$, $\text{RMSE}_{\text{ave}}$ is the global average RMSE of prediction, and $N$ is the length of the drive cycle.

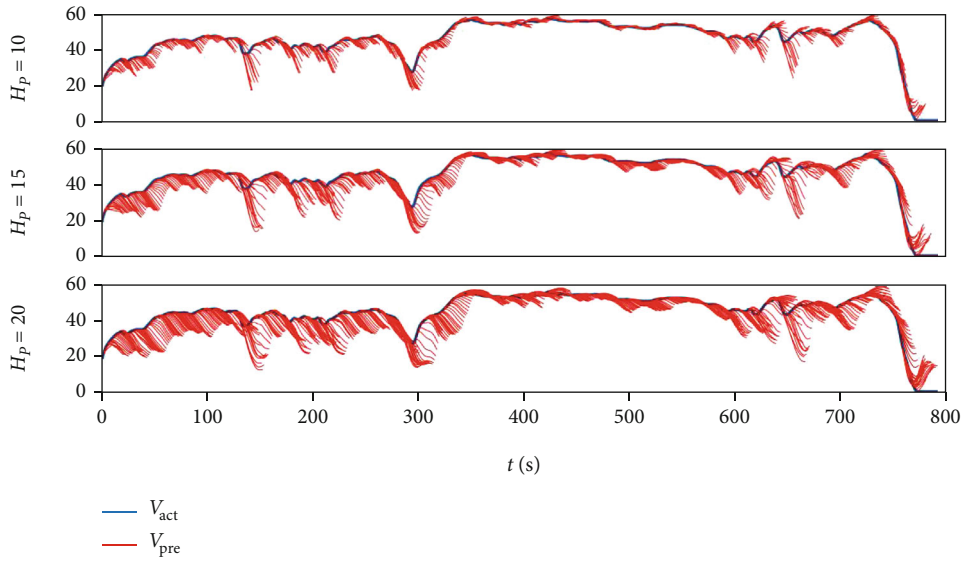


Figure 8: Prediction results for HWFET in three horizons.

In fact, with the structure of MPC, the final SOC for the global time horizon is practically impossible to have $\mathrm{SOC}(0) = \mathrm{SOC}(N)$. SOC deviation is converting into equivalent hydrogen consumption to eliminate the impact above.

To evaluate the performance of the constructed controllers, DP-based energy management strategy is employed as the benchmark of the simulation. It should be noted that unlike the DP algorithm mentioned in Section 3.1, the DP-based energy management strategy selected there is a global optimization strategy, aiming to obtain the optimal control rules and the hydrogen consumption at the whole drive cycle.

Different prediction horizons are tested in this work to explore the effect of the prediction horizon on fuel economy. Figure 7 shows the results of UDDS in prediction horizons are 10 s, 15 s, and 20 s. The prediction results of three prediction horizons reflect the changing trend of velocity without exception; however, with the increasing reduction horizon, the predicted velocity is further different from the actual velocity, which means the prediction error increases. Figure 8 presents the results of HWFET in the prediction horizons are 10 s, 15 s, and 20 s, and it shows the same trends as the results of UDDS; however, it is obvious that the prediction results of HWFET are more close to the actual velocity trajectory compared with UDDS.

Figures 9 and 10 show the SOC trajectories for UDDS and HWFET, respectively. Each figure includes 4 SOC trajectories, 3 of which are obtained with three predictors (the prediction horizons are 10 s, 15 s, and 20 s, respectively) and the other one is obtained with DP-based energy management strategy. In these two figures, the SOC trajectory of DP is different from these trajectories of MPC; this is related to the optimization horizons of the two algorithms. Benefiting from global optimization, the SOC trajectory planned by the DP algorithm is optimal for the specific drive cycle, whereas the MPC-based energy management strategy obtains a locally optimal SOC trajectory at every prediction

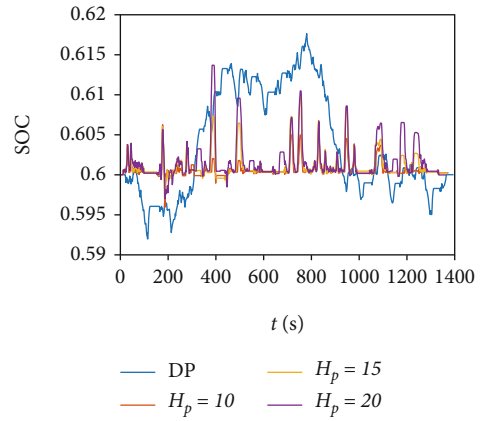


Figure 9: SOC trajectories of DP and MPC for UDDS.

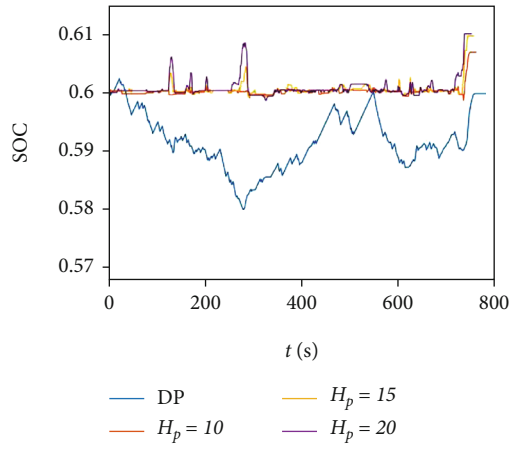


Figure 10: SOC trajectories of DP and MPC for HWFET.

Table 2: Simulation results at different horizons of MPC for UDDS.

| $H_h$ (s) | $H_p$ (s) | $EMSE_{ave}$ | SOC (N) | $T_{cal}$ (s) | $C_{H_2}$ (g) |
|---|---|---|---|---|---|
| 10 | 5 | 2.1279 | 0.602 | 0.071 | 140.95 |
| 10 | 10 | 3.9320 | 0.604 | 0.120 | 119.14 |
| 10 | 15 | 6.0122 | 0.604 | 0.168 | 111.39 |
| 10 | 20 | 7.5998 | 0.604 | 0.213 | 110.34 |
| 10 | 25 | 9.0285 | 0.604 | 0.267 | 109.58 |

Table 3: Simulation results at different horizons of MPC for HWFET.

| $H_h$ (s) | $H_p$ (s) | $EMSE_{ave}$ | SOC (N) | $T_{cal}$ (s) | $C_{H_2}$ (g) |
|---|---|---|---|---|---|
| 10 | 5 | 1.3259 | 0.6035 | 0.073 | 130.66 |
| 10 | 10 | 2.4245 | 0.6063 | 0.127 | 129.58 |
| 10 | 15 | 4.1004 | 0.6099 | 0.169 | 126.99 |
| 10 | 20 | 5.7272 | 0.6098 | 0.207 | 122.86 |
| 10 | 25 | 7.3255 | 0.6102 | 0.247 | 125.77 |

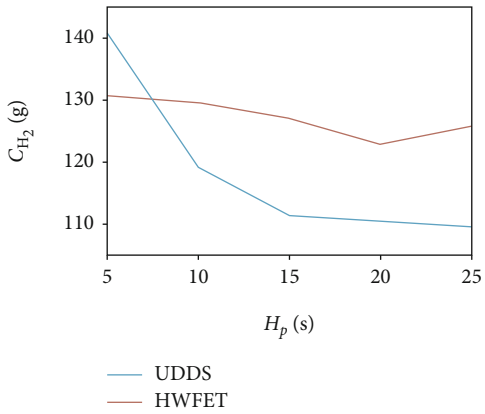


Figure 11: $H_2$ consumption for the different prediction horizons.

horizon. And for the MPC-based energy management strategy, with the same constraints in the final SOC, the battery's power split capacity can be improved by increasing the prediction horizon.

To explore the relationship between prediction error, prediction horizon, and fuel consumption, the hydrogen consumption at different prediction horizons for UDDS and HWFET is shown in Tables 2 and 3, respectively. In these tables, the calculated time $T_{cal}$ of MPC is the optimized time of each prediction horizon, and for the DP, it is the entire drive cycle. For the UDDS, it should be noted that with the increasing of prediction horizon $H_p$, the prediction accuracy $EMSE_{ave}$ decreases, and the fuel economy $C_{H_2}$ improves. The subsequent problem is that the calculated time $T_{cal}$ increases; while for the HWFET, with the increasing of prediction horizon, the fuel economy improves first and then decreases, and the best fuel consumption could be obtained at $H_p = 20$ s. These trends are shown in Figure 11 obviously.

Table 4: Comparison of MPC and DP for two drive cycles.

| Type | $H_p$ (s) | SOC (N) | $T_{cal}$ (s) | $C_{H_2}$ (g) | Normalized average (%) |
|---|---|---|---|---|---|
| UDDS-MPC | 20 | 0.6046 | 0.2132 | 110.34 | 87.42 |
| UDDS-DP | — | 0.6 | 113.60 | 98.01 | 100 |
| HWFET-MPC | 20 | 0.6098 | 0.207 | 122.86 | 90.09 |
| HWFET-DP | — | 0.6 | 65.44 | 111.79 | 100 |

As an onboard controller, the real-time performance of strategy should also be considered. The simulation time at laptop is 0.213 s with the prediction horizon 20 s; this data shows that the MPC-based energy management strategy has a real-time basis. In this work, considering the requirements of energy management strategy on fuel consumption and real-time performance, the prediction horizon is selected to be 20 s. The following analysis is established in the selected horizon. Table 4 shows the comparison between MPC-based and DP-based energy management strategy. In terms of fuel economy, the strategy's effect based on model predictive control (with 20 s as the prediction horizon's length) can reach 87.42% of DP-based in UDDS, while in HWFET, benefiting from a smaller forecast error, this data can rise to 90.09%.

## 5. Conclusions

Based on the simple vehicle model, the RBF-based predictor, and the DP-based solving algorithm, the work presented an MPC-based energy management strategy on a fuel cell vehicle. Models with different prediction horizons were built to study the influence of the prediction time steps.

Simulation results showed that the fuel economy performed best with 25 s as the prediction horizon for UDDS, while for HWFET the best fuel economy appeared at 20 s. In addition, large prediction horizon led to the longer optimizing time. In fact, to a real vehicle, in addition for energy management strategy, the onboard controller also needs to process a lot of real-time data from other components, which may result in much greater actual processing time than simulation. With this in mind, the prediction horizon of around 20 s is appropriate for the onboard MPC-based energy management strategy.

Although the structure of MPC-based energy management strategy is studied in this work, the results are based on the single prediction model with RBF neural network as the frame. In the future, prediction models with multiple algorithms will be studied to obtain the batter predictor.

## Data Availability

The dataset and codes of this paper for the simulation are available from the corresponding author if requested.

## Conflicts of Interest

The authors declare that there is no conflict of interest regarding the publication of this paper.

## Acknowledgments

The study was supported by the Innovation-Driven Development Special Fund Project of Guangxi (Guike AA18242033), Liuzhou Science Research and Planning Development Project (2020GAAA0403 and 2019AD10203), Liudong Science and Technology Project (20200108), and Innovation Project of Guet Graduate Education (2019YCXS008).

## References

[1] Y. L. Murphey, Jungme Park, Zhihang Chen, M. L. Kuang, M. A. Masrur, and A. M. Phillips, "Intelligent hybrid vehicle power control—part I: machine learning of optimal vehicle power," *IEEE Transaction on Vehicular Technology*, vol. 61, no. 8, pp. 3519–3530, 2012.

[2] D. L. Buntin and J. W. Howze, "A switching logic controller for a hybrid electric/ICE vehicle," in *American Control Conference*, pp. 1169-–11175, Seattle, Washington, 1995.

[3] L. Danwei and L. Hui, "Dynamic modeling and control design for bi-directional DC-DC converter for fuel cell vehicle with battery as energy storage element," in *Industry Applications Conference*, pp. 1632–1635, Kowloon, Hong Kong, China, 2005.

[4] H. Hemi, J. Ghouili, and A. Cheriti, "A real time fuzzy logic power management strategy for a fuel cell vehicle," *Energy Conversion and Management*, vol. 80, pp. 63–70, 2014.

[5] G. Paganelli, S. Delpra, T. M. Guerra, J. Rimaux, and J. J. Santin, "Equivalent consumption minimization strategy for parallel hybrid powertrains," in *Vehicular Technology Conference. IEEE 55th Vehicular Technology Conference. VTC Spring 2002*, pp. 2076–2081, Birmingham, AL, USA, 2002.

[6] W. Zhang, J. Li, L. Xu, and M. Ouyang, "Optimization for a fuel cell/battery/capacity tram with equivalent consumption minimization strategy," *Energy Conversion and Management*, vol. 134, pp. 59–69, 2017.

[7] W. Zhou, L. Yang, Y. Cai, and T. Ying, "Dynamic programming for new energy vehicles based on their work modes part II: fuel cell electric vehicles," *Journal of Power Sources*, vol. 407, pp. 92–104, 2018.

[8] D. Fares, R. Chedid, F. Panik, S. Karaki, and R. Jabr, "Dynamic programming technique for optimizing fuel cell hybrid vehicles," *International Journal of Hydrogen Energy*, vol. 40, no. 24, pp. 7777–7790, 2015.

[9] Y. Kim, M. Figueroa-Santos, N. Prakash, S. Baek, J. B. Siegel, and D. M. Rizzo, "Co-optimization of speed trajectory and power management for a fuel- cell/battery electric vehicle," *Applied Energy*, vol. 260, article 114254, 2020.

[10] W. Zhou, C. Zhang, J. Li, and H. K. Fathy, "A pseudospectral strategy for optimal power management in series hybrid electric powertrains," *IEEE Transactions on Vehicular Technology*, vol. 65, pp. 4813–4825, 2016.

[11] X. Lü, Y. Wu, J. Lian et al., "Energy management of hybrid electric vehicles: a review of energy optimization of fuel cell hybrid power system based on genetic algorithm," *Energy Conversion and Management*, vol. 205, article 112474, 2020.

[12] S. di Cairano, D. Bernardini, A. Bemporad, and I. V. Kolmanovsky, "Stochastic MPC with learning for driver-predictive vehicle control and its application to HEV energy management," *IEEE Transactions on Control System Technology*, vol. 22, no. 3, pp. 1018–1031, 2014.

[13] C. Sun, F. Sun, and H. He, "Investigating adaptive-ECMS with velocity forecast ability for hybrid electric vehicles," *Applied Energy*, vol. 185, pp. 1644–1653, 2017.

[14] D. F. Pereira, F. D. C. Lopes, and E. H. Watanabe, "Nonlinear model predictive control for the energy management of fuel cell hybrid electric vehicles in real time," *IEEE Transactions on Industrial Electronics*, vol. 68, pp. 3213–3223, 2020.

[15] L. Guzzella and A. Sciarretta, *Vehicle Propulsion Systems Introduction to Modeling and Optimization*, Springer, 2nd Ed edition, 2013.

[16] Y. Huang, H. Wang, A. Khajepour, H. He, and J. Ji, "Model predictive control power management strategies for HEVs: a review," *Journal of Power Sources*, vol. 341, pp. 91–106, 2016.

[17] O. Sundstrom and L. Guzzella, "A generic dynamic programming Matlab function," in *18th IEEE Multi-Conference on System and control*, pp. 1625–1630, St. Petersburg, Russia, 2009.

[18] O. Sundström, D. Ambühl, and L. Guzzella, "On implementation of dynamic programming for optimal control problems with final state constraints," *Oil & Gas Science and Technology–Revue de l'Institut Français du Pétrole*, vol. 65, no. 1, pp. 91–102, 2010.

Hindawi
Journal of Sensors
Volume 2021, Article ID 9943153, 14 pages
https://doi.org/10.1155/2021/9943153

*Research Article*

# Quality Prediction of Strip in Finishing Rolling Process Based on GBDBN-ELM

**Shuang Li, Jian Wang, and Sen Chen**

*Computer Integrated Manufacturing System Research Center, College of Electronics and Information Engineering, Tongji University, Shanghai 201800, China*

Correspondence should be addressed to Shuang Li; 1930746@tongji.edu.cn

Received 18 March 2021; Revised 10 April 2021; Accepted 20 April 2021; Published 21 May 2021

Academic Editor: Aijun Yin



With the continuous development of the manufacturing industry, the requirement for strip steel quality is becoming higher and higher in automobile manufacturing, mechanical processing, and electronic and electrical industries. The precise control of strip quality depends on the accurate prediction of strip quality to a certain extent. However, the data collected by a large number of sensors on the complex strip production line and generated by the computer control system presents the characteristics of high dimensionality, high coupling, and nonlinearity, which brings difficulties to the prediction of strip quality. The continuous production of massive data in the production line also forces steel enterprises to seek new data mining methods, mining the relationship between sensor data to predict and control strip quality. To solve these problems, this paper proposes a GBDBN-ELM model, which is more efficient and more accurate than other algorithms. In this model, the RBM in DBN is replaced with GBRBM, so that RBM no longer depends on the binary distribution, can handle continuity values, and retain more data features. In order to solve the problem of too long DBN training time, this article replaces the BP network in DBN with an ELM regression model. The ELM model predicts the strip quality based on the extracted data abstract features, thereby improving the model's prediction accuracy and shortening the training time. In this paper, the GBDBN-ELM model is compared with the BP neural network, ELM, and DBN, and root mean square error, $R$ square coefficient of determination, and training time are selected as evaluation indexes of the models. The experimental results show that the improved GBDBN-ELM model can not only improve the accuracy of strip steel quality prediction but also shorten the time of model training. The model proposed in this paper has achieved good results in prediction accuracy and performance.

## 1. Introduction

In the industrial field, the steel industry is one of the national basic industries. Most of the raw materials, resources, and equipment of other industries are provided by the steel industry. The development of the steel industry has also led to the progress of construction, machinery, transportation, and other industries. Although the current international steel production is increasing year by year, the technology for rolling high-quality steel still needs to be improved. With the rapid development of industry and technology, many industries have higher and higher requirements for the quality of strip steel, such as infrastructure engineering, automobile manufacturing, mechanical processing, and electronic and electrical industries. Therefore, the improvement of strip quality has become one of the main tasks of the hot rolling production process. The strip quality can be estimated in advance through prediction, and then, the process parameters can be adjusted in time through computer calculations to achieve closed-loop control of the system, which can maximize the strip quality. Therefore, the strip quality prediction method has gradually become a hot spot in the steel industry.

The traditional rolling mill control relies on manual operation; the strip quality at the exit is controlled by simple electric pressing or manual pressing, without the participation of many sensors. The steel industry has bid farewell to traditional production modes with the extensive application and development of modern automatic control theory in the industrial field. The combination of modern equipment and advanced technology has made the strip production

process increasingly complex [1]. In the strip steel production process, multiple devices are organically connected. The process parameters and product quality parameters involved in the subproduction stage are various, and the relationship between the various parameters is complex. The parameters of each stage often present a hierarchical structure and are coupled with each other. It is difficult to describe these parameters with linear or simple nonlinear relationships [2].

Quality of the strips at the exit of hot continuous rolling mainly depends on the finishing mill. The change of strip width and thickness is caused by the rolling force from the vertical stand and horizontal stand in finishing rolling. The main factors affecting strip steel quality include rolling force, reduction position, inlet temperature, roll bending force, roll gap width, and rack speed. Moreover, factors such as water flow, motor current, oil film compensation, and lubrication also have a certain impact on the surface quality of the strip [3]. Most of these variables are coupled with each other and have serious nonlinearity, and some of them are difficult to measure, which also brings certain difficulties to the prediction of strip quality.

Moreover, with the development of technology, the production model has spread from physical space to virtual space, and the degree of digital production has gradually deepened. More sensors, data acquisition equipment, and computer network control system are involved in the production process. A large amount of raw data are produced in the strip production line every day. How to use these data reasonably and mine more knowledge for strip quality prediction and control is also a problem that needs to be studied.

In order to achieve closed-loop control of strip quality and advance adjustment of process parameters, and to solve the poor prediction accuracy of strip quality resulting caused by high-dimensional, highly coupled, nonlinear data, the main contributions of this paper are as follows.

This paper proposes a strip quality prediction model combining DBN and ELM. In the combined model, DBN is used to extract features from high-dimensional and high coupling input data, and ELM predicts strip quality according to the extracted data features.

Based on the DBN-ELM combined model, the RBM in the DBN model is replaced by GBRBM to solve the dependence on the binary distribution of the visible layer and hidden layer of RBM. The model is improved to the GBRBM-ELM model to suit the continuous value regression problem.

The feasibility of the model is analyzed from the aspects of prediction accuracy and model performance, and the prediction effect of the model is compared with that of BP, ELM, and DBN. The results show that the GBDBN-ELM model can improve the prediction accuracy while shortening the model training time.

The rest of this article is organized as follows: The second chapter introduces the research progress of strip quality prediction technology; the third chapter introduces the principle, network structure, and training method of the strip quality prediction model; the fourth chapter validates the model through the data on the production line of a steel company; the last chapter is a summary of this article.

## 2. Related Works

Quality prediction and quality control problems often use two types of methods, mathematical model methods and data mining techniques.

*2.1. Mathematical Model Methods.* In traditional quality control, the mathematical model is used to predict the quality parameters, and the variables such as temperature, pressure, element, and their relationship are described by mathematical formulas [4, 5]. But the process of establishing the mathematical model of strip quality is very complex, because in the rolling process, not only many physical quantities but also much thermodynamic knowledge is involved. The strip quality prediction based on the mathematical model ignores and simplifies the influence of many on-site factors, and the dynamic effects sometimes produce false results, leading to large errors. Later, people paid attention to deformation laws in the forming process, and the finite element method and finite element simulation software were applied to the simulation of the strip production process and the quality control of the strip [6, 7]. However, the finite element analysis software has high requirements for the user's ability, and it often requires level-by-level training to use it proficiently.

On the other hand, the growing mass of data has made data mining methods centered on machine learning and deep learning more attention [8]. And it is used in manufacturing production scheduling [9], equipment monitoring [10], quality control [11], and other aspects. The data mining methods provide an effective way to predict and control the quality of hot strip rolling. It can break the data island, deeply mine, and utilize the data value. Specifically, initially, through data mining, the correlation between process parameters and quality parameters is discovered from the massive production history data. Further, the strip quality is predicted through these correlations. Finally, combined with the computer control system, a closed loop is formed to the greatest extent to control the quality of the strip.

*2.2. Data Mining Techniques.* Data mining techniques can be divided into two parts: machine learning and deep learning. Kotkunde et al. used artificial neural networks (ANN) and support vector machines (SVM) to evaluate the thickness distribution of alloy sheets at various temperatures and blank diameters [12]. Li and Dai used the $k$-means algorithm to divide the production data into $k$ clusters and uses the BP neural network to predict the final strip rolling temperature to improve the prediction accuracy [13]. Wu et al. improved the ELM algorithm and created a two-hidden layer optimized ELM model, and they applied it to the prediction of bending force in the hot strip rolling process [14, 15].

The above studies are based on pure machine learning predictions, but machine learning cannot handle high-dimensional problems. Before using the machine learning method, the above research often needs to select data features to reduce the dimension of the input parameters [16].

However, for the high coupling strip quality prediction problem, too few features often cannot contain all the features of the data, which makes the prediction accuracy worse. The deep learning network has deeper network layers and more complex network structure compared with machine learning. For example, the deep belief network (DBN) superimposes RBM in front of the BP network. DBN has good feature extraction ability and shows good performance when processing high-dimensional input variables. It is widely used in manufacturing.

Liu et al. used DBN to process a large amount of real-time quality data collected by sensors and constructed a real-time quality monitoring and diagnosis plan for the manufacturing process [17]. Yang and Frangopol predict the remaining life cycle of ships based on DBN and then propose a ship life cycle management framework [18]. Zheng et al. combine DBN and SVM, use DBN to extract high-level features of signals, and use the SVM classifier for defect recognition, providing a new method for the nondestructive testing of bolt anchorage [19].

It can be concluded from a large number of studies that since deep belief networks were primarily used to classify problems at first, now it is mainly used for classification problems such as defect identification and quality classification in manufacturing quality problems and less often applied to regression problems such as quality parameter prediction. However, because the deep belief network has strong high-dimensional feature extraction capabilities and good model generalization, it can be improved to suit continuous value prediction problems on the basis of maintaining the feature extraction capabilities. For example, in existing research, DBN is combined with Particle Swarm Optimization (PSO) [20], Firefly Algorithm (FA) [21], Support Vector Machine (SVM) [22], Extreme Learning Machine (ELM) [23], and other algorithms to improve the prediction accuracy and model feasibility.

Considering the complexity of the DBN network structure, this paper chooses the combination of DBN and ELM to simplify the DBN training method and shorten the training time while improving the prediction accuracy.

## 3. Quality Prediction Model and Network Structure

A deep belief network is one of the core algorithms in deep learning. The deep belief network is composed of several restricted boltzmann machines (RBM) and a BP neural network, which can solve the high-dimensional and high-coupling problem well. However, DBN has problems such as unsuitable for continuous value and too long training time. In this paper, DBN is improved to make it more suitable for the quality prediction of the strip finishing process.

### 3.1. Deep Belief Network Model

*3.1.1. Basic Structure of DBN.* The deep belief network is composed of multiple series-connected RBMs and a BP neural network. It has a powerful feature learning ability. The structure of the deep belief network for strip steel quality prediction is shown in Figure 1.

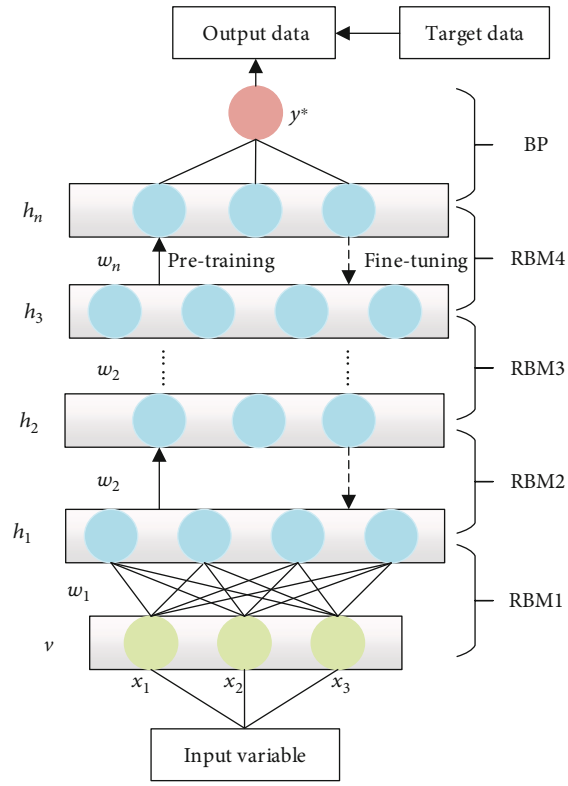


Figure 1: Deep belief network structure.

The first visible layer $V$ and the second hidden layer $h_1$ constitute RBM1. The hidden layer of RBM1 is also the visible layer of RBM2, forming RBM2 together with the third hidden layer, and so on for each layer, stacking to form multilayer RBMs. RBM in DBN uses unsupervised learning, mainly used for feature extraction; the BP network uses supervised learning, mainly used for regression and outputting the predicted value of quality parameters.

*3.1.2. DBN Training Process.* It can be seen from the figure that the training process of DBN is divided into two stages, namely, the forward pretraining stage and the reverse fine-tuning stage. DBN uses a greedy unsupervised learning mechanism to complete layer-by-layer forward training from bottom to top and extracts the abstract features of the bottom-level data as the high-level input, until the features are sent to the top-level regression unit. Then, it calculates the error between the regression result and the real result and uses the back propagation algorithm of the BP network to complete the reverse fine-tuning of the parameters, further reducing the model error and improving the training accuracy of the system.

DBN gives full play to and combines the advantages of RBM and BP neural network, uses multilayer RBM to extract and abstract high-dimensional data, retains important feature information as much as possible, uses the BP network to complete regression, and uses the BP algorithm to fine-tune the parameters of each layer, so as to achieve the optimal state.

*3.1.3. Shortcomings of DBN.* Although the traditional DBN has particularly good feature extraction capabilities, after analyzing the model, it can be known that the traditional DBN model also has the following shortcomings:

(a) The visible layer and hidden layer of traditional RBM obey the binary distribution and have a good function of extracting feature signals for discrete data. In the problem of strip quality prediction, the continuous input signals need to be digitized, which leads to the loss of information and reduces the accuracy of the model

(b) In the process of DBN training, an important parameter that needs to be adjusted is the number of neurons in each hidden layer, which directly affects the prediction accuracy and training time of the model. For the problem of strip quality prediction, the dimension of input data involved is relatively high, so it is more difficult to select the number of neurons

(c) Since the fine-tuning process of DBN is based on the gradient descent algorithm, the convergence speed of the BP network is relatively slow. In addition, the BP algorithm is a local search algorithm, which may cause the network to fall into a local optimum due to improper selection of the initial network weights, which may lead to network training failures

In order to solve the above problems, this paper introduces Gauss-Bernoulli RBM instead of RBM in traditional DBN to save the signal of continuous input data, introduces particle swarm optimization to calculate the optimal number of neurons in the hidden layer in the process of parameter adjustment, and introduces extreme learning machine to shorten the training time of the model, improve the generalization ability, and avoid falling into local optimization.

### 3.2. Gaussian-Bernoulli RBM (GBRBM)

*3.2.1. Basic Structure of GBRBM.* Restricted Boltzmann machine (RBM) is a shallow random generation network proposed by Hinton et al. It is an energy model for unsupervised learning. It divides all neurons into the visible layer and hidden layer. Data is input from the visible layer to express data features. The hidden layer can extract features to express the relationship between input variables, so the hidden layer is also called a feature extractor. The two layers of neurons are fully connected, and there is no connection between the neurons in the same layer.

Suppose $v_1 \sim v_m$ is the visible layer cell node, $h_1 \sim h_n$ is the hidden layer cell node, $a_1 \sim a_m$ is the visible layer node offset, $b_1 \sim b_n$ is the hidden layer node offset, and $w_{n\times m}$ is the weight matrix between the visible layer and the hidden layer.

When the state of $(v, h)$ is determined, the energy function of RBM can be defined as

$$E(v, h \mid \theta) = -a^T v - b^T h - v^T w_{n\times m} h. \tag{1}$$

The visible layer and hidden layer of the traditional RBM are limited by the binary distribution [24], which has a good performance when dealing with classification problems. But Boolean variables are no longer suitable for the calculation of continuous data when dealing with regression problems. Therefore, this paper introduces GBRBM when carrying out strip quality prediction.

Gaussian-Bernoulli RBM (GBRBM) is a restricted Boltzmann machine for nonbinomial data proposed by Krizhevsky and Hinton. GBRBM introduces Gaussian function between visible and hidden elements to process continuous numbers between 0 and 1. The energy function expression of GBRBM is as follows:

$$E(v, h|\theta) = \sum_{i=1}^{m} \frac{(v_i - a_i)^2}{2\sigma_i^2} - \sum_{j=1}^{n} b_j h_j - \sum_{i=1}^{m}\sum_{j=1}^{n} \frac{v_i}{\sigma_i} w_{ij} h_j. \tag{2}$$

The lower the energy of the system is, the more stable the system is and the smaller the error of quality parameter prediction results is. In equation (2), $\theta$ is the parameter to be solved, $\theta = (\mathrm{w}, a, b, \sigma)$, and $\sigma_i$ is the tolerance corresponding to $v_i$. When $\theta$ is determined, the joint probability distribution of $(v, h)$ can be obtained through the energy function:

$$P(v, h \mid \theta) = \frac{e^{-E(v,h|\theta)}}{Z(\theta)}. \tag{3}$$

In equation (3), $Z(\theta) = \sum_{v,h} e^{-E(v,h|\theta)}$ is the normalization factor, also called the distribution function.

Since there is no connection between neurons in the same layer of RBM, the activation states between the visible layer and the hidden layer unit are independent of each other, so when the $V$ and $H$ states are determined, the activation probability of the visible layer and the hidden layer unit can be obtained as

$$P(v_i = x \mid h) = \frac{1}{\sigma_i \sqrt{2\pi}} \exp\left( - \frac{\left( x - a_i - \sum_{j=1}^{n} w_{ij} h_j \right)^2}{2{\sigma_i}^2} \right), \tag{4}$$

$$P\left(h_j = 1 \mid v\right) = \mathrm{sigmoid}\left( a_i + \sum_{i=1}^{m} \frac{v_i}{\sigma_i} w_{ij} \right). \tag{5}$$

*3.2.2. GBRBM Training Process.* The purpose of RBM model training is to calculate the optimal value of parameter $\theta = (w, a, b, \sigma)$, so as to obtain the optimal model. Usually, it can be achieved through the maximum likelihood estimation formula:

$$\ln L(\theta \mid v) = \ln \left( \frac{1}{Z(\theta)} \sum_{h} e^{-E(v,h|\theta)} \right). \tag{6}$$

In order to calculate the updated equation of each parameter, we use the contrast divergence (CD) algorithm proposed by Hinton to train the model and add the adjustment

of $\sigma_i$ in GBRBM; the training process is as follows: (a) at the beginning of training, assign the input data to the nodes of the visible layer to obtain $v_i$ and obtain the data features mapped from the visible layer $V$ to the hidden layer $H$ according to equation (5), (b) calculate reversely according to equation (4) and map the output obtained in (a) to the visible layer $V$, and (c) calculate the error between the samples according to the comparison between the reconstructed results and the original data and adjust the interlayer weight $W$ to reduce the error. The updating process of parameter vector $\theta = \{w, a, b, \sigma\}$ is as follows:

$$\begin{cases} \Delta w_{ij} = \gamma\left(\left\langle v_i h_j\right\rangle_{\text{data}} - \left\langle v_i h_j\right\rangle_{\text{recon}}\right), \\ \Delta a_i = \gamma\left(\left\langle v_i\right\rangle_{\text{data}} - \left\langle v_i\right\rangle_{\text{recon}}\right), \\ \Delta b_j = \gamma\left(\left\langle h_j\right\rangle_{\text{data}} - \left\langle h_j\right\rangle_{\text{recon}}\right), \\ \Delta \sigma_i = \gamma\left(\left\langle \sigma_i\right\rangle_{\text{data}} - \left\langle \sigma_i\right\rangle_{\text{recon}}\right). \end{cases} \tag{7}$$

In equation (7), $\gamma$ is the RBM learning rate, $\langle\cdot\rangle_{\text{data}}$ is the mathematical expectation of the input data, and $\langle\cdot\rangle_{\text{recon}}$ is the mathematical expectation of the reconstructed data. The output of the trained model forward passing can represent the original input of the visible layer; thus, the feature extraction of the input data is completed.

*3.3. Extreme Learning Machine.* The BP neural network is used in the upper layer of DBN. Although the BP neural network has better adaptive ability, it adopts the gradient descent algorithm in the training process. When the neuron is close to 0 or 1, the convergence speed is relatively slow, resulting in a longer training time for the model. Moreover, the BP algorithm may fall into a local optimum for complex nonlinear problems such as strip quality prediction. In order to solve these problems, this paper introduces the extreme learning machine model.

Extreme learning machine (ELM) is a single hidden layer feedforward neural network proposed by Huang Guangbin in 2004, including the input layer, hidden layer, and output layer. The structure is shown in Figure 2. The offset of the hidden layer node and the weight of the input layer in ELM are randomly assigned during initialization, which greatly shortens the training time of the model. The output weight of ELM is adjusted by the regularized minimum mean square error, which can ensure the global optimization ability of ELM. Therefore, ELM has relatively high learning efficiency and strong generalization ability and is more suitable for complex production scenarios such as the steel finishing rolling process.

Suppose there are $M$ sample $(X_i, y_i)$, $X_i = [x_{i1}, x_{i2}, \cdots, x_{\text{in}}]^T \in R^n$ and $y_i = [y_{i1}, y_{i2}, \cdots, y_{im}]^T \in R^m$ are the input samples and their corresponding expected output, respectively. Assuming that the number of hidden layer nodes is $L$, the ELM model can be expressed as

$$\sum_{i=1}^{L} \beta_i g\left(w_i \cdot x_j + b_i\right) = o_j, \quad j = 1, \cdots, M. \tag{8}$$

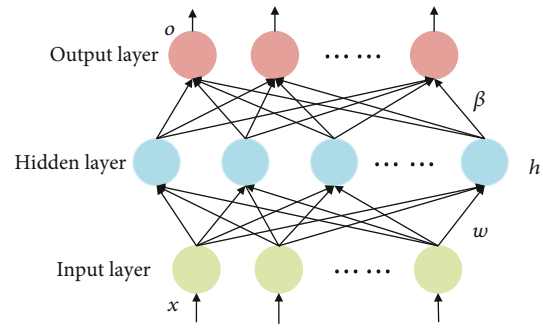


Figure 2: Structure of ELM.

In equation (8), $g(x)$ is the activation function of the hidden layer; $w_i$ and $\beta_i$ are the weight vectors between the input layer and hidden layer and between the hidden layer and output layer, respectively; $b_i$ is the offset of the hidden layer node; and $o_j$ is the output of ELM. The purpose of network training is to minimize the output error and find a special $w_i, \beta_i, b_i$ so that the output value is the target value:

$$\sum_{i=1}^{L} \beta_i g\left(w_i \cdot x_j + b_i\right) = y_j, \quad j = 1, 2, \cdots, M. \tag{9}$$

Expressed as a matrix:

$$H\beta = Y, \tag{10}$$

$$H = \begin{bmatrix} g(w_1 \cdot x_1 + b_1) & \cdots & g(w_L \cdot x_1 + b_L) \\ \vdots & \ddots & \vdots \\ g(w_1 \cdot x_M + b_1) & \cdots & g(w_L \cdot x_M + b_L) \end{bmatrix}. \tag{11}$$

In equation (10), $h$ is the hidden layer output matrix, $\beta$ is the weight matrix, and $Y$ is the network output matrix. Since ELM randomly generates $w_i$ and $b_i$ in the initialization stage, the matrix $H$ is uniquely determined. The training process of the network can be transformed into a linear system solving the problem. The approximate solution of $\beta$ can be obtained according to the Moore-Penrose generalized inverse matrix:

$$\beta^* = H^+ Y. \tag{12}$$

In equation (12), $H^+$ is the Moore-Penrose generalized inverse of the hidden layer output matrix $H$.

*3.4. GBDBN-ELM Model.* In this article, the RBM in the traditional DBN is replaced with GBRBM to form GBDBN, and then, the GBDBN model and the ELM model are combined, as shown in Figure 3. For an $N$-layer GBDBN-ELM model, the strip quality sample data is assigned to the visible layer $V$ of the first layer of GBRBM, the first hidden layer $h_1$ and the second hidden layer $h_2$ form GBRBM, the output of the former GBRBM is also the input of the latter GBRBM, and so on, until the $N-2$ layer of the model; the $N-2$ layer, $N-1$ layer, and the last output layer are the ELM. The

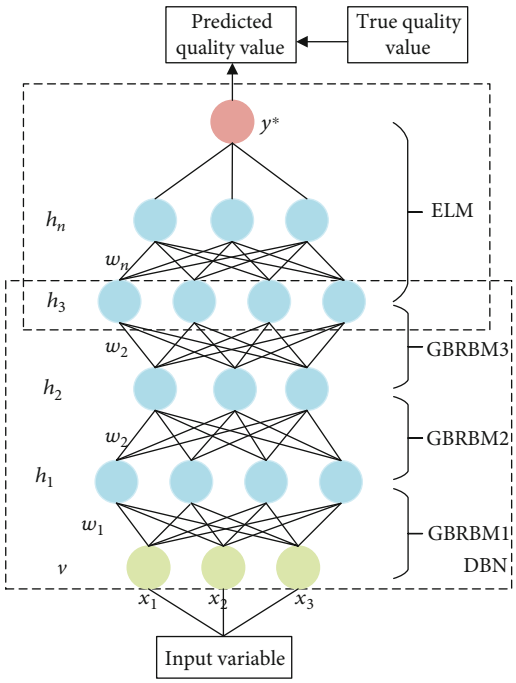


Figure 3: GBDBN-ELM network structure for strip quality prediction.

$N-2$ layer of the model is both the output of the last layer of GBRBM and the input of ELM.

In this model, the strip quality input data is extracted by multilayer GBRBM to form a low-dimensional feature expression, which ensures the features of the original input data set as much as possible. Then, input the extracted features into ELM for regression prediction to obtain the predicted strip quality prediction data.

For an $N$-layer GBDBN-ELM model, suppose the number of neurons in the $N-1$ layer network is $n$, and the number of neurons in the $N-2$ layer network is $m$, the network can be expressed as

$$\sum_{i=1}^{m} \beta_i g(w_i \cdot h_{N-2} + b_i) = o_j, \quad j = 1, \cdots, n. \tag{13}$$

According to the ELM algorithm, the output matrix of the $N-1$ layer of the network and the solving equation of $\beta$ can be obtained as

$$H_{N-1} = \begin{bmatrix} g(w_1 \cdot h_{N-2,1} + b_1) & \cdots & g(w_L \cdot h_{N-2,1} + b_L) \\ \vdots & \ddots & \vdots \\ g(w_1 \cdot h_{N-2,n} + b_1) & \cdots & g(w_L \cdot h_{N-2,n} + b_L) \end{bmatrix}, \tag{14}$$

$$\beta^* = {H_{N-1}}^+ Y. \tag{15}$$

The GBDBN-ELM model combines the unsupervised learning characteristics of DBN with high learning efficiency and strong generalization ability of ELM. It can improve the training speed and prediction accuracy.

## 4. Experimental Study

The indexes to measure the quality of strip steel mainly include the thickness, width, and surface temperature, among which the thickness is the most important index to evaluate whether the steel is up to the standard [25]. Therefore, this paper verifies the feasibility of the improved deep confidence network by predicting the thickness of the finished rolled strip and compares the improved model with other machine learning algorithms and deep learning algorithms to illustrate the superiority of the model.

### 4.1. Data Preparation

*4.1.1. Data Source.* The experimental data in this paper comes from a 1580 mm hot strip finishing line of a steel company. The production line consists of 7 units. After 5~7 passes of rough rolling, we can get intermediate billet of 25~60 mm thick, which can be sent to the finishing mill after the hot coil box, flying shear, and dephosphorization box. The control of strip thickness is mainly in the finishing mill. After the finishing mill, we can obtain the finished strip with thickness of 1.2-12.7 mm. The production line consists of seven finishing mills, namely, F1~F7. A work roll bending device is adopted on 7 rolling mills, among which F2~F4 are PC rolling mills with crossed rolls in pairs. Looper rolls are installed between each two rolling mills to balance the rolling tension and prevent plate stacking. The threading speed, acceleration, reduction of each stand, and bending force of each stand of the F1~F7 rolling mill are calculated and set by a computer control system according to the variety and specification of rolled strip and can be adjusted dynamically. The exit of the F7 finishing mill is equipped with rolling line detection instruments for thickness, width, temperature, and crown of strip steel quality, which can monitor the quality in real time and modify the process parameters to improve the quality of rolled products.

In this experiment, the process parameters set by the computer control system of the seven finishing mills in the finishing rolling stage and the strip quality parameters detected by the sensor at the F7 exit are collected within 8 days. The sampling time interval is 90 seconds, and a total of 3350 sets of production data are collected. Each set of data includes 7 sets of finishing mills' reduction position, rolling force, stand speed, oil film compensation, eccentric compensation, and other process parameters, as well as their confidence and number of points, totaling 234 columns of data.

*4.1.2. Data Preprocessing.* As there are 234 process parameters collected, if all these data are used to predict the strip thickness, the deep learning network will be very complex and the training time will be very long. However, some of the data are not highly correlated with the final strip exit thickness. In this paper, the importance of each element is sorted by the gradient boosting decision tree method, as shown in Figure 4. Finally, 69 factors are selected as the input parameters for strip quality prediction, including entrance thickness, exit temperature, roll gap of each stand, rolling force, stand speed, roll bending force, back tension, and looper angle.

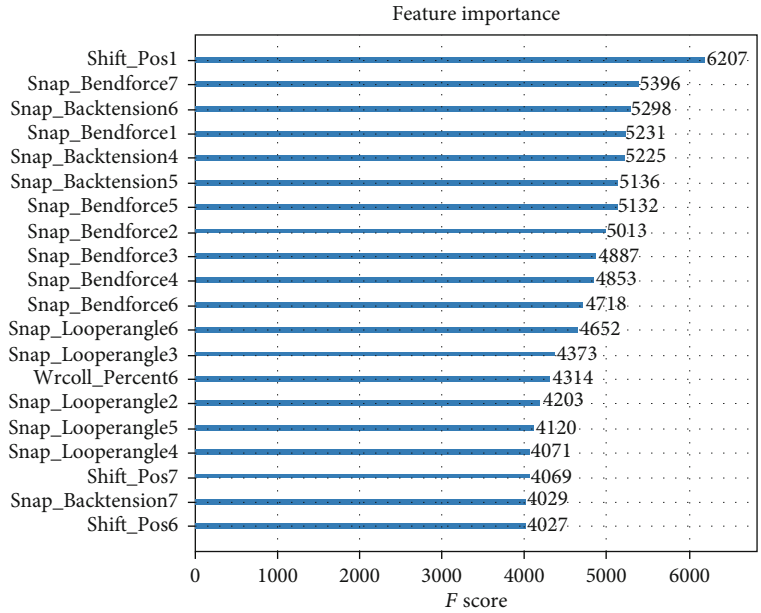


Figure 4: The importance of each element to the thickness of the strip (the first 20).

Due to the complex production environment, water vapor, and other interference factors, and the instability of the computer system and sensor itself, the data collected on-site has certain errors, missing data, and abnormal values. For the problem of missing data, this paper uses the mean method to supplement the missing value. For outliers, first, calculate the Euclidean distance between samples by the $k$ -means clustering method and extract outliers, and then, eliminate the outliers. The min–max normalization method is used to carry out linear transformation on the original data, and the data is mapped between $[0, 1]$, so as to eliminate the influence of parameter dimension on the prediction results.

According to the holdout verification method, 3000 groups of data are randomly selected as the training set, and the remaining 350 groups of data are used as the verification set of the model after training.

### 4.2. Parameter Setting

*4.2.1. Key Parameter.* Before training and prediction, some relevant parameters need to be set in advance. These parameters cannot be updated in the training process but given in advance through the parameter setting method. These parameters have a great impact on the learning ability of the model and need to be adjusted continuously to maximize the advantages of the model.

By analyzing the structure and principle of the network model, the superparameters of the GBRBM-ELM model need to be set in advance, including the number of GBRBM layers in DBN, the number of hidden layer nodes in DBN and ELM, the number of visible layer nodes in the first RBM layer, the number of ELM output layer nodes, the size of data blocks in the network training phase, the number of training rounds, the learning rate and momentum term.

Since 69 input parameters are selected to predict the strip thickness, the number of visible layer nodes is 69 and the number of output layer nodes is 1. This paper uses different methods to set and tune different parameters.

*4.2.2. Grid Search Method.* Grid search is to use prior knowledge to specify the value range of parameters. In this range, the parameters are listed hierarchically. Based on the experimental results, the optimal parameter value with a small prediction error can be selected.

Taking GBRBM layers as an example, it is one of the important parameters of the DBN network structure. The number of RBM layers directly affects the prediction effect of the model. When the number of RBM layers is too small, the model will not be able to take advantage of deep learning, and the prediction effect will be poor. But too many layers will lead to the training time process or cause overfitting. According to prior knowledge, the change range of the number of layers is set to be between 1 and 10. The prediction effect of the model is shown in Figure 5.

According to the comparison results, when the number of RBM layers is 4, the model error is the smallest, so this paper uses a 4-layer RBM network structure.

Using the same method, after multiple comparison experiments, the number of hidden layer nodes in ELM, data block size, training rounds, learning rate, and momentum can be obtained. The optimal parameters of the network are shown in Table 1.

*4.2.3. Particle Swarm Optimization.* Another main parameter of the DBN model structure is the number of nodes in each hidden layer. Because the hidden layers in the 4-layer RBM are related to each other, the number of nodes varies widely, and there are many node combinations; it is difficult to use grid search to enumerate one by one to find the optimal

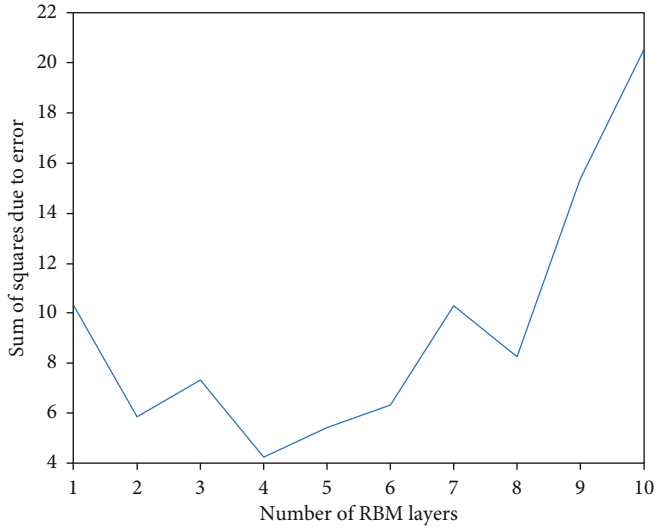


Figure 5: Variation of residual sum of squares with RBM layers.

Table 1: Parameters of GBDBN-ELM model.

| | |
|---|---|
| Number of RBM layers | 4 |
| Number of hidden layer nodes in ELM | 60 |
| Data block size | 150 |
| Training rounds | 20 |
| Learning rate | 0.01 |
| Momentum | 0.5 |

combination of the number of nodes. In this paper, particle swarm optimization (PSO) is used to automatically calculate the number of hidden layer nodes in each layer.

The particle swarm algorithm compares the optimized solution of each objective function to the particles in the search space. Each particle has two parameters, position and velocity, and the fitness of the particle can be calculated from the objective function. By comparing the fitness of the particle at the current time with that at the previous time, the individual optimal position $p_{id}$ can be obtained. Similarly, the group optimal position $g_d$ can be obtained. According to equation (14), the velocity and position of the particle can be updated, and the global optimal solution satisfying the termination condition can be found:

$$v_{id}(t+1) = wv_{id} + c_1 r_1 (p_{id} - x_{id}(t)) + c_2 r_2 (g_d - x_{id}(t)), \tag{16}$$

$$x_{id}(t+1) = x_{id}(t) + v_{id}(t+1). \tag{17}$$

In equations (16) and (17), $v_{id}(t)$ and $x_{id}(t)$ are the velocity and position of particles at time $t$, $c_1$ and $c_2$ are the learning factors, and $r_1$ and $r_2$ are random numbers in (0,1).

Set the population size of PSO as 10 and the number of alternations as 10, and finally, find the number of hidden layer nodes of 4-layer DBN as [63, 54, 46, 35].

*4.3. Model Training.* The training of the GBDBN-ELM combined model is divided into two parts:

(a) *GBDBN Module Training.* First, initialize the network parameters, weights, and the number of hidden layer nodes of the model. The first $N-2$ layers of the combined model are the GBDBN model, and the preprocessed input data is allocated to the visible layer nodes to establish $v_i$. Next, the contrast divergence (CD) algorithm is used to train each RBM layer by layer from bottom to top. When one RBM layer is trained, the parameters of the layer are fixed and used as the input of the upper RBM to train the upper RBM, and so on, until all RBM training is completed. Finally, the bottom features are gradually gathered into the high-level features and finally sent to the regression unit.

(b) *ELM Module Training.* The connection weights of the $n-1$ layer and $n-2$ layer are initialized. The $N-2$ layer is the feature extraction layer of the last layer of GBDBN. The preprocessed high-dimensional labeled data is used as the input of the GBDBN module after training, and the feature extraction result is used as the input of the initial elm module. The elm algorithm is used for training to obtain better model parameters.

Based on GBDBN-ELM module training, effective DBN and ELM are obtained, respectively. The test data set is preprocessed to obtain high-dimensional sample data to be detected. The trained GBDBN model is used for feature extraction to obtain better feature data. The predicted strip thickness can be obtained by the ELM module. The overall process is shown in Figure 6.

*4.4. Result Analysis and Comparison*

*4.4.1. Model Evaluation Index.* In this paper, five indexes are used to evaluate the prediction effect of the model, including

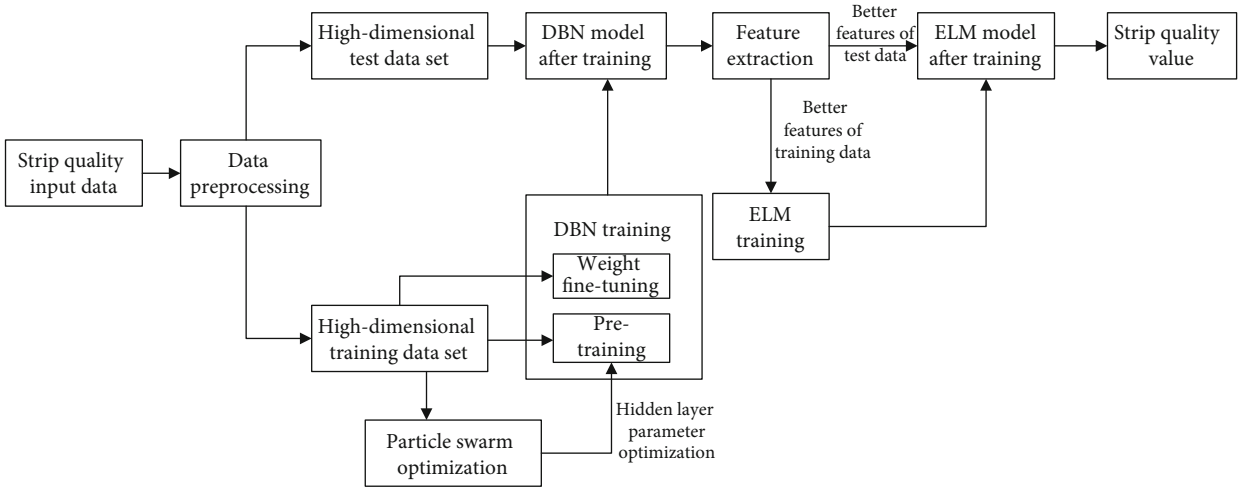


Figure 6: Strip steel quality prediction process based on GBDBN-ELM.

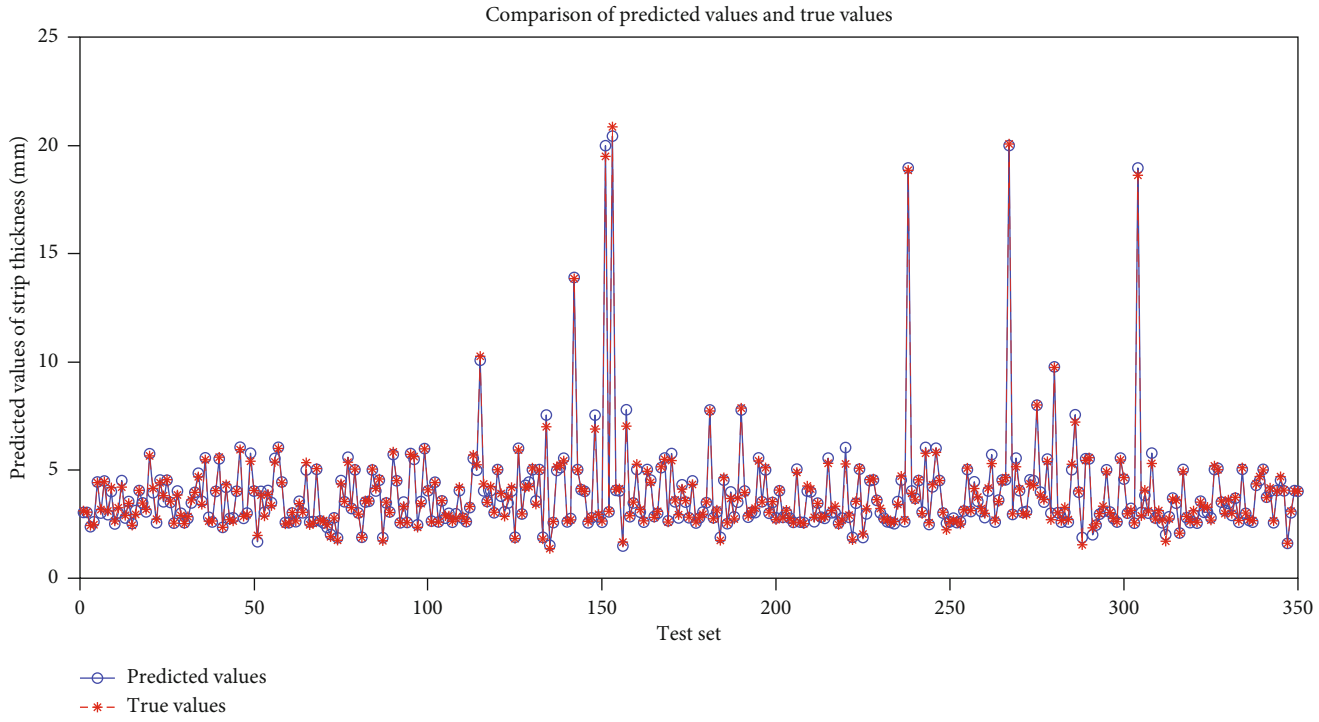


Figure 7: The curve of the predicted value and the true value of the strip thickness.

the sum of squares of residuals (SSR), root mean square error (RMSE), $R$ square coefficient of determination ($R^2$), and training time ($T$). The index is calculated as follows:

$$\begin{cases} \text{SSE} = \sum_{i=1}^{N} (y_i^* - y_i)^2, \\ \text{RMSE} = \sqrt{\frac{1}{n}\sum_{i=1}^{N} (y_i^* - y_i)^2}, \\ R^2 = 1 - \frac{\sum_{i=1}^{N} (y_i^* - \overline{y_i})^2}{\sum_{i=1}^{N} (y_i - \overline{y_i})^2}. \end{cases} \tag{18}$$

The smaller SSE, RMSE, and MAE, the better the prediction effect. $R^2$ is the fitting degree of the model, and the closer $R^2$ is to 1, the better the regression effect of the model is; $T$ is the time from the beginning to the end of training, and the smaller $t$ is, the faster the model training is and the better the model performance is.

*4.4.2. Prediction Results.* 350 sets of data were used in the test set to evaluate the performance of the model. In this paper, the simulation results of the prediction model are assessed by analyzing the curve of the predicted value and the true value of the strip thickness, the curve of the prediction error, and the curve of the prediction relative error.

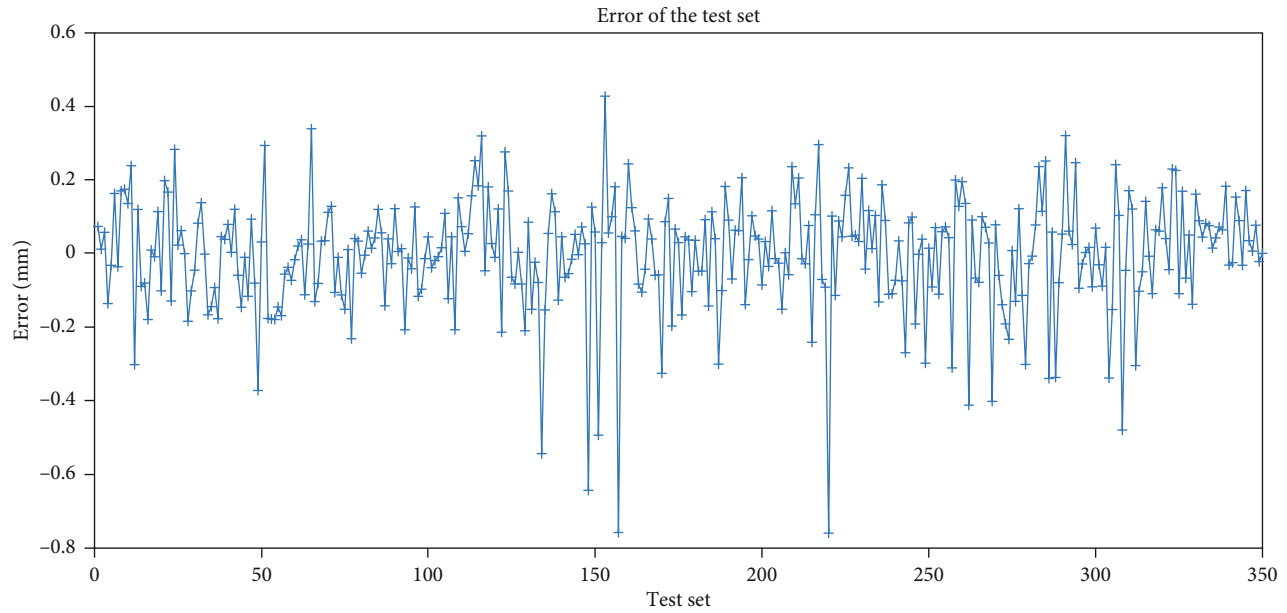


Figure 8: The curve of the prediction error.

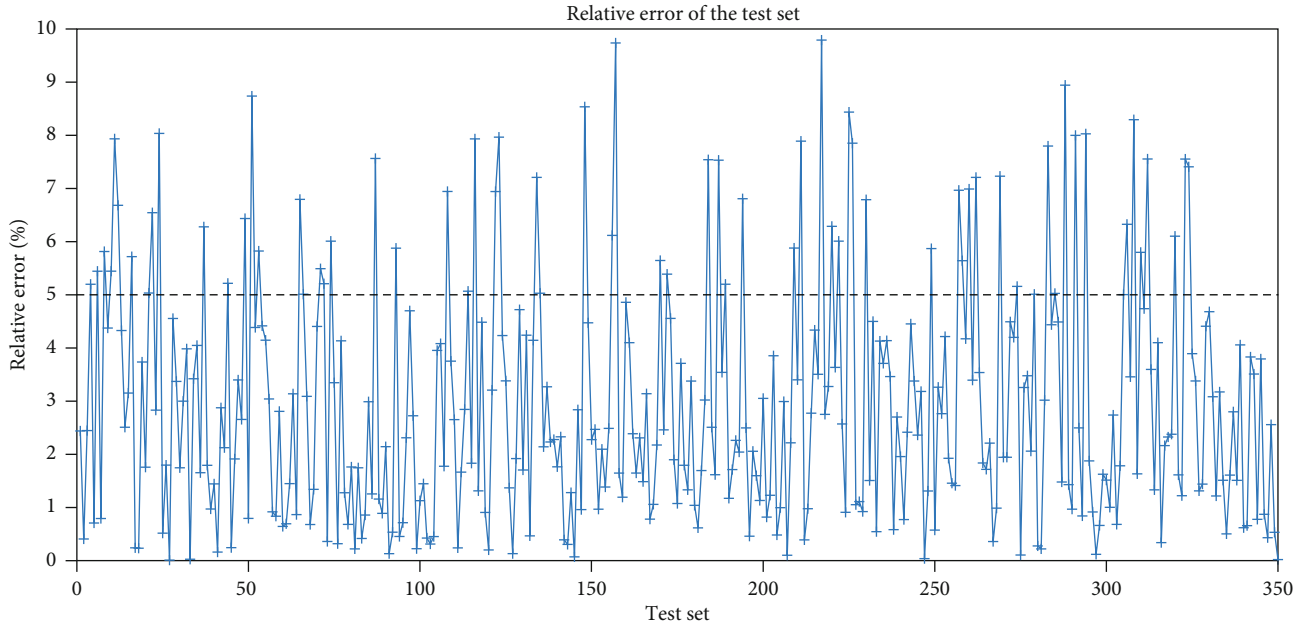


Figure 9: The curve of the prediction relative error.

Table 2: Comparison of prediction results of different models.

| Index\model | BP | ELM | DBN | DBN-ELM | GBDBN-ELM |
|---|---|---|---|---|---|
| SSR | 59.3560 | 78.2718 | 14.3091 | 22.398 | 8.5856 |
| RMSE | 0.4118 | 0.4728 | 0.2022 | 0.2530 | 0.1565 |
| $R^2$ | 0.9872 | 0.9607 | 0.9926 | 0.98854 | 0.9956 |
| $T$ | 3.1548 | 0.5127 | 96.9802 | 32.0120 | 33.8380 |

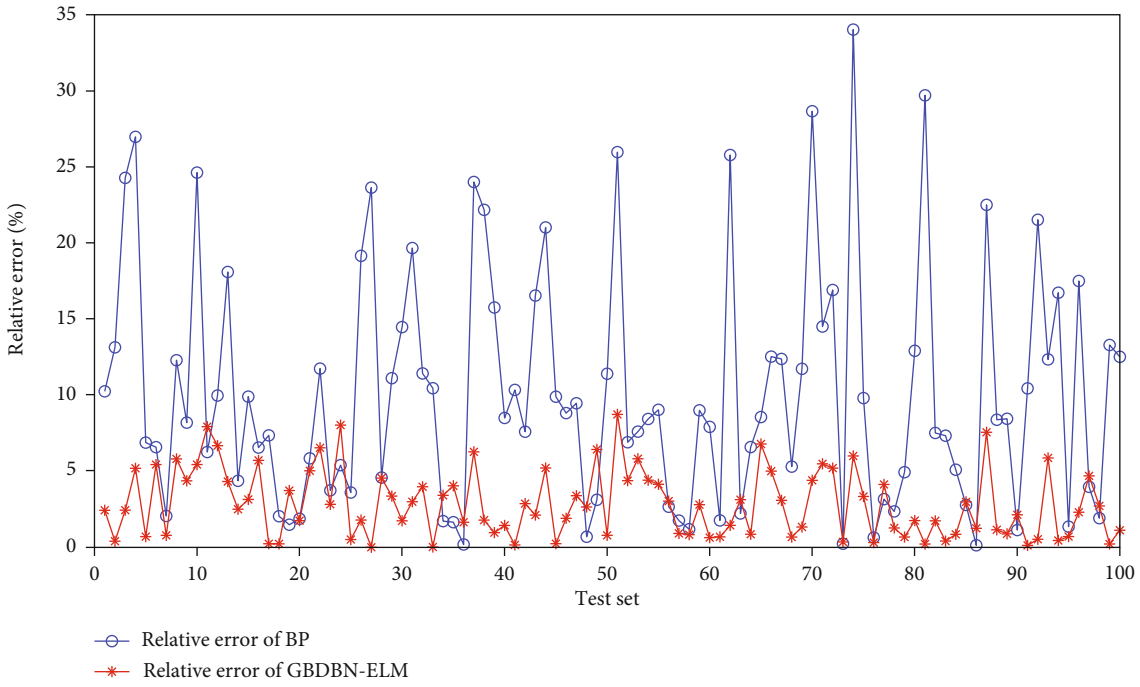


Figure 10: Comparison of relative errors of BP and GBDBN-ELM (part).

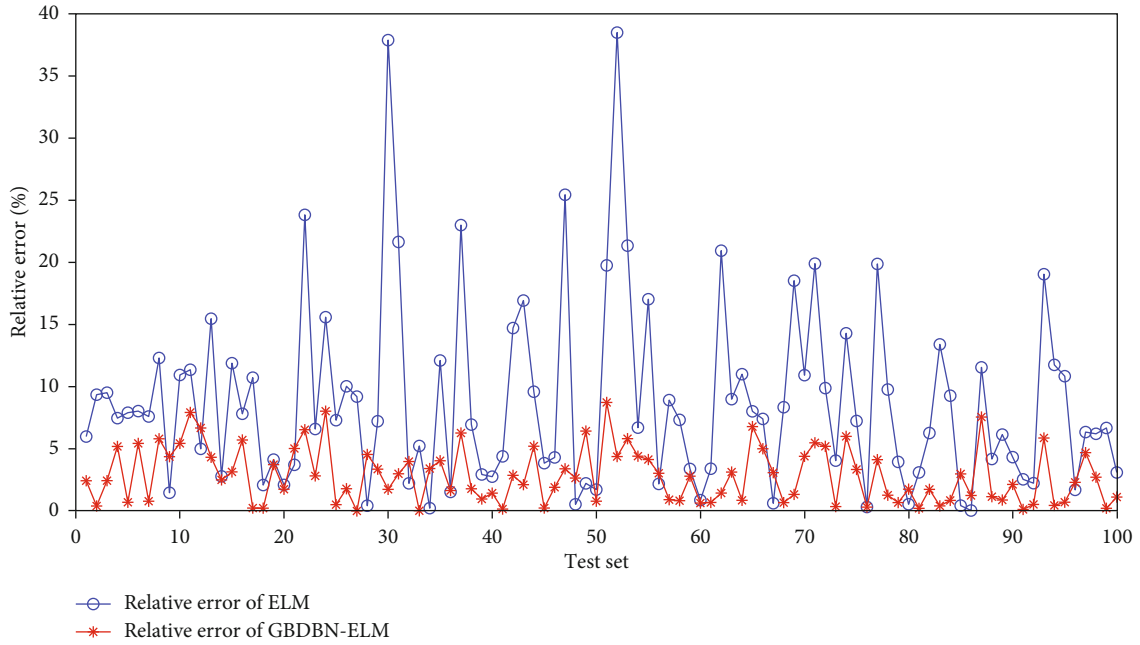


Figure 11: Comparison of relative errors of ELM and GBDBN-ELM (part).

It can be seen from Figure 7 that the predicted value of strip thickness obtained by the GBDBN-ELM model is very close to the real value of strip thickness, and the fluctuation trend and variation range of them are basically consistent. By analyzing Figure 8, we can get the following results: 93.7% of the absolute error between the predicted value and the real value is between $[-0.3, 0.3]$, and only a few points have relatively large error between $[-0.4, 0.8]$. The reason is that the test samples are randomly selected, and these points have large mutation compared with the surrounding points, and the change range of the model prediction is less than the real change range. As shown in Figure 9, the relative error of strip thickness predicted by the model is within 10%, among which 80.9% is less than 5%. In conclusion, the prediction model of strip thickness based on GBDBN-ELM has high accuracy.

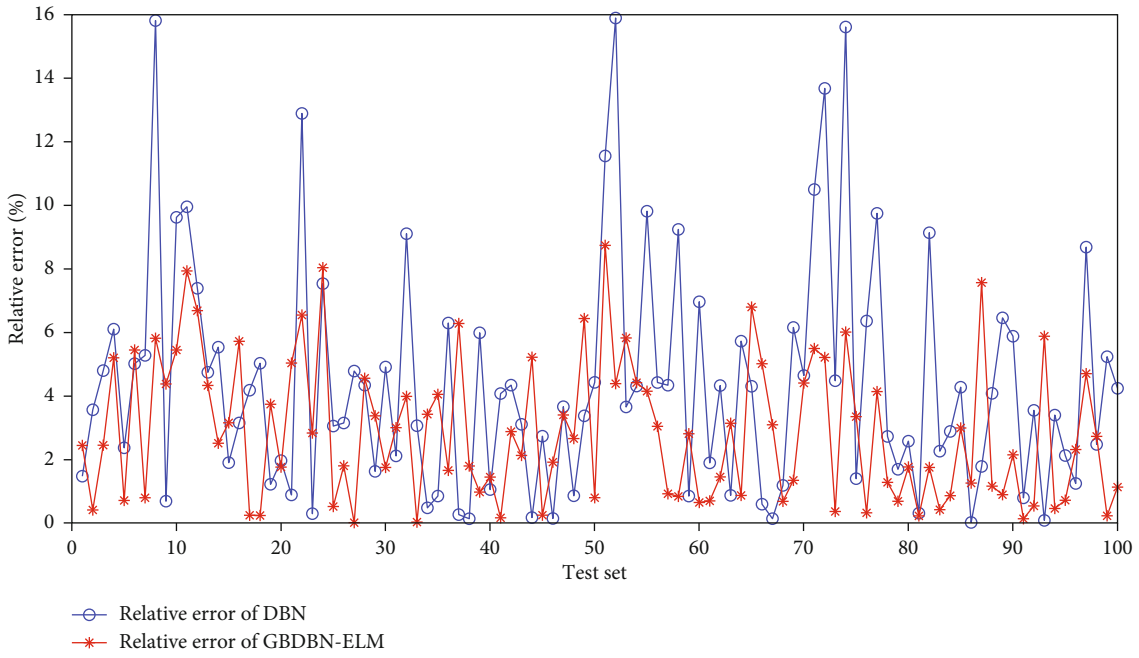


Figure 12: Comparison of relative errors of DBN and GBDBN-ELM (part).

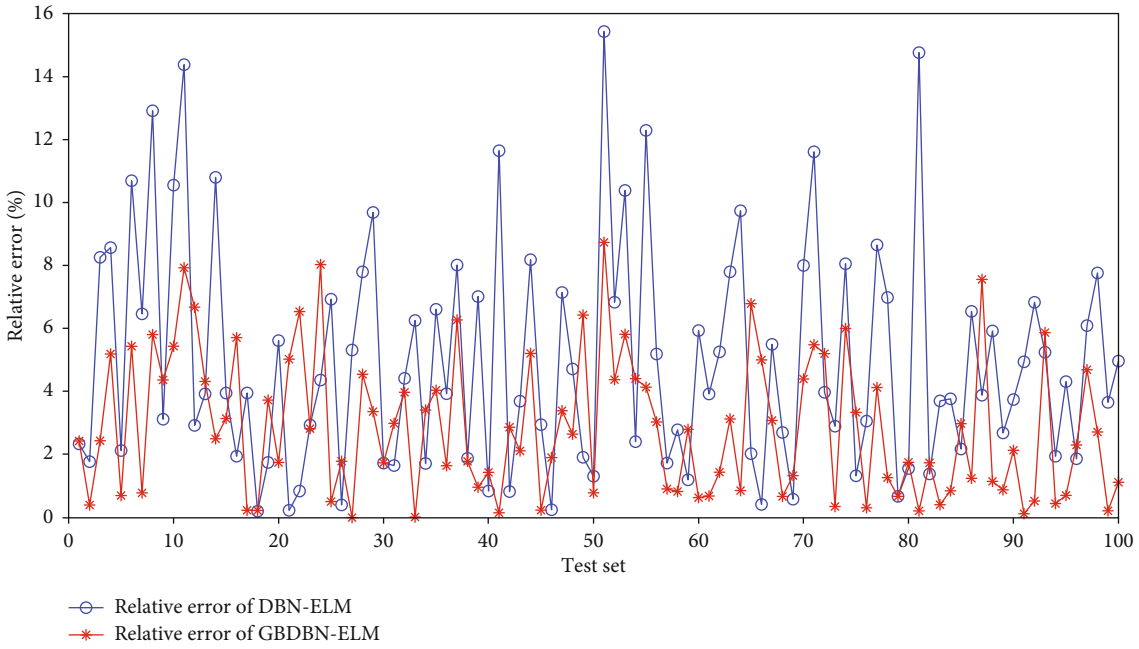


Figure 13: Comparison of relative errors of DBN-ELM and GBDBN-ELM (part).

*4.4.3. Comparison of Different Models.* In order to comprehensively analyze the prediction performance of the model for strip steel quality, this paper compares it with the BP neural network, ELM, traditional DBN network, and DBN-ELM model and evaluates the above models according to SSR, RMSE, and $R^2$. The results are shown in Table 2. In order to intuitively compare the prediction error of the model, Figures 10–13 show the relative error of the prediction results of the first 100 groups of test data of GBDBN-ELM and show the comparison with other models, respectively.

Comparing the prediction results of the BP neural network and ELM in Table 2, we can find that the training time of ELM is shorter, since it generates hidden layer offset and input layer weights randomly during initialization, and there is no need to update them during training. However, the BP neural network can adjust the model to a better state during training, so its prediction accuracy is higher than that of ELM. However, by analyzing Figures 10 and 11, it can be found that a large part of the error of the two neural network prediction results is greater than 10%,

so it is not enough to use simple machine learning for strip quality prediction.

It can be seen from Table 2 that although DBN-ELM significantly shortens the training time, the prediction accuracy is slightly lower than DBN. GBDBN-ELM improves the RBM network on the basis of DBN-ELM to make it suitable for the continuous value regression problem and can retain more data features when predicting strip thickness. Therefore, GBDBN-ELM combines the advantages of DBN and ELM.

By comparing the results in Table 2, it is found that compared with DBN, GBDBN-ELM reduces the training time by 65.1%, the sum of squares error by 39.9%, and the root mean square error by 22.6%; compared with DBN-ELM, GBDBN-ELM reduces the sum of square error by 61.7% and the root mean square error by 38.1%, and the training time only increases by one second, which indicates that the improved model can effectively improve the accuracy and shorten the training time.

From Figures 12 and 13, we can see the prediction effect of the three deep learning models for each test data more intuitively. It can be seen that the overall relative error of the prediction results of GBDBN-ELM is smaller than that of DBN and DBN-ELM. The relative error of GBDBN-ELM hardly exceeds 8%, and it is certain that the prediction accuracy of the improved model meets industry requirements. In 350 sets of test data, the error of GBDBN-ELM's prediction results is 63.7% less than DBN, and 65.7% less than DBN-ELM. The average relative error is reduced, respectively, by 40.4% and 32.6%.

Especially for data with large prediction errors of DBN and DBN-ELM, GBDBN-ELM can significantly reduce the error and achieve better prediction results. The advantages of the improved model are also reflected here to a large extent.

The analysis of Table 2 and Figures 10–13 shows that the improved GBDBN-ELM model can improve the prediction accuracy and shorten the training time to a large extent.

## 5. Conclusion

This paper proposes an improved DBN strip quality prediction method to solve the problem that the strip quality prediction accuracy is not high because there are many sensors involved in the strip production process, and most of the process parameters are coupled with each other and have serious nonlinearity. In this paper, the RBM in DBN is changed into GBRBM to eliminate the dependence on binary distribution, extract the features of high-dimensional and high coupling input data, combine GBDBN with ELM, replace the BP network in DBN with ELM, and input the extracted data features into ELM for strip quality prediction. The GBDBN-ELM model is verified by the data of the steel finishing line and used to predict the strip thickness. We can draw the following conclusions.

The simple BP neural network and ELM model cannot deal with the high dimension and high coupling nonlinear data produced by the complex production process. Due to the simple network structure, they cannot fully extract the data features and mine the knowledge contained in the data, resulting in the accuracy of strip thickness prediction being not enough.

The GBDBN model proposed in this paper can solve the problem of low prediction accuracy caused by complex input data. The GBDBN network can retain as many abstract features of input data as possible, so that ELM can obtain higher prediction accuracy.

Through the comparison with the DBN network, it can also be known that using the ELM algorithm for GBDBN network training and prediction calculations can greatly shorten the time and solve the problem of excessive training time caused by the complexity of the DBN network.

## Data Availability

The raw/processed data required to reproduce the experiments in this article cannot be shared due to corporate confidentiality.

## Conflicts of Interest

The authors declare that there is no conflict of interest.

## Acknowledgments

This work was supported by the National Science and Technology Innovation 2030 of China Next-Generation Artificial Intelligence Major Project, Data-Driven Tripartite Collaborative Decision-Making and Optimization, under Grant 2018AAA0101801.

## References

[1] C. Klinkenberg, B. Kintscher, K. Hoen, and M. Reifferscheid, "More than 25 years of experience in thin slab casting and rolling current state of the art and future developments," *Steel Research International*, vol. 88, no. 10, article 1700272, 2017.

[2] Q. K. Pan, Q. D. Chen, T. Meng, B. Wang, and L. Gao, "A mathematical model and two-stage heuristic for hot rolling scheduling in compact strip production," *Applied Mathematical Modelling*, vol. 48, pp. 516–533, 2017.

[3] D. H. Zhang, W. Peng, J. Sun, J. G. Ding, and X. Li, "Key intelligent technologies of steel strip rolling process," *Journal of Iron and Steel Research*, vol. 31, no. 2, pp. 174–179, 2019.

[4] J. Y. Chen, P. H. Hao, J. P. Song, and H. J. Guo, "Study on temperature prediction model of cold rolling strip," in *International Conference on Artificial Intelligence and Big Data (ICAIBD)*, pp. 214–217, Chengdu, China, May2018.

[5] C. Yao, A. He, J. Shao, and J. Zhao, "A real-time quasi-3D metal flow model for hot strip rolling," *International Journal of Mechanical Sciences*, vol. 159, pp. 91–102, 2019.

[6] S. Ganguly, X. Wang, K. Chandrashekhara, M. F. Buchely, and S. Lekakh, "Modeling and simulation of void closure during steckel mill rolling for steel plate," *Steel Research International*, vol. 92, no. 2, article 2000293, 2020.

[7] C. Yao, A. He, J. Shao et al., "Finite difference modeling of the interstand evolutions of profile and residual stress during hot strip rolling," *Metals*, vol. 10, no. 11, article 1417, 2020.

[8] A. Dogan and D. Birant, "Machine learning and data mining in manufacturing," *Expert Systems With Applications*, vol. 166, article 114060, 2021.

[9] B. Waschneck, A. Reichstaller, L. Belzner, T. Altenmuller, and T. Bauernhansl, "Deep reinforcement learning for semiconductor production scheduling," in *Annual SEMI Advanced Semiconductor Manufacturing Conference (ASMC)*, pp. 301–306, Saratoga Springs, NY, 2018.

[10] M. Azamfa, X. Li, and J. Lee, "Deep learning-based domain adaptation method for fault diagnosis in semiconductor manufacturing," *IEEE Transactions on Semiconductor Manufacturing*, vol. 33, no. 3, pp. 445–453, 2020.

[11] C. B. Lemos, P. C. M. A. Farias, E. E. Simas, and A. G. S. Conceicao, "Convolutional Neural Network Based Object Detection for Additive Manufacturing," in *International Conference on Advanced Robotics (ICAR)*, pp. 420–425, Belo Horizonte, Brazil, Dec 2019.

[12] N. Kotkunde, A. Balu, A. K. Gupta, and S. K. Singh, "Development of predictive models for formability study of Ti-6Al-4V alloy at elevated temperatures," *Materials Today-Proceedings*, vol. 4, no. 2, pp. 937–945, 2017.

[13] X. Li and Y. R. Dai, "Prediction model of hot rolled strip quality based on K-means clustering and neural network," in *11th International Symposium on Computational Intelligence and Design (ISCID)*, vol. 2, pp. 150–153, Hangzhou, China, 2018.

[14] Y. Wu, H. C. Ni, X. Li, F. Luan, and Y. D. He, "Prediction of bending force in the hot strip rolling process using multilayer extreme learning machine," *Mathematical Problems in Engineering*, vol. 2021, Article ID 6682660, 13 pages, 2021.

[15] Z. Xu, D. D. Ye, J. J. Chen, and H. T. Zhou, "Novel terahertz nondestructive method for measuring the thickness of thin oxide scale using different hybrid machine learning models," *Coatings*, vol. 10, no. 9, p. 805, 2020.

[16] A. Singh and A. Tiwari, "A study of feature selection and dimensionality reduction methods for classification-based phishing detection system," *International Journal of Information Retrieval Research*, vol. 11, no. 1, pp. 1–35, 2021.

[17] Y. M. Liu, H. F. Zhou, F. Tsung, and S. Zhang, "Real-time quality monitoring and diagnosis for manufacturing process profiles based on deep belief networks," *Computers & Industrial Engineering*, vol. 136, pp. 494–503, 2019.

[18] D. Y. Yang and D. M. Frangopol, "Evidence-based framework for real-time life-cycle management of fatigue-critical details of structures," *Structure and Infrastructure Engineering*, vol. 14, no. 5, pp. 509–522, 2018.

[19] H. Q. Zheng, Y. R. Yang, X. Y. Sun, and C. Wen, "Nondestructive detection of anchorage quality of rock bolt based on DS-DBN-SVM," in *International Conference on Machine Learning and Cybernetics (ICMLC)*, pp. 288–293, Chengdu, China, 2018.

[20] Z. M. Li, C. X. Liang, and M. S. Wang, "Short-term power generation output prediction based on a PSO-DBN neural network," *Power System Protection and Control*, vol. 48, no. 8, pp. 149–154, 2020.

[21] S. Goudarzi, M. N. Kama, M. H. Anisi, S. A. Soleymani, and F. Doctor, "Self-organizing traffic flow prediction with an optimized deep belief network for internet of vehicles," *Sensors*, vol. 18, no. 10, article 3459, 2018.

[22] X. X. Zhang, Y. Miao, X. Z. Liu, and K. Wu, "Hot strip thickness prediction based on least squares support vector machine with feature extraction by deep belief network," *Metallurgical Industry Automation*, vol. 44, no. 2, pp. 17–22, 2020.

[23] Y. Xie, J. Zou, Z. Li, F. Gao, and C. Peng, "A novel deep belief network and extreme learning machine based performance degradation prediction method for proton exchange membrane fuel cell," *IEEE Access*, vol. 8, pp. 176661–176675, 2020.

[24] J. Melchior, N. Wang, and L. Wiskott, "Gaussian-binary restricted Boltzmann machines for modeling natural image statistics," *Plos One*, vol. 12, no. 2, article e0171015, 2017.

[25] R. R. Dema, R. N. Amirov, and O. R. Latypov, "Mathematical model for assessing the management of quality parameters of hot- rolled strips according to the criterion of local thickness variation," *Materials Today: Proceedings*, vol. 19, no. 5, pp. 2417–2421, 2019.

Hindawi
Journal of Sensors
Volume 2020, Article ID 6687295, 12 pages
https://doi.org/10.1155/2020/6687295

*Research Article*

# Vibration Diagnosis and Treatment for a Scrubber System Connected to a Reciprocating Compressor

**Shuangshuang Li**,[1] **Guicheng Yu**,[2] **Ding Tang**,[2] **Ming Li**,[2] **and Huaming Han**[3]

[1]*School of Mechanical Engineering, Xihua University, Chengdu 610039, China*
[2]*Gas Storage Management Department of PetroChina Southwest Oil and Gasfield Company, Chongqing 401147, China*
[3]*Chongqing Gas District of PetroChina Southwest Oil and Gasfield Company, Chongqing 400021, China*

Correspondence should be addressed to Shuangshuang Li; 15882068051@163.com

Received 19 October 2020; Revised 2 November 2020; Accepted 4 November 2020; Published 24 November 2020

Academic Editor: Aijun Yin



Severe vibration was observed at a scrubber system connected to a reciprocating compressor during commissioning stage. Field measurements including vibration, pressure pulsation, and modal experiment were conducted to determine the causes of vibration, which showed that the excessive vibration was caused by pressure pulsation-induced mechanical resonance. Vibration reduction treatment for mechanical resonance avoidance via the installation of support on scrubber was proposed and then validated by resonance analysis and one-way fluid structure interaction (FSI) analysis. Resonance analysis showed both the dominant frequencies of pressure pulsation and rotational frequencies of compressor were beyond resonance regions, and FSI analysis indicated that the vibration levels of the scrubber system at its design conditions were within the allowable limit. Installation of two braces with a band clamp on the scrubber was implemented. The effectiveness of the treatment was verified by comparison of measured data before and after scrubber modification; the peak amplitudes occurring at the dominant excitation frequencies in both vibration and pulsation spectra declined greatly after modification, which guaranteed the long-term stable operation of the scrubber.

## 1. Introduction

Reciprocating compressors are widely used to boost natural gas pressure to be required because of their flexibility in capacity and pressure range in natural gas storage industry. Since the high-pressure gas discharged from the compression cylinder of a compressor always contains lube oils, a scrubber must be applied on the outlet of the compressor for removal of the lube oils to ensure gas quality before entering the underground storage facilities. Gas pressure pulsations produced by the reciprocating action of the piston could inevitably be transmitted into the pipelines and equipment attached to a reciprocating compressor; no problem occurs unless they coincide with a particular mechanical or acoustic frequency of the system. The pressure pulsations can then be greatly amplified and excite the pipelines and/or equipment, which may result in high vibration. Excessive vibration can lead to many practical problems, such as pipeline fatigue failure, equipment damage, instrument distortion, power consumption, and energy loss. Pipelines and equipment carrying high-pressure and high-speed gas need a high level of reliability and stability.

The vibration of pipelines and equipment connected to the reciprocating compressor is a typical flow-induced vibration. Relevant studies show that vibration is generally induced by poor dynamic balance of structure, poor kinematical design, mechanical resonance, and large pressure pulsations. Researches concerning such vibration have been focusing on three different areas: vibration theory and analysis, vibration diagnosis and identification techniques, and vibration control methods. Vibration theory and analysis mainly include establishment of a vibration model, analytical and numerical solutions of the vibration model [1, 2], modal analysis for avoidance of resonance, vibration analysis and related experimental research [3], fluid-structure interaction (FSI) vibration study [4, 5], vibration dynamic response of

system, acoustic and pulsation analysis using acoustic wave theory, transfer matrix method, and finite element methods [6, 7]. Numerous vibration analysis techniques are employed to predict the vibration level of system during the design phase and to identify the source of high vibration in the operation phase, which mainly focus on field measurement methods, test instrumentation, signal processing, and frequency spectrum analysis [8, 9]. Vibration control methods are aimed at proposing a proper design and/or modification to reduce the mechanical vibration and pressure pulsation to a minimum. Vibration can be controlled by increasing pipe size, increasing buffer tank, shorting pipeline length, adding support, installing orifice, and so on [10–13]. Recent vibration reduction studies mainly focus on natural frequency adjustment and pressure pulsation control [14–16].

These studies lay the foundation for diagnosis, identification, analysis, and mitigation of flow-induced vibration in a reciprocating compressor systems. This paper is devoted to determine the main causes of high vibration encountered by a scrubber system through field vibration measurement, pulsation measurement, and modal experiment and put forward effective vibration reduction treatment via resonance analysis and one-way FSI vibration analysis.

## 2. Vibration Diagnosis and Cause Analysis

One underground natural gas storage station has employed eight reciprocating compressors with a rated power of 4000 kW and a design processing capacity of $166 \times 10^4$ $Nm^3/d$ each to boost natural gas pressure. Each reciprocating compressor is equipped with a scrubber in size $\Phi 610mm \times 2921$ mm to remove lube oil to 0.1 $\mu$m from natural gas to ensure its quality and protect gas storage facilities. During the commissioning of the reciprocating compressor, one scrubber system (see Figure 1) encountered excessive vibration as high as 40 mm/s RMS, which was considered to be dangerous and should be controlled to values less than 18 mm/s to ensure the safety and reliability of the scrubber system [17]. Field measurements are conducted to investigate the factors resulting in such problem, as presented in Figure 2. Measuring parameters include vibration, pressure pulsation, and modal. The measurement sensors employed for field measurements comprise an accelerometer for vibration test, a pressure transmitter for pressure test, and an impact hammer for modal test, in which main specifications are given in Table 1.

*2.1. Vibration Measurements and Analysis.* Vibration measurements were performed to investigate the causes of vibration. The operating parameters of the reciprocating compressor are listed in Table 2. Three vibration measuring points V1, V2, and V3 are located at the scrubber inlet pipeline, the top of the scrubber, and the scrubber outlet pipeline, respectively; each measuring point contains H (horizontal), V (vertical), and A (axial) directions, as shown in Figure 1. Vibration measurement results including vibration displacement, velocity, and acceleration measured by an accelerometer are listed in Table 3. Generally, the velocity method is used to determine the vibration level for low-frequency

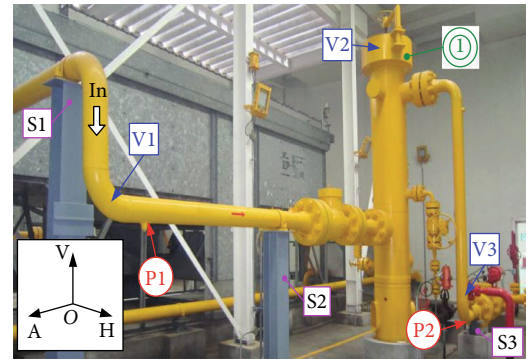


Figure 1: Scrubber system connected to a reciprocating compressor.

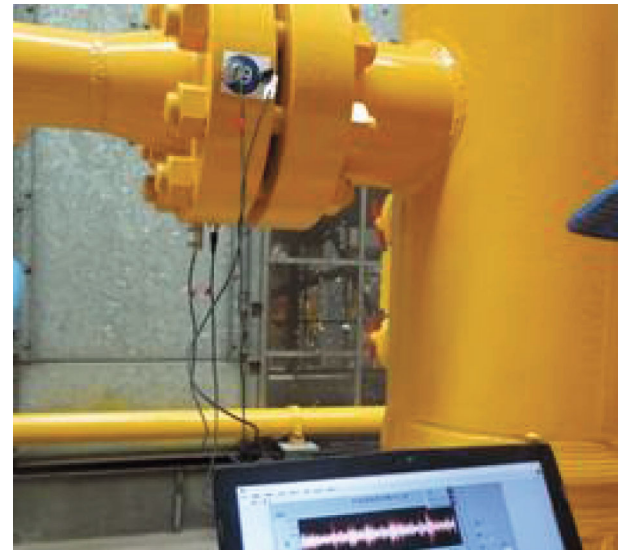

Figure 2: Field measurements for the scrubber system.

steady-state vibration. Table 3 reveals that the maximum velocity is observed at the top of the scrubber, especially in the A direction, and the velocity values measured at measuring point V2 in the H and A directions are greater than the allowable velocity limits (18 mm/s), which indicates that the scrubber stiffness in the *A* direction is weaker than that in the H and V directions.

Vibration spectrum analysis was applied to identify the frequency contents of the vibration signals [18]. The vibration frequency spectra measured at points V1, V2, and V3 in the A direction are displayed in Figure 3. The problematic frequency components can be seen straight. The spectrum measured at point V1 in the A direction exhibits mainly two dominant frequency components of 16.56 Hz and 32.39 Hz, which are related to the reciprocating compressor rotational frequency and its second harmonics calculated by Equation (1). This revealed that the main source of vibration excitation at the scrubber inlet pipeline was the pressure pulsation caused by the intermittent suction/discharge flow of the reciprocating compressor. The spectrum measured at V2 in the A direction shows mainly two dominant frequency components of 5.9 Hz and 16.56 Hz; the vibration peak at

Table 1: Measurement sensors and the main specifications.

| Sensor | Measuring parameter | Type | Technical specifications |
|---|---|---|---|
| Accelerometer | Vibration | PCB 608A11 | Range: 0.5 Hz to 10 kHz<br>Sensitivity(±15%): 100 mV/g<br>Measurement range: ±50 g<br>Broadband resolution: 350 $\mu$g |
| Pressure transmitter | Pressure | Wotian PCM 301 | Range: 0~30 MPa<br>Accuracy: ±0.5%<br>Response time: ≤1 ms<br>Shock: 100 g |
| Impact hammer | Modal | PCB 086D20 | Range: ±22,240 N pk<br>Sensitivity (±15%): 0.23 mV/N<br>Resonant frequency: 12 kHz<br>Nonlinearity: 1% |

Table 2: The main operating parameters of the reciprocating compressor.

| Rotational speed (rpm) | Processing capacity ($Nm^3/d$) | Inlet pressure (MPa) | Outlet pressure (MPa) | |
|---|---|---|---|---|
| | | | First stage | Second stage |
| 994 | $149.2 \times 10^4$ | 7.61 | 13.62 | 24.41 |

Table 3: Vibration measurement results at the three points V1, V2, and V3.

| Point | Direction | Displacement ($\mu$m RMS) | Velocity (mm/s RMS) | Acceleration ($m/s^2$ RMS) |
|---|---|---|---|---|
| V1 | H | 196.1 | 15.33 | 1.85 |
| | V | 125.65 | 11.55 | 1.63 |
| | A | 105.49 | 10.78 | 1.31 |
| V2 | H | 215.8 | 18.6 | 1.91 |
| | V | 83.29 | 9.45 | 1.39 |
| | A | 271.7 | 25.76 | 2.04 |
| V3 | H | 49.03 | 4.41 | 0.89 |
| | V | 57.97 | 5.83 | 0.94 |
| | A | 71.32 | 8.56 | 1.12 |

5.9 Hz contributes to about 70% of the total vibration. Similarly, the two dominant frequencies of 5.9 Hz and 16.56 Hz are observed at the point V3 in the A direction. It is known that the pipelines and equipment connected to the reciprocating compressor vibrate inevitably at the rotational frequency and harmonics of the compressor. Hence, the problematic frequency of 5.9 Hz observed at the top of the scrubber was usually related to the scrubber structure and/or flow-induced vibration (FIV).

$$f_{ex} = \frac{N}{60} ki, \tag{1}$$

where $f_{ex}$ is the compressor rotational frequency (Hz); $N$ is the compressor rotational speed (rpm), for single-action piston $k = 1$ or double-action piston $k = 2$; and $i$ is the harmonic order of frequency.

### 2.2. Acoustic and Pulsation Analysis

*2.2.1. Acoustic Analysis.* The pressure pulsations of fluid are referred to as acoustical, because they travel through a system at the speed of sound of the gas. Pressure pulsations are generally too weak to cause any problem; however, they can be strongly amplified and result in high vibration due to acoustic resonance when a particular excitation frequency matches the acoustic frequency. Acoustic analysis was carried out to find out the acoustic frequencies of system using the transfer matrix method. In this method, the structural system is divided into several elements such as a pipe, a volume, and a resistance [19]. Each element has a transfer matrix [M]. Ignoring damping effects, the $2 \times 2$ transfer matrix is then formulated by multiplying all the transfer matrices to relate the pressure pulsation $p$ and the flow pulsation $u$ between the inlet and outlet of system, which can be written as [20]

$$\begin{bmatrix} p_{out} \\ u_{out} \end{bmatrix} = [M_n][M_{n-1}] \cdots [M_2][M_1] \begin{bmatrix} p_{in} \\ u_{in} \end{bmatrix}. \tag{2}$$

The subscripts "in" and "out" represent the conditions at the inlet and outlet of the system, respectively. As presented in Figure 1, the scrubber system is mainly composed of three elements: the inlet pipeline, scrubber itself, and outlet pipeline. Therefore, the mathematical model for the scrubber system can be considered to a "P-V-P" (pipe-volume-pipe) acoustic system, as shown in Figure 4. The transfer matrices of the inlet pipeline, scrubber itself, and outlet pipeline are given by Equations (3), (4), and (5), respectively. So the matrix equation of an acoustic model for the scrubber system can be expressed by Equations (6).

$$[M_1] = \begin{bmatrix} \cos \frac{\omega}{a} L_1 & -\rho_0 a \sin \frac{\omega}{a} L_1 \\ \frac{1}{\rho_0 a} \sin \frac{\omega}{a} L_1 & \cos \frac{\omega}{a} L_1 \end{bmatrix}, \tag{3}$$

$$[M_2] = \begin{bmatrix} 1 & 0 \\ \frac{V\omega}{S_2 \rho_0 a^2} & \frac{S_1}{S_2} \end{bmatrix}, \tag{4}$$

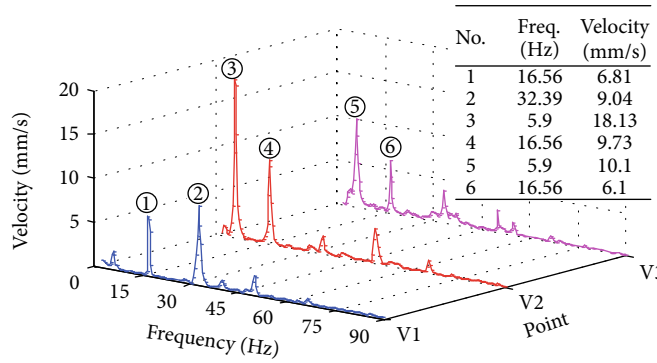


| No. | Freq. (Hz) | Velocity (mm/s) |
|---|---|---|
| 1 | 16.56 | 6.81 |
| 2 | 32.39 | 9.04 |
| 3 | 5.9 | 18.13 |
| 4 | 16.56 | 9.73 |
| 5 | 5.9 | 10.1 |
| 6 | 16.56 | 6.1 |

Figure 3: Vibration spectrum comparison of the three points in the A (axial) direction.

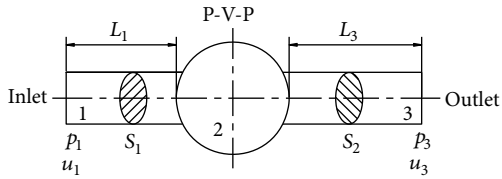


Figure 4: Acoustic mathematical model of the scrubber system.

$$[M_3] = \begin{bmatrix} \cos\frac{\omega}{a}L_2 & -\rho_0 a \sin\frac{\omega}{a}L_2 \\ \frac{1}{\rho_0 a}\sin\frac{\omega}{a}L_2 & \cos\frac{\omega}{a}L_2 \end{bmatrix}, \quad (5)$$

$$\begin{bmatrix} p_3 \\ u_3 \end{bmatrix} = [M_3][M_2][M_1]\begin{bmatrix} p_1 \\ u_1 \end{bmatrix}, \quad (6)$$

where $\omega$ is the angular velocity (rad/s), $L$ is the effective length of the pipeline (m), $a$ is the sound speed of gas (m/s), $\rho$ is the density of gas (kg/m$^3$), $S$ is the cross-sectional area inside the pipeline (m$^2$), $V$ is the volume of volume element (m$^3$), and the subscripts 1, 2, and 3 represent the number of each element.

The acoustic frequencies can be determined by solving Equation (6) in consideration of boundary conditions. The pipeline connected to a large volume can be regarded as an open end, if not, a closed end. For an open end, the boundary conditions are that the pressure pulsation $p$ is zero but flow pulsation $u$ is not zero; for a closed end, the flow pulsation $u$ is zero but pressure pulsation $p$ is not zero. The pulsation can be set to 1 when it is not zero, which will not affect the results of acoustic frequencies. So the boundary conditions of the scrubber system are

$$\begin{cases} p_3 = 1, & u_3 = 0, \\ p_1 = 1, & u_1 = 0. \end{cases} \quad (7)$$

Using these boundary conditions in Equation (7), Equation (6) can be derived as

Table 4: The key structure parameters of the scrubber system.

| Parameter | L1 (m) | L2 (m) | S1 (m$^2$) | S2 (m$^2$) | $V$ (m$^3$) |
|---|---|---|---|---|---|
| Value | 11 | 9 | 0.528 | 0.528 | 0.0154 |

Table 5: Physical properties of the natural gas in the scrubber system.

| Property | Symbol | Value |
|---|---|---|
| Ratio of specific heats | $k_v$ | 1.29 |
| Relative density | $r_\rho$ | 0.588 |
| Gas constant (J/(kg·K)) | $R_g$ | 488.06 |
| Absolute pressure (MPa) | $p$ | 24.41 |
| Absolute temperature (K) | $T$ | 311.15 |
| Compressibility factor | $Z$ | 0.838 |
| Sound speed (m/s) | $a$ | 431.4 |

Table 6: The first four acoustic frequencies of the scrubber system.

| Acoustic frequency | First | Second | Third | Fourth |
|---|---|---|---|---|
| $f_{ac}$ (Hz) | 10.42 | 13.41 | 29.81 | 36.32 |

$$\sin\frac{\omega}{a}L_2\cos\frac{\omega}{a}L_1 + \frac{V\omega}{S_2 a}\cos\frac{\omega}{a}L_2\cos\frac{\omega}{a}L_1 + \cos\frac{\omega}{a}L_2\sin\frac{\omega}{a}L_1 = 0, \quad (8)$$

$$f_{ac} = \frac{\omega}{2\pi}. \quad (9)$$

The acoustic frequencies $f_{ac}$ of the scrubber system not only depend on its structure parameters but also on the fluid parameters inside the scrubber, such as density and sound speed of fluid. The key structure parameters of the scrubber system and physical properties of the natural gas in the scrubber system are given in Tables 4 and 5, respectively. Using these data, the first four acoustic frequencies of the scrubber system were calculated by solving Equation (8) and Equation (9), in which results are listed in Table 6. As discussed above, the main excitation frequencies of vibration are 5.9 Hz and 16.56 Hz (the rotational frequency) and in its

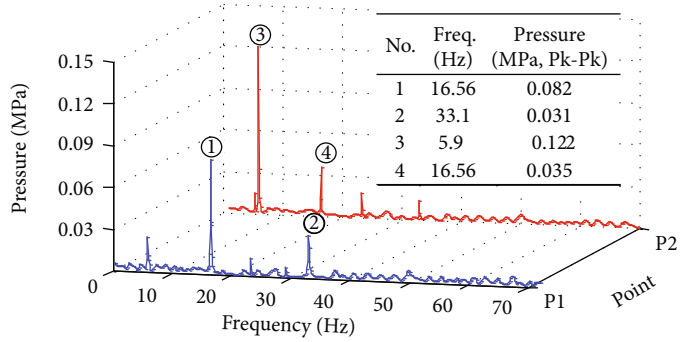


| No. | Freq. (Hz) | Pressure (MPa, Pk-Pk) |
|---|---|---|
| 1 | 16.56 | 0.082 |
| 2 | 33.1 | 0.031 |
| 3 | 5.9 | 0.122 |
| 4 | 16.56 | 0.035 |

Figure 5: Pressure spectrum comparison of points P1 and P2.

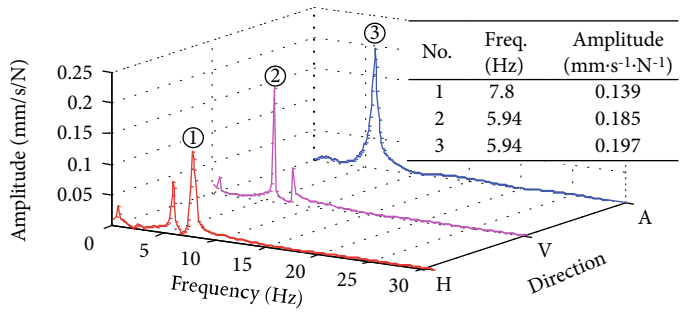


| No. | Freq. (Hz) | Amplitude ($mm \cdot s^{-1} \cdot N^{-1}$) |
|---|---|---|
| 1 | 7.8 | 0.139 |
| 2 | 5.94 | 0.185 |
| 3 | 5.94 | 0.197 |

Figure 6: Impact response spectrum obtained at impact point ① by modal experiment.

harmonics, it is obvious that the acoustic frequencies of the scrubber system are far away from them. It can be concluded that the acoustic frequencies of the scrubber system were not excited by the main excitation frequencies; there was no acoustic resonance in the scrubber system.

*2.2.2. Pulsation Analysis.* Even for steady flow conditions, pressure pulsation is an important source of energy responsible for scrubber vibration. Pressure pulsation has several characteristic frequencies, which normally results in low-amplitude vibration, and no problem occurs unless these pulsations coincide with the mechanical and/or acoustical resonance frequency of a system. Pulsation measurements were performed upstream and downstream of the scrubber using a pressure transmitter to find the dominant excitation frequency components. Two pressure pulsation measuring points P1 and P2 are shown in Figure 1. The frequency components and magnitude of the pressure pulsation were analysed to determine its characteristics and its potential effect, in which results are represented in Figure 5. It can be seen that the resulting pressure pulsation is a low-frequency pulsation; the pulsation at point P1 mainly contains several harmonics of the rotational frequency of 16.56 Hz; however, the pulsation at point P2 is strongest at 5.9 Hz; spikes at the harmonics of 16.56 Hz exist as well. As the dominant frequency of 5.9 Hz was observed downstream of the scrubber but not observed upstream of the scrubber, it can be concluded that the dominant excitation frequency occurred at 5.9 Hz.

*2.3. Modal Analysis.* Modal experiment was conducted at the impact point ① (see Figure 1) to acquire the MNFs (mechanical natural frequencies) of the scrubber system. From

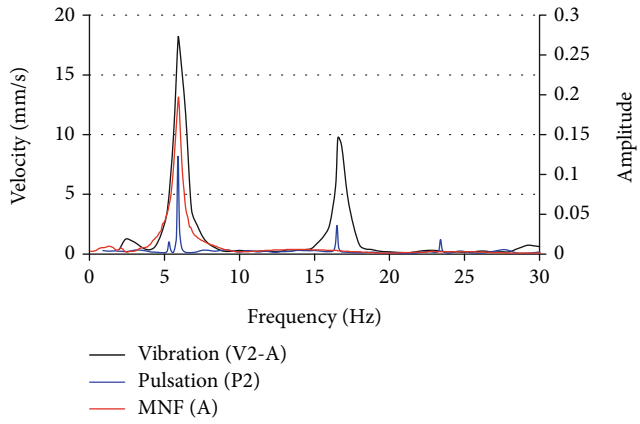


Figure 7: The spectrum overlay of vibration, pulsation, and MNF.

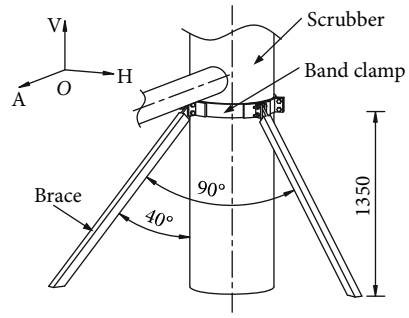


Figure 8: The scrubber supported by two braces with a band clamp.

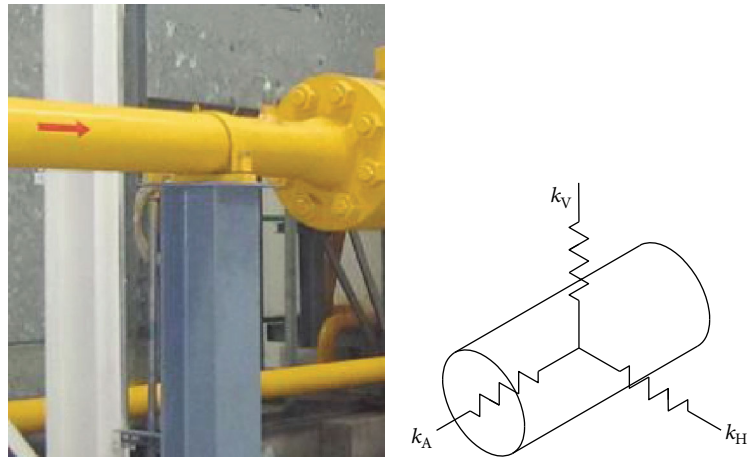


Figure 9: Pipe support: (a) common support; (b) support simplified model.

Table 7: The boundary conditions applied in the simulation model of the original scrubber system.

| Location | Boundary conditions |
|---|---|
| S1 | $k_H = 3.80E+03$ N/mm, $k_V = 7.60E+05$ N/mm, $k_A = 2.67E+04$ N/mm |
| S2 | $k_H = 5.87E+04$ N/mm, $k_V = 9.88E+05$ N/mm, $k_A = 8.34E+03$ N/mm |
| S3 | $k_H = 2.17E+06$ N/mm, $k_V = 3.29E+06$ N/mm, $k_A = 3.09E+05$ N/mm |

Figure 6, two fundamental frequencies of 5.94 Hz and 7.8 Hz are found in the three directions; the peak amplitude in the A direction is greater compared to the other two directions, which indicates that the scrubber is more likely to vibrate in the A direction.

Meanwhile, the relationships among the vibration, pressure pulsation, and MNFs of the scrubber system can be compared to reveal potential causes of vibration. According to the spectrum overlay shown in Figure 7, the dominant frequency of pressure pulsation at 5.9 Hz is very close to the first MNF of the scrubber system of 5.94 Hz; the highest vibration occurs at 5.9 Hz, so it can be concluded that the main cause of the excessive vibration was pressure pulsation-induced mechanical resonance.

## 3. Vibration Reduction Treatment and Analysis

*3.1. Vibration Reduction Treatment.* The motion equation of forced vibration of a structure system is given by Equation (10). In practice, it is useful to add mass, increase damping, add stiffness, and reduce exciting force to minimize the vibration response of a structure system.

$$M\{\ddot{x}(t)\} + C\{\dot{x}(t)\} + K\{x(t)\} = \{F(t)\}, \quad (10)$$

where $M$ is the mass matrix, $C$ is the damping matrix, $K$ is the stiffness matrix, $\{F(t)\}$ is the exciting force vector, and $\{x(t)\}$ is the vibration displacement vector.

The highest vibration level at 5.9 Hz was due to resonance, so it is necessary to separate the MNFs of the scrubber system from the dominant frequency of pulsation as a countermeasure against vibration. Resonance avoidance solutions were needed to eliminate such vibration problem, such as adjusting MNFs by adding support and change in operation conditions to shift pulsation frequency. As the scrubber must have a wide range of operating conditions to meet the requirements of reciprocating compressor, changing the MNFs of the scrubber system was more effective than changing the operation conditions to control vibration. As discussed above, the vibration of the scrubber system is low-frequency vibration; the vibration response of the system can be said to be stiffness dominated. A practical method of changing the MNFs of the scrubber system may be installation of a new support to increase system stiffness. In this study, two braces with a band clamp are installed at the middle of the scrubber to raise its MNFs beyond the resonance region of concern, as displayed in Figure 8.

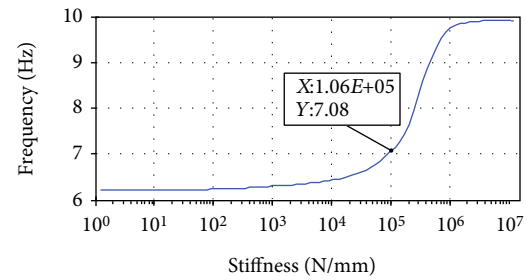


Figure 10: The effect of the axial stiffness of the brace on the first MNF of the modified model.

*3.2. Resonance Analysis.* The effectiveness of the vibration reduction treatment should be analysed before implementation. Finite element method (FEM) is also useful to

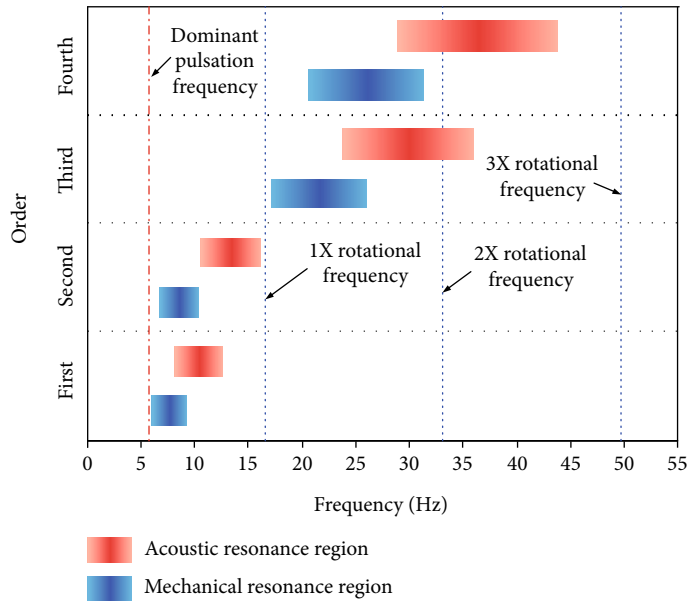


Figure 11: Resonance analysis of the modified model of the scrubber system.

determine modal parameters of a structure system. The simulation model of the original scrubber system modelled from the construction drawings and physical measurement was used to calculate the MNFs and mode shapes, which shall be validated by the results of modal experiment discussed in Section 2.3. Material of the scrubber system was steel with density $\rho = 7850\,\text{kg/m}^3$, Young's modulus $E = 210\,\text{GPa}$, and Poisson's ratio $\nu = 0.3$. The scrubber inlet and outlet pipelines are restrained by several supports, as presented in Figure 1; each support can be simplified as a spring with three stiffness values of $k_H$, $k_V$, and $k_A$, as shown in Figure 9. These stiffness values at locations S1, S2, and S3 (see Figure 1) can be calculated by FEM using the software Ansys, the results of which are listed in Table 7 [21].

Using these boundary conditions in Table 7, the first mechanical natural frequency of the original scrubber system is 6.21 Hz. There is a relatively low (4%) disagreement compared with the result of modal experiment. Such a slight disagreement is acceptable in engineering application, so the simulation model of the original scrubber system was validated and then was used to optimize the design of the two braces. Some factors causing the disagreement could be idealizations and simplifications of the scrubber structure, difficulties in obtaining actual stiffness of support because of insufficient support, uncertainties in surface soil effect on concrete piers, etc.

A modified model of the scrubber system was modelled on the basis of the vibration reduction treatment shown in Figure 8, in which MNFs greatly depend on the stiffness of the two braces. The brace can be defined as a spring with different axial and radial stiffness. Since the two braces and band clamp are connected together by several bolted connections, the axial stiffness of the brace has far greater influence on the MNFs of the modified model than its radial stiffness. From Figure 10, the first MNF of the modified model increases with an increase in the axial stiffness of brace and increases greatly

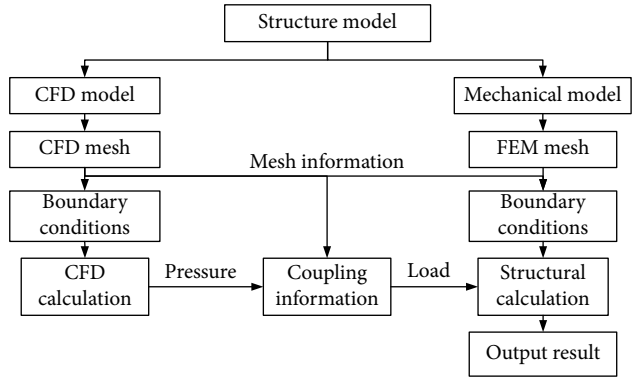


Figure 12: One-way FSI analysis process for flow-induced vibration.

from $1E + 04$ N/mm to $1E + 06$ N/mm. To control the vibration problem, the predicted MNFs of the modified model should be designed to be separated from the dominant excitation frequencies of 5.9 Hz by at least 20%, which means the axial stiffness of the brace should be at least $1.06E + 05$ N/mm to ensure the modified model has a mechanical natural frequency higher than 7.08 Hz.

In order to avoid mechanical resonance and acoustic resonance, the MNFs and acoustic frequencies of the modified scrubber system should have a separation margin of 20% from the significant excitation frequencies, such as dominant pulsation frequency and the 1X (first) rotational frequency of the reciprocating compressor. In this study, the first four MNFs of the modified model were obtained by the finite element method with the assumption that the axial stiffness of the brace was $2E + 05$ N/mm. Resonance analysis was performed to show the relationships among the MNFs, acoustic frequencies, dominant pulsation frequency, and rotational frequencies of the modified model. As show in Figure 11, the blue boxes present the first four mechanical resonance

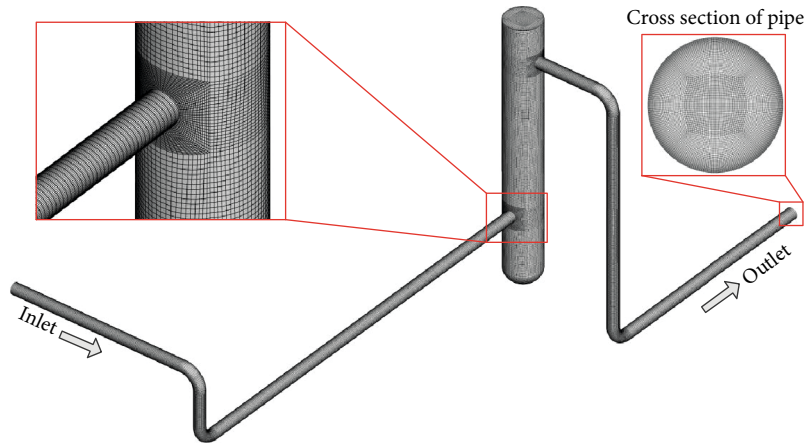


Figure 13: Numerical mesh of the CFD model in the modified scrubber system.

regions, and the red boxes the first four acoustic resonance regions; the dominant pulsation frequency, 1X rotational frequency, and 3X rotational frequency are beyond the resonance region; the 2X rotational frequency is within the third- and fourth-order acoustic resonance regions, but not in the core region. As the first-order acoustic frequency excited by the dominant excitation frequency is often more destructive than others in engineering application, it can be seen that both mechanical resonance and acoustic resonance are avoided by this vibration reduction treatment.

*3.3. Fluid-Structure Interaction Vibration Analysis.* The vibration of the scrubber system is a complex fluid-structure interaction (FSI) problem, the fluid flow exerts pressure loads on the structure, and these pressure loads induce structural deformation and vibration to change the fluid flow itself. Such problems generally need numerical simulations, as it is difficult to obtain analytical solutions. From Table 3, the maximum vibration displacement of the scrubber system is 215.8 micron; it can be seen that such displacement is not large enough to have a significant impact on the fluid flow, so one-way coupling FSI analysis can be applicable for vibration simulation of the scrubber system. The one-way FSI analysis process is illustrated in Figure 12, which shows that the pressure calculated by CFD (Computational Fluid Dynamics) calculation at the fluid-structure interface is transferred to the mechanical model and applied as load in structural calculation.

To evaluate the vibration level of the modified scrubber system at its design condition, one-way FSI analysis was performed. The CFD model of the modified scrubber system was built up for CFD calculation. The numerical mesh of the CFD model is constructed with a combination of unstructured and structural mesh elements, as plotted in Figure 13. Since the results of CFD calculation are very sensitive to the mesh quality, this numerical mesh independence was tested, which showed that a deviation of less than 0.1% was obtained in relation to pressure drop.

The design condition of the scrubber is the processing capacity which is $166 \times 10^4\ \mathrm{Nm^3/d}$, the outlet pressure 30 MPa, and the rotational frequency 16.667 Hz (1000 rpm). According to the API 618 standards, the maximum allowable pressure pulsation is 0.5%, and the static pressure of gas is 30 MPa, so the dynamic pressure calculated is 0.15 MPa [22]. Hence, the pressure at the end of the scrubber outlet pipeline can be described as $p = 30 + 0.075\sin(104.667t)$ (MPa); the boundary conditions for CFD calculation are listed in Table 8. In this paper, transient-state CFD calculation was carried out using the software FLUENT, the realizable $k - \varepsilon$ model was employed, time step was 0.0001 s, and total time is 0.06 s. The pressure distribution of the fluid-structure interface in the CFD model at 0.04 s is presented in Figure 14.

Table 8: Boundary conditions of the CFD model in the scrubber system for CFD calculation.

| Position | Boundary condition | Value |
|---|---|---|
| Inlet | Velocity inlet | 4.215 (m/s) |
| Outlet | Pressure outlet | $30 + 0.075\sin(104.667t)$ (MPa) |
| Wall | Wall | No slip wall |

According to the one-way FSI analysis process in Figure 12, these pressure loads were transferred to the mechanical model of the modified scrubber system, and then, the vibration response was simulated in structural calculation using the software Ansys. Figure 15 shows the vibration velocity of the modified scrubber system; the maximum velocity of 9.63 mm/s observed at the top of the scrubber is below 18 mm/s, which illustrates that the vibration level is reduced to the allowable limit when operating at its design condition.

## 4. Implementation and Evaluation of Countermeasures

Both the resonance analysis and fluid-structure interaction vibration analysis indicate that the vibration reduction treatment proposed is effective to mitigate the vibration problem. Installation of two braces with a band clamp is implemented on the scrubber on the basis of the above analysis, as displayed in Figure 16. After modification of the scrubber system, vibration and pressure measurements were carried out at the same points as before. The operating parameters of

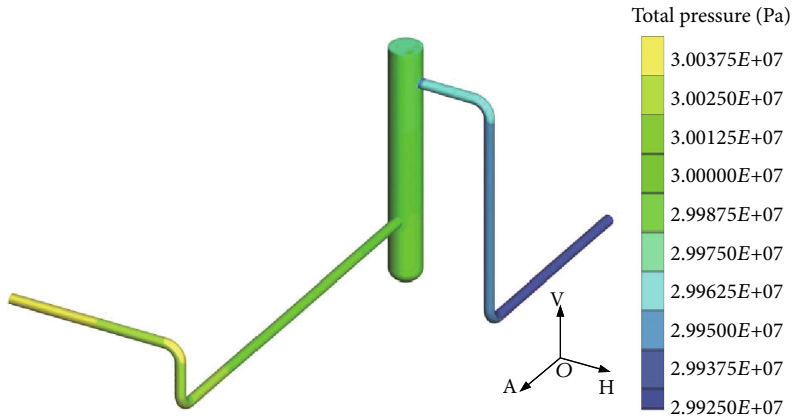


Figure 14: Pressure distribution of the fluid-structure interface in the CFD model at 0.04 s.

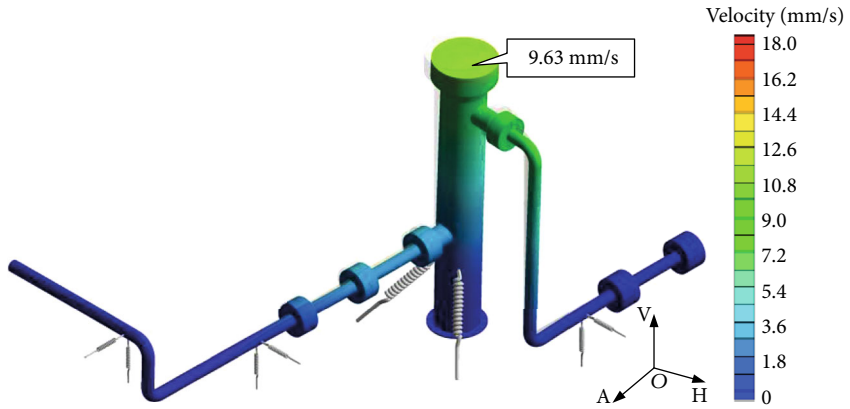


Figure 15: Vibration velocity of the modified scrubber system at its design condition.

the reciprocating compressor during measurements after modification are listed in Table 9, which are very similar to that (see Table 2) before. The comparison of vibration velocity measured at points V1, V2, and V3 before and after modification is plotted in Figure 17; it can be seen that all the vibration velocity values are reduced to a considerable extent; especially, the maximum vibration velocity at point V2 in the A direction is decreased by 67.31% from 25.76 mm/s to 8.42 mm/s. The velocity spectrum of point V2 after modification, as shown in Figure 18, outlines that the dominant frequency of vibration is the compressor rotational frequency of 16.56 Hz, but the vibration amplitudes occurring at 5.92 Hz are small. By comparing the pressure spectrum of point P2 before and after modification presented in Figure 19, the dominant frequency is 16.56 Hz, and pressure pulsation occurring at 5.9 Hz declines by 84.4% from 0.122 MPa, peak to peak, to 0.019 MPa, peak to peak.

## 5. Results and Discussion

The potential causes of vibration can be revealed by vibration and pulsation measurements, acoustic analysis, and modal analysis. Vibration measurement and analysis are beneficial for diagnosis and characterization of vibration. Pulsation measurement is a good way of understanding the characteristics of pressure pulsation for pulsation reduction to control

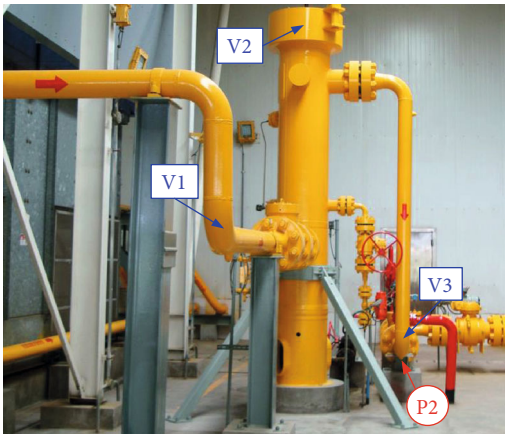


Figure 16: The modified scrubber system supported by two braces.

Table 9: The operating parameters of the reciprocating compressor after scrubber modification.

| Rotational speed (rpm) | Processing capacity ($Nm^3/d$) | Inlet pressure (MPa) | Outlet pressure (MPa) | |
|---|---|---|---|---|
| | | | First stage | Second stage |
| 994 | 145.8 × 104 | 7.56 | 13.32 | 24.26 |

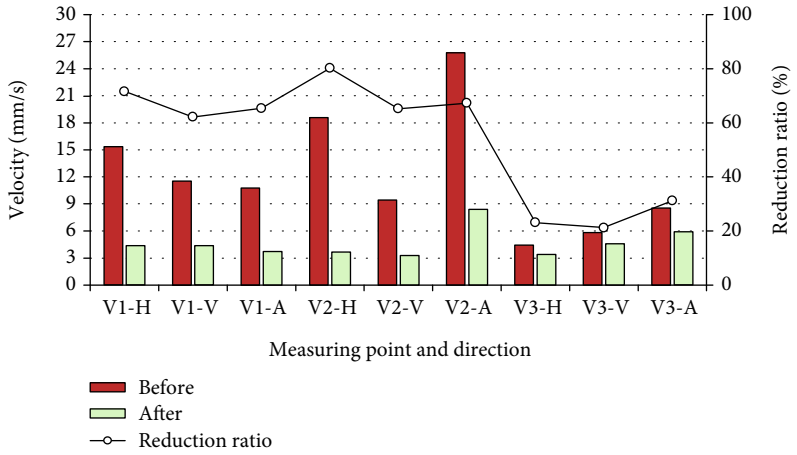


Figure 17: Comparison of vibration velocity measured before and after modification.

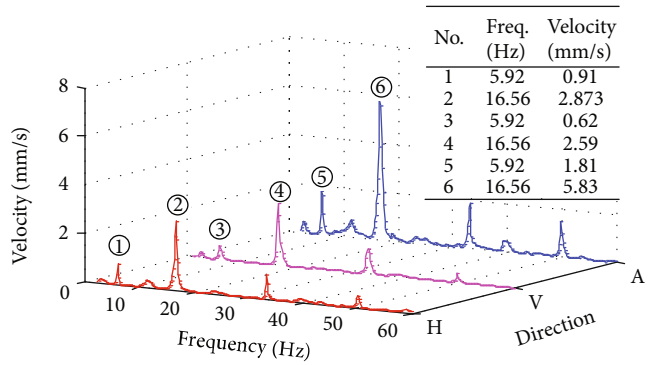


Figure 18: Velocity spectrum of point V2 after modification.

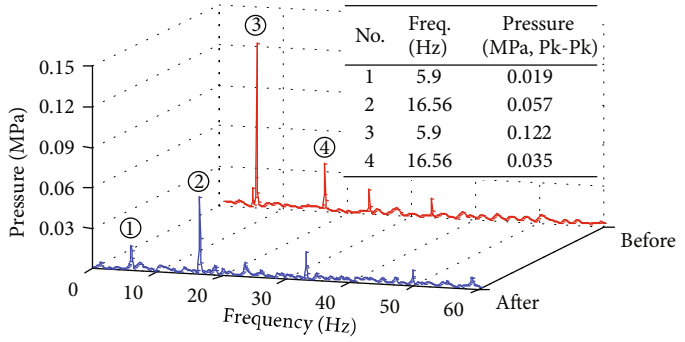


Figure 19: Pressure spectrum comparison of point P2 before and after modification.

flow-induced vibration. Acoustic analysis is used to determine the acoustic frequencies of system to avoid acoustic resonance. Modal analysis using experiment and/or the finite element method is used to obtain the modal parameters to avoid mechanical resonance. In this paper, the highest vibration of the scrubber system was observed near the mechanical resonance frequency of 5.94 Hz, followed by 16.56 Hz; the excitation source resulting from pressure pulsation in the scrubber had several clear spikes in the range of 0-70 Hz, which clearly contained 5.9 Hz and 16.56 Hz, so the excessive vibration problem resulted from pressure pulsation-induced mechanical resonance.

Effective vibration mitigation measures are needed to be developed based on field measurement data and structural dynamics models for optimizing feasible solutions. Flow-induced vibration can be mainly controlled by avoiding mechanical resonance, acoustic resonance, and high pressure pulsation in a structure system. Resonance analysis is essential for avoidance of mechanical resonance and acoustic resonance in system. FSI analysis using the finite element method can determine the vibration level of the structure system. However, the accuracy of results depends greatly on the idealizations and simplifications of system, the numerical mesh quality, boundary conditions, etc. In this study, a

vibration reduction treatment was proposed by installation of two braces with a band clamp at the middle of the scrubber to increase its MNFs; the simulation model of the original scrubber system was developed and validated by comparison with the modal experiment, resonance analysis revealed mechanical resonance, and acoustic resonance can be avoided when the brace had an axial stiffness greater than 2 $E + 05$ N/mm, and the FSI vibration analysis revealed that the vibration level of the modified scrubber system at its design conditions was within the acceptable limit.

Two braces with band clamp were installed on the scrubber as countermeasure against vibration. The effectiveness of the vibration reduction treatment was confirmed by comparison with the field measured data before and after modifications. The MNFs of the modified scrubber increased and was away from the dominant excitation frequencies of pressure pulsation, so mechanical resonance was avoided. The vibration and pulsation values were reduced greatly after modification. To conclude, with this modification in the scrubber system, the vibration problem was eliminated altogether and the scrubber can operate safely at its design conditions.

## 6. Conclusions

Flow-induced vibration in a reciprocating compressor system can only be minimized with proper design and configuration of structure. There are two elastic vibration systems: mechanical structure system and acoustic system; each system has natural or resonant frequencies. Severe vibration can be induced by mechanical and/or acoustic resonance due to coincidence with a particular mechanical natural frequency and/or acoustic frequency. Field measurements including vibration, pressure pulsation, and modal experiment in combination with frequency spectrum analysis are useful to diagnose vibration problem. Development of a practical and effective vibration control measure should need field measured data, resonance analysis, and FSI vibration analysis using the finite element method.

## Data Availability

The data used to support the findings of this study are available from the corresponding author upon request.

## Conflicts of Interest

The authors declare that there is no conflict of interest regarding the publication of this paper.

## Acknowledgments

This research was funded by the Open Research Subject of Key Laboratory (Research Base) of Fluid and Power Machinery of Xihua University, Ministry of Education (szjj2017-081); the Key scientific research fund of Xihua University (Z17118); the Natural Science Foundation of the Education Department of Sichuan Province (18ZB0574).

## References

[1] S.-H. Lee, S.-M. Ryu, and W.-B. Jeong, "Vibration analysis of compressor piping system with fluid pulsation," *Journal of Mechanical Science and Technology*, vol. 26, no. 12, pp. 3903–3909, 2012.

[2] Y. Li, K. Quan, R. Wu, Y. Chang, B. Guo, and B. Zhang, "Numerical simulation and experimental validation of large pressure pulsation in reciprocating compressor," *Energy Procedia*, vol. 160, pp. 606–613, 2019.

[3] H. Lu, X. Wu, and K. Huang, "Study on the effect of reciprocating pump pipeline system vibration on oil transportation stations," *Energies*, vol. 11, no. 1, p. 132, 2018.

[4] S. Li, B. W. Karney, and G. Liu, "FSI research in pipeline systems – a review of the literature," *Journal of Fluids and Structures*, vol. 57, pp. 277–297, 2015.

[5] M. Siba, W. Wanmahmood, M. Z. Nuawi, and R. Rasani, "Flow-induced vibration in pipes: challenges and solutions—a review," *Journal of Engineering Science and Technology*, vol. 11, no. 3, pp. 362–382, 2016.

[6] Y. Zhao, B. Zhao, Q. Zhou, X. Jia, J. Feng, and X. Peng, "Analysis and control of severe vibration of a screw compressor outlet piping system," in *International Compressor Engineering Conference*, Purdue University, 610 Purdue Mall, West Lafayette, Indiana, United States, 2016.

[7] T. C. Allison and J. Bennett, "Acoustically induced vibration mitigations in compressor piping systems," in *Turbo Expo: Power for Land, Sea, and Air*, no. article V009T024A023, 2016American Society of Mechanical Engineers, 2016.

[8] J. Wu and S. Y. Zheng, "Field measurement and numerical study of the vibration in the pipeline of centrifugal compressor," *Journal of Pressure Vessel Technology*, vol. 141, no. 5, 2019.

[9] P. Cyklis, "Advanced techniques for pressure pulsations modeling in volumetric compressor manifolds," *Journal of vibration and acoustics*, vol. 132, no. 6, 2010.

[10] J. Wang, C. Deng, S. Zhang, X. Guo, and G. Yang, "Research on vibration control in a reciprocating compressor piping system using an orifice tube structure," in *2019 2nd International Conference on Safety Produce Informatization (IICSPI)*, pp. 133–136, Chongqing, China, 2019, IEEE.

[11] P. Dubey, G. Reddy, and K. Vaze, "Vibration mitigation of H2s booster discharge pipeline of a typical heavy water plant," *Procedia Engineering*, vol. 86, pp. 818–826, 2014.

[12] T. Han, C. Huang, and A. C. Tan, "Experimental and finite element analysis to identify the source of vibration of a coach," *Engineering Failure Analysis*, vol. 44, pp. 100–109, 2014.

[13] F. Trebuňa, F. Šimčák, R. Huňady, and M. Pástor, "Identification of pipes damages on gas compressor stations by modal analysis methods," *Engineering Failure Analysis*, vol. 27, pp. 213–224, 2013.

[14] Q. Ma, Z. Wu, G. Yang, Y. Ming, and Z. Xu, "Pulsation suppression in a reciprocating compressor piping system using a two-tank element," *Proceedings of the Institution of Mechanical Engineers, Part E: Journal of Process Mechanical Engineering*, vol. 232, no. 4, pp. 427–437, 2017.

[15] M. H. Ghazali, L. M. Hee, and M. S. Leong, "Piping vibration due to pressure pulsations," in *Advanced Materials Research*, pp. 350–354, Trans Tech Publ, 2014.

[16] Y.-W. Kim and Y.-S. Lee, "Damage prevention design of the branch pipe under pressure pulsation transmitted from main

steam header," *Journal of Mechanical Science and Technology*, vol. 22, no. 4, pp. 647–652, 2008.

[17] ISO, *Mechanical vibration — measurement and evaluation of machine vibration — part 1: general guidelines*, ISO, 2016.

[18] S. Li, L. Zhang, and C. Kong, "Vibration failure analysis and countermeasures of the inlet pipelines at a gas Compressor Station," *Shock and Vibration*, vol. 2019, 8 pages, 2019.

[19] Z. Liang, S. Li, J. Tian, L. Zhang, C. Feng, and L. Zhang, "Vibration cause analysis and elimination of reciprocating compressor inlet pipelines," *Engineering Failure Analysis*, vol. 48, pp. 272–282, 2015.

[20] T. Nakamura, S. Kaneko, F. Inada et al., *Flow-Induced Vibrations: Classifications and Lessons from Practical Experiences*, Butterworth-Heinemann, 2013.

[21] P. A. A. M. Junior and T. M. Portela, "Evaluation of the stiffness effect of pipe supports in relation to static and dynamic loads in a flexibility analysis," *International Journal of Advanced Engineering Research and Science*, vol. 5, no. 6, pp. 91–94, 2018.

[22] P. Shejal and A. Desai, "Pulsation and vibration study of reciprocating compressor according to API 618," *International Journal of Modern Engineering Research*, vol. 4, no. 7, 2014.